Ray Tracing Analysis for the mid-latitude SuperDARN HF radar at Blackstone incorporating the IRI-2007 model

Nitya Ravindran Varrier

Thesis submitted to the faculty of the Virginia Polytechnic Institute and State University in partial fulfillment of the requirements for the degree of

Master of Science
In
Electrical Engineering

Dr. J. Micheal Ruohoniemi, Co-Chair

Dr. Joseph B.H. Baker, Co-Chair

Dr. Steven W. Ellingson

Dr. Wayne A. Scales

June 29, 2010
Blacksburg, Virginia

Keywords: SuperDARN, HF radar, Propagation Analysis, Ray Tracing, IRI-2007

Ray Tracing Analysis for the mid-latitude SuperDARN HF radar at Blackstone incorporating the IRI-2007 model

Nitya Ravindran Varrier

ABSTRACT

The Super Dual Auroral Radar Network (SuperDARN) is an international network of high frequency (HF) coherent scatter radars, employed to detect backscatter from magnetic field aligned plasma irregularities in the ionosphere and to study the near- Earth space weather. Space weather impacts many technological systems including HF communications, Global Positioning System (GPS), and surveillance radars. Variations in the pattern of the backscatter from the ground (‘ground scatter’) observed by the SuperDARN radars give information regarding the state of the ionosphere. In this thesis, ray tracing simulation of the observed ground scatter pattern for the mid-latitude SuperDARN radar at Blackstone, Virginia is implemented. An existing ray tracing code was modified, to incorporate the IRI-2007 model for electron density. This ray tracing code was used to simulate the ground scatter pattern observed at Blackstone in the year 2009. Simulations were compared with the observed ground scatter to assess our understanding of the ionospheric conditions. The IRI-2007 model is found to be adequate to predict the average ground scatter pattern observed through the year, including the winter anomaly. However, one deficiency with the IRI-2007 model is its inability to predict the sporadic E layer formation in summer and an anomalous evening enhancement in backscatter power observed in some months of the year, described here for the first time. Finally some suggestions are presented for the further improvement of the simulation methods for backscatter prediction.

I dedicate this thesis to my parents

Acknowledgements

First of all, I would like to thank my advisers Dr. Jo Baker and Dr. Mike Ruohoniemi for letting me be a part of the SuperDARN research group at Virginia Tech. I am greatly indebted to them for their support and guidance throughout the course of this thesis.
I would like to thank my lab mates in the SuperDARN project whose contributions where very relevant for this thesis. A special thanks to Dr. Lasse Clausen for providing me with the latest version of the ray tracing code from the Leicester University. I would also like to thank my committee members, Dr. Wayne Scales and Dr. Steven Ellingson for reviewing my work.

Thanks to my friend Jojo who inspired me to pursue graduate studies; my friend Jimmy for his priceless moral support during my initial days in USA and his valuable suggestions for debugging the code. I also want to thank Saritha, Ampili, Renjini, Arun and Syamala ma'm who have helped get through tough times. Without my roommates, Shambhavi, Pallavi and Navaneeta, life would have never been so enjoyable at Blacksburg. Thanks for all the fun and support.

I am indebted to my family for their love and trust in me and the support they have extended to all my endeavors.

List of Contents:

	Preface	ix
1	**INTRODUCTION**	1
1.1	The Ionosphere	1
	1.1.1 Variations with latitude	3
	1.1.2 Ionospheric layers	3
1.2	Electromagnetic waves in the ionosphere	6
1.3	Radio communication in ionospheric channels	8
	1.3.1 Multihop propagation	9
	1.3.2 Ionospheric phenomena in radio communication	10
1.4	Systems for ionospheric investigation	11
	1.4.1 GPS	11
	1.4.2 Radars	12
2	**RAY TRACING THEORY**	20
2.1	Ray Tracing	20
2.2	Wave Propagation through the ionosphere	22
2.3	Magnetoionic Theory	26
2.4	Propagation in an anisotropic medium	28
	2.4.1 Phase and group path	30
	2.4.2 Haselgrove's equations	32
2.5	Jones and Stephenson's code	33
2.6	Propagation effects at HF	35
3	**RAYTRACING APPLIED TO THE BLACKSTONE RADAR**	40
3.1	Radar Backscatter	40

3.2 Ray tracing code and the IRI model 41

3.3 Integrating the IRI -2007 model into the ray tracing code 47

3.4 Estimation of the ground scatter power from ray tracing 57

4 SIMULATION AND ANALYSIS OF THE GROUND SCATTER POWER, YEAR 2009 65

4.1 Seasonal variation of the ground scatter observed at Blackstone 66

4.2 Anomalous Behavior in the Blackstone ground scatter power 72

4.2.1 Winter Anomaly 72

4.2.2 Mid latitude Summer Night Time Anomaly (MSNA) 73

4.3 Simulation of the Ground Scatter Power using Ray Tracing 76

4.3.1 Winter Results 76

4.3.2 Spring Results 77

4.3.3 Summer Results 81

4.3.4 Autumn Results 83

5 CONCLUSIONS AND FUTURE WORK 86

Appendix A : Tables 89

Appendix B: The Ray Tracing Code 91

Appendix C: Doxygen for ray tracing code documentation 95

Appendix D: RTI plots from the ray tracing code 98

List of References 111

List of Figures:

Fig.1.1	Different layers of the atmosphere	2
Fig.1.2	Ionospheric layers	5
Fig.1.3	Electromagnetic waves in the ionosphere	7
Fig.1.4	Multi hop propagation	9
Fig.1.5	Fields of view of the SuperDARN radars in the northern hemisphere	16
Fig.1.6	Doppler velocity map	17
Fig.1.7	SuperDARN radar at Blackstone, Virginia under construction	18
Fig.2.1	An example of a ray tracing plot for the Blackstone radar	21
Fig.2.2	Refraction in a layered ionosphere	24
Fig.2.3	Cross-section of a wave front in an anisotropic, homogeneous medium	29
Fig.2.4	Block diagram showing important subroutines in the Jones Stephenson code	35
Fig.2.5	Ray plots for Blackstone radar shown to explain HF propagation effects	36
Fig.2.6	Ionospheric scatter vs. Ground scatter	38
Fig.3.1	Plot from the existing ray tracing code	42
Fig.3.2	Comparison of Ne height variations between ISR and IRI models for two mid-latitude locations	44
Fig.3.3	Electron density variations at the Blackstone radar location	46
Fig.3.4	Comparison of electron density profile obtained from ray tracing code and web tool for IRI provided by NASA	49
Fig.3.5	Diurnal and seasonal variations in ray paths	50-51
Fig.3.6	Time series plot of radar power measured at Blackstone on 02 Nov ‘09	53
Fig.3.7	Group path and ground range	54
Fig.3.8	Ray tracing plots for 02 Nov 2009 at 18:00 UT	57
Fig.3.9	Ray density histogram	58
Fig.3.10	Power histogram	59
Fig.3.11	Power plot for 02 Nov ’09 at 18:00 UT	60
Fig.3.12	Simulation for 02 Nov ’09 from 12 to 23 UT	60
Fig.3.13	Time series plot from radar measurements	61
Fig.3.14	Time series plot of median power per hour	62
Fig.4.1	Radar range-time plots from Jan to May ‘09	67
Fig.4.2	Radar range-time plots from June to Aug ‘09	69
Fig.4.3	Radar range-time plots from Sept to Oct ‘09	70
Fig.4.4	Electron density profile showing winter anomaly	73
Fig.4.5	Night time radar ground scatter plots from Mar through June ‘09	74
Fig.4.6	Comparison of radar data and simulation for winter	77
Fig.4.7	Comparison of radar data and simulation for spring	79

Fig.4.8	Ray tracing plot for April 2009	80
Fig.4.9	Comparison of radar data and simulation for summer	82
Fig.4.10	Comparison of radar data and simulation for autumn	83
Fig.B.1	Flow chart for ray tracing code	91
Fig.C.1	Caller graph of subroutine ‘readw’	95
Fig.C.2	Call graph for function ‘readw’	96
Fig.C.3	Call graph for function ‘rindex’	97

Preface

The SuperDARN radar at Blackstone has been operational since February 2008. The pattern of backscatter measured from the ground at the radar helps in remote sensing the state of the ionosphere. The 'ground scatter' observed at Blackstone shows a consistent trend through the day and through the seasons. Hence it was decided to simulate the pattern of ground scatter, using a ray tracing code incorporating the IRI-2007 model for electron density, and compare the simulated pattern with the observation to assess our understanding of the ionosphere and the performance of the radar. This work is presented in this thesis.

This thesis is organized into 5 chapters.

Chapter 1 gives a general introduction to the ionosphere and the propagation of electromagnetic waves through the ionosphere. A few systems used for the ionospheric investigation, including the SuperDARN radar, are introduced.

Chapter 2 is a theoretical introduction to the ray tracing, which is the technique used for predicting ray propagation through the ionosphere. The Jones and Stephenson's ray tracing code is introduced and the ionospheric scatter and ground scatter measured at the radar are explained.

Chapter 3 details the implementation aspects of introducing the IRI-2007 model for electron density to the existing ray tracing code. The step by step procedure for producing the simulated ground scatter plots from the ray tracing code is also explained.

Chapter 4 presents the analysis of the seasonal and the diurnal ground scatter pattern observed at Blackstone in 2009 and the measurements are compared with the simulated results.

Chapter 5 makes conclusions about the efficiency of using the IRI-2007 to model the electron density at the Blackstone radar location and suggests further improvements possible for the ray tracing code.

Chapter 1

Introduction

1.1 The Ionosphere

The atmosphere is a layer of gases surrounding the earth that is retained by earth's gravity. The atmosphere is classified into different layers based on the temperature, dominant physical processes or on chemical composition [1]. Based on temperature distribution, the atmosphere is divided into 5 layers: Troposphere, Stratosphere, Mesosphere, Thermosphere and Exosphere (in the order of lowest to highest altitude). Figure 1.1 shows the approximate altitude of these layers. The troposphere is the lowest part of the atmosphere and is mainly heated by transfer of heat from the Earth's surface. Hence temperature decreases with altitude. In the stratosphere, the temperature increases with height whereas in the mesosphere, temperature decreases with height. Temperature increases with height in the thermosphere. It is in the thermosphere where we typically see the auroras. The exosphere is the outermost layer and is mainly composed of hydrogen and helium.

The ionosphere may be defined as the part of earth's upper atmosphere where ions and electrons are present in quantities sufficient enough to affect the propagation of radio waves. It stretches from about 60 km to about 500-600 km [2]. This region exists in a weakly ionized plasma state. Ionization depends primarily on solar illumination. Photons at the frequencies of Ultraviolet, X-Ray and shorter wavelengths of solar radiation are capable of ionizing neutral gas. As gas density

increases at lower altitudes, the recombination process prevails, since the gas molecules and ions are closer together.

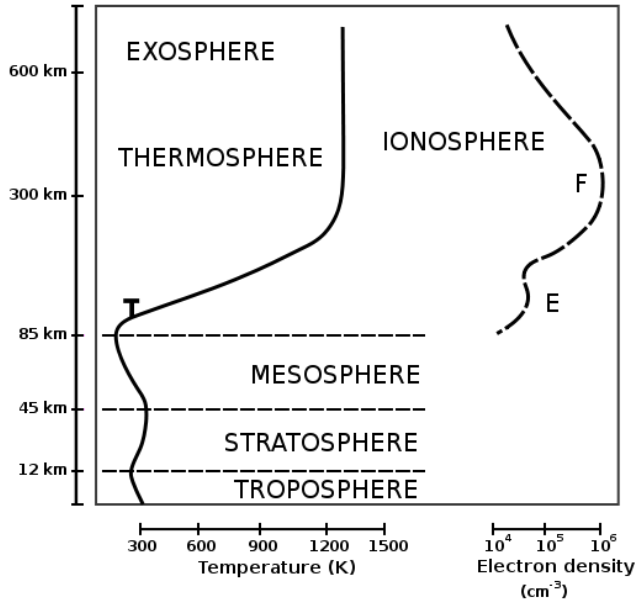

Figure 1.1: Different layers of the atmosphere; the magnetosphere is not shown in this picture; but it starts at the upper boundary of the ionosphere and exists in a strongly ionized plasma state [1]

The upper bound of the ionosphere is determined as the altitude at which the concentration of the charged particles of plasma exceeds that of neutral molecules and atoms. At these altitudes, the ionosphere transforms continuously into the magnetosphere, which consists of only strongly ionized plasma (absence of neutral molecules and atoms) and strong ambient electric and magnetic fields. The balance between the ionization and the recombination, the electron and ion precipitation from the magnetosphere, the diffusion processes and the plasma convection in the crossed electric and magnetic fields determines the quantity of ionization present in the ionosphere [1].

1.1.1 Variations with latitude

Since the ionosphere is mainly controlled by solar illumination, it undergoes changes diurnally. Apart from this diurnal variation, changes are observed in the ionosphere as we move along the geomagnetic latitudes.

The terrestrial ionosphere may be divided into 3 broad regions that have different properties according to their geomagnetic latitude [3]:

The low latitude zone, spanning 20° or 30° on either side of the magnetic equator is strongly influenced by electromagnetic forces that arise because the geomagnetic field lines are nearly horizontal near the magnetic equator. The primary consequence is that the electrical conductivity is abnormally large over the equator [4].

In the mid latitude region, between 30° and 55°, ionization is produced almost entirely by energetic ultraviolet and X-ray emissions from the sun, and is removed again by chemical recombination process that may involve the neutral atmosphere as well as ionized species.

At high latitudes, greater than 55°, the geomagnetic field lines are nearly vertical and hence lead to an ionosphere which is more complex than that in the low- latitude or mid–latitude regions. The magnetic field lines connect the high latitude ionosphere to the outer part of the magnetosphere which is confined by the streaming solar wind plasma, whereas the ionosphere at the low and mid–latitude is connected to the inner magnetosphere, which rotates with the earth and is less sensitive to external influences.

1.1.2 Ionospheric layers

Solar radiation, acting on the height-dependent composition of the atmosphere, generates different ionized layers. The 3 distinct layers of the ionosphere are D (present only during day

time), E and F. The F layer is further subdivided into F1 and F2 during day time (depicted in Figure 1.2).

Approximate altitude ranges of the ionospheric regions are [5]:

- D region : 50 to 90 km
- E region : 90 to 140 km
- F1 region : 140 to 210 km
- F2 region : over 210 km

The electron density during the day usually increases more or less uniformly with altitude from the D region, reaching a maximum in the F2 region. Electrons and ions move differently at these heights in the presence of external electric and magnetic fields. In the F-region, the motion of both electrons and ions are dominated by the electric and magnetic field and they drift in the $\overline{\boldsymbol{E}} \times \overline{\boldsymbol{B}}$ direction [6]. (The electric field, $\overline{\boldsymbol{E}}$, is a result of magnetospheric and ionospheric dynamic processes; and the charged particles drift in a direction perpendicular to both $\overline{\boldsymbol{E}}$ and $\overline{\boldsymbol{B}}$). At the bottom of the E region, due to the ions having frequent collisions with neutrals, they are not affected (to a first approximation) by the magnetic field; only electrons move in the $\overline{\boldsymbol{E}} \times \overline{\boldsymbol{B}}$ direction. At these heights, a relative motion between electrons and ions exists (electric current), and it can easily be detected by observing the magnetic effects of the electric current. In the D region, both electrons and ions are collisionally dominated so that there is almost no effect on their motion by the electric field.

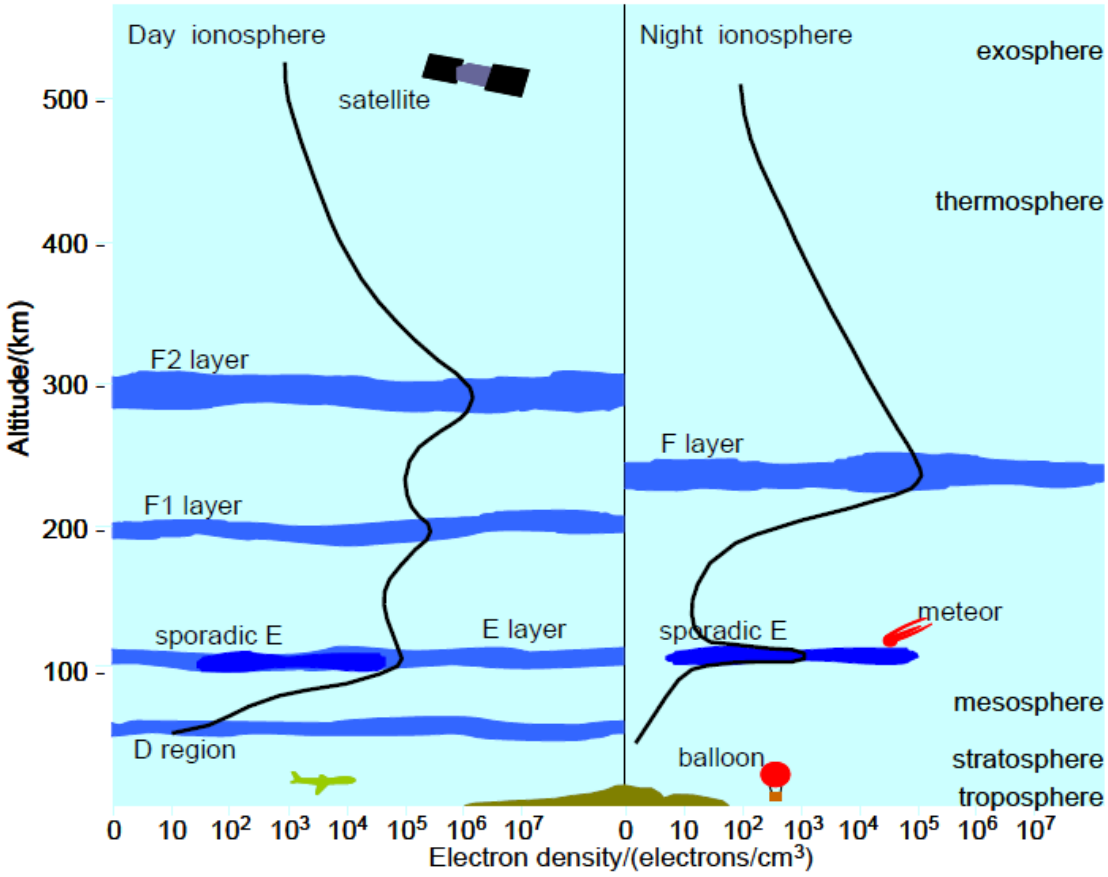

Figure 2.2: Ionospheric layers [4]

Sporadic E refers to the largely unpredictable formation of regions of very high electron density in the E region. Sporadic E may form at any time during the day or night occurring at altitudes of 90 to 140 km (the E region). It varies greatly in the area it covers (a few km to hundreds) and the time it persists for (minutes to many hours). At high latitudes, sporadic E tends to form at night. Sporadic E in the low and mid-latitudes occurs mostly during the daytime and early evening, and is most pronounced during the summer.

1.2 Electromagnetic waves in the Ionosphere

A brief note on the theory of behavior of electromagnetic waves in the ionosphere is given below [7].

When an electromagnetic wave enters an ionized medium, its alternating electric field induces oscillations in the charges. The amplitude of this oscillation is opposite in phase to the alternating field. The amplitude of the oscillation, x_0 is given by

$$x_0 = e E_0 / (m \omega^2)$$

where, m and e are mass and charge of the particle, ω is the angular frequency of oscillation and E_0 is the average value of electric field.

The oscillation of electrons is much larger than that of ions (due to inverse mass dependence). Also, the higher the frequency, the lesser the time there is for acceleration of charge and the smaller the amplitude obtained.

The oscillating electrons emit secondary waves, which have the frequency of the primary wave; but are shifted in phase. The secondary waves from different electrons interfere with each other and finally produce two plane secondary waves: one in, and another opposite to, the direction of the primary wave. The resultant wave is the vector addition of the primary and the secondary waves. The contributions from different depths of the ionosphere tend to cancel out the various secondary waves. However when the electron density reaches a critical value, which depends on the frequency, the phase changes so rapidly that the backward directed secondary waves become phase-coincident. In this case, the forward wave is dampened very rapidly and the secondary backward directed waves get more energy. This means that the incident wave is reflected.

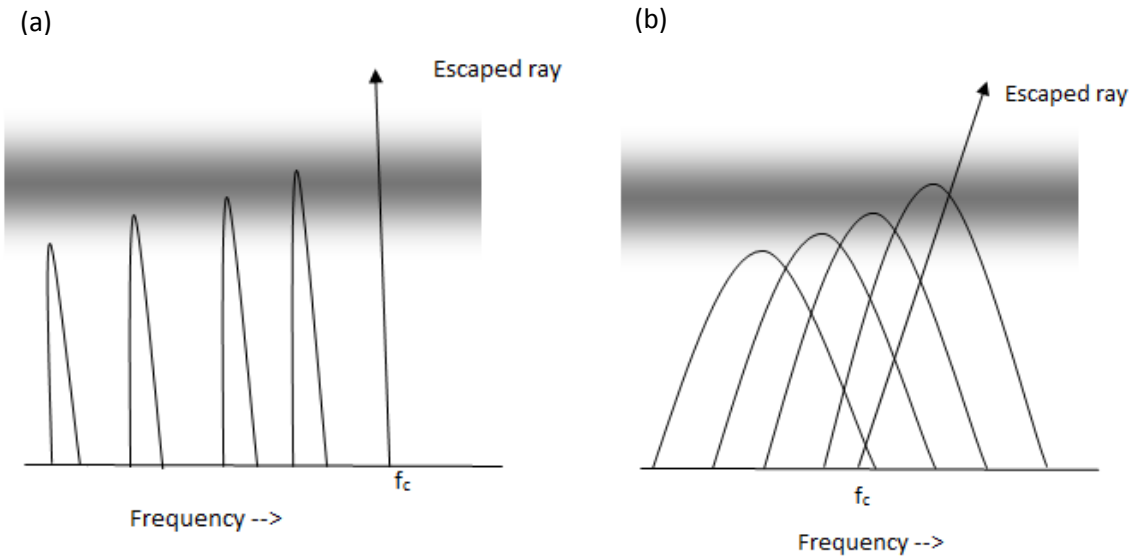

Figure 1.3: Electromagnetic waves in the ionosphere; Rays with the same elevation angle at different frequencies are shown (a) Vertical Incidence- rays refracted from the ionosphere hit the ground at the transmitter (b) Oblique Incidence – rays refracted from the ionosphere reach distant points from the transmitter

When an HF electromagnetic wave (3 – 30 MHz) enters the ionosphere, the free electrons and ions cause the wave that is moving upward to bend back towards the Earth due to refraction. Figure 1.3.a shows radio waves incident at a normal angle to the ionosphere. As we can see, the lower frequencies are reflected from lower altitudes where the electron density is less. The higher the frequency of the wave, the greater is the height from which it is reflected from the ionosphere. The frequency of propagation for which the wave penetrates the ionosphere is called the *critical frequency*, f_c. Figure 1.3.b shows waves incident at an oblique angle. This case is similar to Figure 1.3.a except that, reflection allows the signals to travel back down to the surface at ranges well over the horizon to reach distant points, giving HF radiation its unique long range characteristics. The concept of critical frequency applies to oblique propagation also.

1.3 Radio communication in Ionospheric channels

Radio waves are electromagnetic waves of wavelength 10^{-3} m and higher. Their frequency range is from a few kHz to a few hundred MHz. Radio frequency bands are given in Table 2. The propagation of radio waves is important in many modern forms of communication like radio, television, microwaves etc.

When radio waves encounter the ionosphere, they can get refracted/reflected back to the earth, escape through the ionosphere or get absorbed. These phenomena are a function of wave frequency, angle of incidence (measured form normal to the ionospheric plane) and electron density [8, 9].

The D layer reflects some VLF and LF waves, and absorbs MF and HF frequencies to a certain extent. Hence it has a negative impact on radio communication as it absorbs radio energy, particularly those frequencies below 7 MHz. The E layer can only reflect radio waves having frequencies less than 5 MHz. Sporadic E can have a comparable electron density to the F region which means it can reflect the sort of high frequencies intended for F region communications. Sometimes a sporadic E layer is transparent and allows most of the radio wave to pass through it to the F region, however, at other times the sporadic E layer obscures the F region totally and the signal does not reach the F region and hence the receiver (sporadic E blanketing). If the sporadic E layer is partially transparent, the radio wave is likely to be reflected at times from the F region and at other times from the sporadic E region. This may lead to partial or intermittent transmission of the signal or fading.

The F1 layer reflects radio waves up to 10 MHz. The F2 layer can reflect waves up to 50 MHz and during a sunspot maximum, this maximum reflected frequency can go up to 70 MHz. The F

region is most important in HF communication as its high altitude allows longest communication paths and reflects the highest frequencies in the HF range [5, 10].

1.3.1 Multi-hop propagation

Multi-hop propagation (also known as sky wave or ionospheric skip) uses HF radio waves (3-30 MHz), which can be reflected by both the ionosphere and the earth's surface. (The sky waves are also called short waves.) A single hop of the wave may not be sufficient for the transmitted wave to reach the receiver. Since earth's surface is conductive, the HF waves can be reflected back to the ionosphere thereby giving multiple hops of the single wave. This is shown in Figure 1.4.

Not all the HF waves are reflected by the ionosphere: there are upper and lower frequency bounds for communication between two terminals. If the frequency is too high, the wave will pass straight through the ionosphere. If it is too low, the strength of the signal will be very low due to absorption in the D region. The range of usable frequencies will vary throughout the day, with the seasons, with solar cycle and from place to place. The lower limit of frequency is also dependant on receiver site noise, antenna efficiency, transmit power and ionospheric absorption.

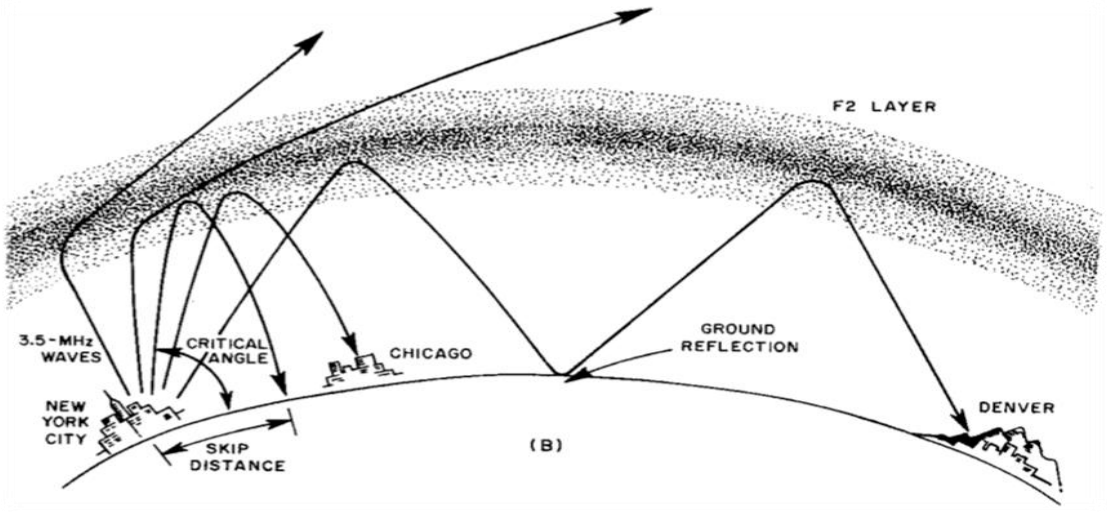

Figure 1.4: Multi hop propagation [9]

Propagation distance also depends on the angle at which the wave enters the propagation medium (in HF, the ionosphere). This angle is called the angle of incidence. As the angle of incidence increases, the amount of wave refraction decreases. The maximum angle of incidence below which radio waves of a certain frequency are refracted and reflected back to the earth is called the *critical angle*. For Blackstone radar simulations, we are considering only the single hop propagation mode.

1.3.2 Ionospheric phenomena in radio communication

Ionospheric perturbations affect radio and satellite communication. Absorption, scattering and fading are a few phenomena relevant in radio communication [11]. These phenomena are relevant in the radar wave propagation also.

Absorption: Due to interaction with charges in the ionosphere, the radio wave experiences absorption. Energy of the electromagnetic wave is transferred to the particles and appears as thermal energy.

S**cattering:** The ionospheric scattering can be classified as strong or weak in terms of received signal strength of the scattered wave at the receiving radar antenna. Another way of classifying scattered echoes is in terms of their backscatter cross-section and their temporal stability.

Fading:

Satellite communication experiences complications from plasma structures in the ionosphere. Plasma density irregularities cause additional losses compared to those observed when the ionospheric plasma is a uniform, homogeneous, regular-layered medium and also causes multipath fading of the signal strength observed at the receiver. The communication signal experiences temporal deviations when passing through a multipath channel (multipath occurs

due to stratified ionosphere; the signal reflected from different layers of the ionosphere or irregularities of the ionosphere give rise to multipath signals having different phase shifts). At the receiver, such random-phased waves from different paths combine vectorially to give an oscillating resultant signal, the character of whose variations depends on the distribution of phases among the incoming component waves. The signal amplitude random variations are known as fading effect.

From the above discussion, it can be concluded that study of the highly variable environment of the ionosphere is necessary to obtain high efficiency in HF communication. Apart from radio communication, ionospheric irregularities affect operation of power grids, OTH radars, GPS etc.

1.4 Systems for ionospheric investigation

A variety of radio-physical systems such as optical devices, coherent and incoherent scatter radars, Global Positioning System (GPS), ionosondes, etc., are employed today for the study of ionosphere [8]. A brief review of a few of these systems is presented in this section.

1.4.1 GPS

The GPS consists of 24 medium earth orbiting satellites in six different orbital planes. These satellites travel roughly at a speed of 7,000 mph with transmit power of 50W or less. GPS is currently the most used satellite navigation system in the world.

GPS signals, like any other satellite signals are greatly affected by the ionosphere. Hence GPS turns out to be a powerful tool for remote sensing of the ionosphere.

Hajj and Romans (1998) demonstrated the use of GPS in obtaining profiles of electron density and other geophysical variables such as temperature, pressure and water vapor in lower

ionosphere. They are also useful in measuring the Total Electron Content (TEC) along signal path in presence of ionospheric irregularities.

1.4.2 Radars

Radar uses radio waves to identify the range, altitude, direction or speed of objects. When a radar signal comes in contact with a target, it is scattered. The signal which is partially reflected back to the radar (referred to as backscatter) is measured and the location of the target is determined from the round trip delay time for the signal. Also, if the target is moving, the returned signal is shifted in frequency and the measurement of this Doppler shift gives the velocity of the target.

One form of the radar equation is given by [8]

$$P_r = \frac{P_t G_t A_r \sigma F^4}{(4\pi)^2 R_t^2 R_r^2}$$

where

P_r : Receiver Power

P_t : Transmitter power

G_t : Gain of transmitting antenna

A_r : Effective aperture area of receiving antenna

σ : Radar cross section

F: Propagation factor

R_t & R_r: Distance of target from transmitting and receiving antennas. In case, transmitter and receiver are co-located, $R_t = R_r$ = range

Ionospheric radars can be broadly classified into coherent and incoherent scatter radar [3]. A brief description of both radars is given below.

Incoherent Scatter Radar

Electrons in random thermal motion will scatter signals whose phases are varying with time and are not related to one another. At the radar receiving antenna, the signals will add and give a very low level echo.

It turns out that the backscatter from the ionosphere is actually due to the local fluctuations in the electron density at the thermal level, instead of pure scatter from free electrons. Evans (1969 and 1972) presented the essentials of incoherent-scatter theory and practice and salient equations are given by Krall and Trivelpiece (1973). Incoherent scatter radars (ISR) are mainly used for the study of the lower ionosphere out to ranges of a few hundred kilometers.

Since incoherent scatter radars capture weak echoes, they need high sensitivity and power for their operation and hence are very expensive. One of the oldest incoherent scatter radar in use is Jicamarca in Peru for study of equatorial ionosphere. A few of the other major ISR are Millstone Hill in USA, EISCAT (European Incoherent SCATter Association) and Svalbard radar in Scandinavia.

Coherent Scatter Radar

When plasma instabilities are present in the ionosphere, the amplitude of fluctuations in the medium grows to much higher levels than the thermal background. This results in coherent backscatter which has cross-sections many orders of magnitude larger than that of incoherent scatter. Coherent backscatter is generally 40-90 dB stronger than incoherent scatter. Hence these radars need lower power and sensitivity for operation and are cheaper than incoherent scatter radars.

Coherent backscatter is obtained when the ray path from the transmitting antenna intersects large electron density gradients or magnetic field-aligned irregularities, at or near perpendicular

incidence to the local magnetic field. The first quantitative description of the coherent scatter from the ionospheric irregularities was published by Booker (1956), when he derived a theory to describe the backscatter from the field aligned irregularities in the auroral E region. The results are also applicable to the backscatter from the F region irregularities.

Modern coherent radars use HF and VHF bands and use continuous wave or pulse coded modulation. In the propagation mode known as the ground scatter, the echoes reflected by the ionosphere are scattered by the ground and some power returns to the radar through the ionosphere, whereas in the direct backscattering mode, the echo comes directly reflected from the irregularities in the ionospheric plasma. This distinction between the direct backscatter and the ground scatter is further explained in section 2.4. The velocity, spectrum and intensity of the echo is analyzed to study the nature of the plasma irregularities. A good example of the HF coherent scatter radar is the SuperDARN. A brief description of the SuperDARN radars is given below.

Super Auroral Radar Network (SuperDARN)

This section gives a brief overview of the significance of the SuperDARN radar, about the SuperDARN collaboration, the radar construction, the mode of radar operation and also a brief description of the radar observations.

The SuperDARN is a network of HF coherent scatter radars, designed to study plasma convection and irregularities over the high latitude region. A combination of reconnection and viscous processes occurring at the magnetopause are responsible for creating large-scale electric fields. These fields map down geomagnetic field lines into the high-latitude ionosphere where they cause the plasma to drift in $\overline{\boldsymbol{E}} \times \overline{\boldsymbol{B}}$ direction (as discussed in Section 1.1). The movement of

the particles is thus tied to the earth's magnetic field lines. By measuring the motion of this ionospheric plasma it is, therefore, possible to infer a great deal about the magnetospheric processes that are responsible for the convection and also about disturbances in the Earth's near-space environment that are collectively referred to as the space weather [11].

The SuperDARN radars observe backscatter from decameter-scale ionospheric irregularities. The SuperDARN radars utilize ionospheric refraction to achieve orthogonality with the magnetic field aligned irregularities in the high latitude F region, i.e., the ray may start at an oblique angle, but due to continuous refractions, it may attain orthogonality to the local magnetic field in the F region. Since the ionospheric irregularities are aligned with the magnetic field, finding their velocity reduces to a 2-dimensional velocity determination. The Line of Sight (LOS) velocities measured by the dual radars are combined to determine the vector velocity of the irregularities. The SuperDARN observations are used for locating the ionospheric irregularities, plasma diagnostics, and the study of the $\overline{\boldsymbol{E}} \times \overline{\boldsymbol{B}}$ drift of the ionospheric plasma.

SuperDARN is an international collaboration between numerous universities and funding agencies. The SuperDARN consists of over 21 radars operating on frequencies between 8 and 20 MHz. A list of SuperDARN radars is given in Table 2. The field of view of the radars in the northern hemisphere is given in Figure 1.5.

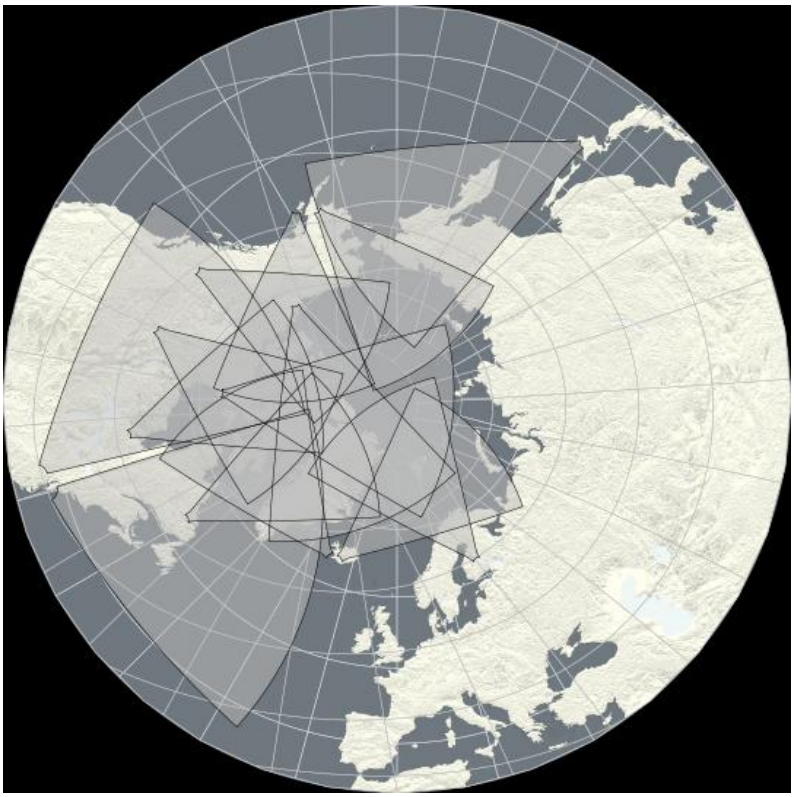

Figure 1.5: Fields of view of the SuperDARN radars in the northern hemisphere

The construction of all radars is almost identical. Each radar consists of two antenna arrays, a main array of 16 antennas with both transmit and receive capability and an interferometer array of 4 antennas with receive capability only. Appropriate phasing of the main array antennas creates 16 narrow beams, each covering only about 4°, the total azimuthal coverage being 52° [12].

SuperDARN radars use multipulse sequence, to determine Doppler characteristics of different targets at multiple ranges by using the Autocorrelation Function (ACF) of the received samples. Many sequences are transmitted and the calculated ACFs integrated over a period to minimize the effect of noise. The final average ACF is used to calculate backscatter power, spectral width and Doppler velocity of plasma irregularities. In a standard operating mode, a multipulse

sequence (of seven pulses) is transmitted and sampled to resolve 75 ranges with a 45 km separation [10].

Figure 1.6 shows a Doppler velocity map from the Kapuskasing radar. As explained earlier, analysis of LOS velocities from the multiple radars produces a two dimensional pattern of the ion drifts.

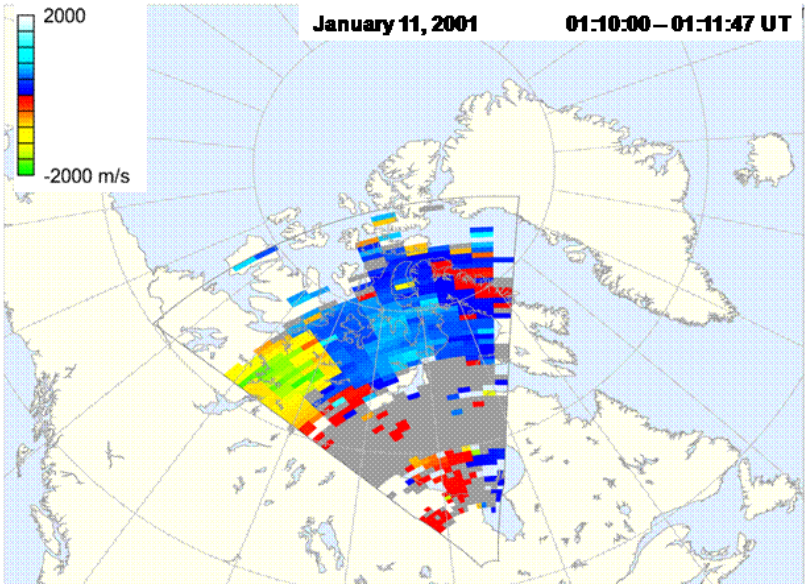

Figure 1.6: Doppler velocity map showing color coded Line of Sight Doppler velocities of the targets (ionospheric irregularities) measured by 16 beams; the blue colors represent velocity towards the radar ; yellow colors represent velocity away from the radar and the grey color represent zero velocity which is essentially from ground scatter

The Doppler velocity map shows the velocity of the target measured in the field of view of the radars by 16 beams. The gray patch in the velocity plot shows ground scatter. The simulation of this ground scatter is the major work of this thesis. We can see that there is no major difference as we move across the beams; hence data from a single central beam, beam 8, which looks at an azimuth of 335° due North is used for our simulations.

SuperDARN was first built in the 1990s as a chain of radars ringing the auroral latitudes and pointing towards the poles. This was sufficient for studying such phenomena as the magnetospheric substorm, which occurs frequently and is mostly confined to auroral latitudes. Powerful magnetic storms, however, which occur much less often but have more serious effects, can trigger very large disturbances in the space environment and can cause auroras to be seen even in the mid-latitude. The impacts get even more significant at the mid-latitudes since more people live there and the density of vulnerable technology is greater. So the SuperDARN collaborators decided to begin installation of a chain of mid-latitude radars, which is sometimes referred to as StormDARN, to study the magnetic storm electric fields. The mid-latitude radar at Blackstone (37.1° N, 77.9° W), Virginia falls under this category.

The radar is located at the Virginia Tech University's Blackstone Agricultural Research and Extension Center and has been operational since February 2008.

Figure 1.7: SuperDARN radar at Blackstone, Virginia under construction in Jan, 2008

The SuperDARN research group at Virginia tech is responsible for radars located at Blackstone (Virginia), Goose Bay (Canada), Kapuskasing (Canada),Wallops Island (Virginia) and two new radars at Hayns (Kansas). In the study presented in this thesis, ground scatter measured at the Blackstone radar is what we have tried to simulate.

Chapter 2

Ray Tracing Theory

In the first chapter, an introduction to wave propagation through the ionosphere and an overview of the radar devices deployed for the study of the ionosphere including SuperDARN radar were given. This chapter deals with ray tracing through the ionosphere, which is the theory behind radio wave propagation prediction.

2.1 Ray Tracing

Ray tracing is a method for calculating the path of electromagnetic waves through a system with regions of varying propagation velocity, absorption and reflection.

Ray tracing involves determining the path of an electromagnetic signal by the successive application of ray theory over a series of thin homogenous slabs of the medium. It requires that the wave parameters such as polarization and refractive index do not change appreciably within a wavelength. Accurate ray tracing requires detailed knowledge of the state of the ionosphere.

Ray tracing is widely employed in the study of radio waves through the ionosphere. Radio signals are modeled as rays and traced through the ionosphere where they are reflected or refracted back to the earth. Ray tracing has been extensively used for the prediction of HF communication as well as Over-The-Horizon radar applications. An example of a ray tracing plot is given below in Figure 2.1, which shows a plot of altitude vs. ground range from the transmitter. The origin represents a transmitter emitting rays with elevation angles from 5° to 35° in steps of 5° for a constant transmit frequency of 11 MHz. The background electron density is

simulated using the empirical model IRI-2007, the details of which are elaborated in Section 3.2. This electron density values are for 02 November 2009 at 18:00 UT. We can see that the ionosphere starts at 60 km which represents the D region. As we move along in altitude, we can see that the ionosphere builds up, i.e., the electron density keeps increasing till it reaches a maximum near 250 km. This is indicative of the different ionospheric regions – D (60 to 90 km); E region (from 90 to 140 km) and F region (above 140 km) described in Section 1.1.

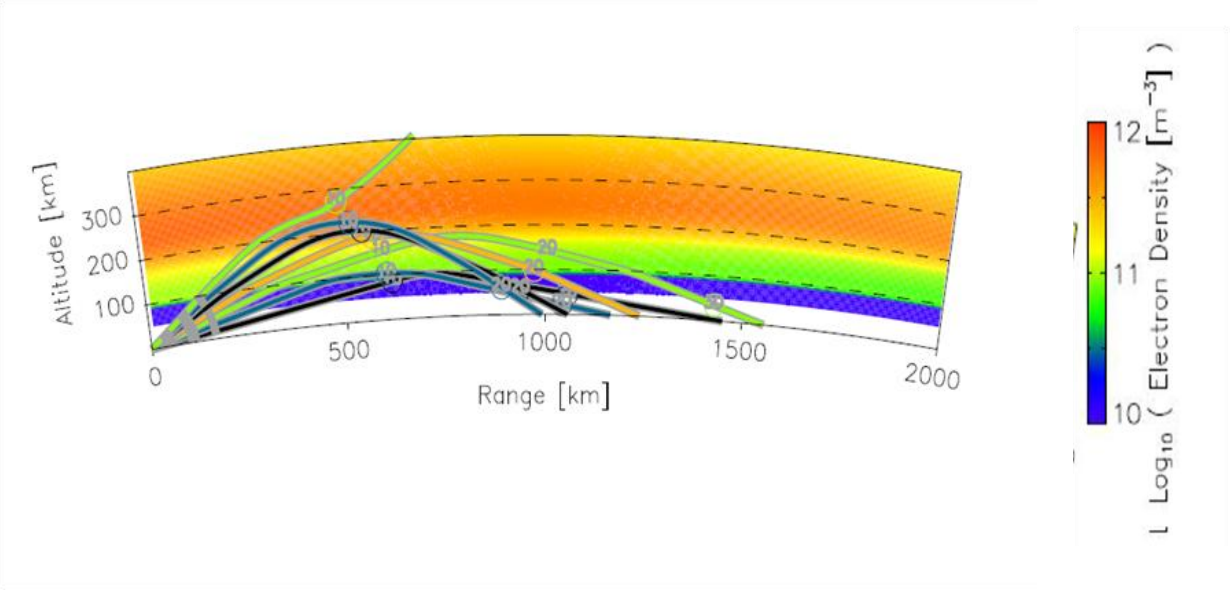

Figure 2.1: An example of a ray tracing plot for the Blackstone radar. This simulation is done for Blackstone radar on 11-02-2009 at 18:00 UT. Rays of elevation angle from 5° to 35° in steps of 5° at a constant transmit frequency of 11 MHz are shown; Electron density is represented by the IRI model.(In the figure, the background electron densities are color coded; rays of different elevation angles are shown using different colors)

In the figure, rays of different elevation angles are shown with different colors. When the rays encounter the ionosphere, they gradually start bending horizontally and can get refracted back to the Earth. It can be seen that the lower elevation angles (5° and 10° indicated by the lowest black and blue lines) get refracted from the D region, the higher angle rays (15° to 30°) travel to

greater heights and are reflected from the E and F regions. In the figure, the ray with the highest elevation angle, which is 35°, is somewhat deflected but ultimately penetrates the ionosphere and never returns to the Earth. This corresponds to the critical angle, defined in Section 1.3.1.

2.2 Wave propagation through the ionosphere

When a radio wave travels through the ionosphere, its electric field imparts an oscillatory motion to the electrons, which re-radiate like miniature antennas. If the magnetic field were absent, the oscillatory motion of the electrons would be parallel to the electric field of the incident wave and the re-radiated wavelets would have the same polarization as the incident wave. Hence the composite wave that results when these wavelets add to the original wave has the same polarization as that of the incident wave [15, 16].

When the earth's magnetic field is considered, the oscillatory motion of the electron is modified. The charged particles re-radiate wavelets in which the electric field rotates. The composite wave has its electric field rotating so that the polarization can be different from that of the original wave.

If the original wave makes the charges rotate in the same way as its own rotation, they produce a composite wave whose field also rotates in the same way. In this case, the polarization has not been changed and the resulting wave is called an ordinary wave. A second wave is possible in which the rotation is in the opposite sense and is called the extraordinary wave. Thus in the presence of the Earth's magnetic field, there would be an extraordinary wave through the ionosphere whose polarization is different from that of the incident wave.

In its passage through the ionosphere, a radio wave imparts energy to electrons. The constituents of the ionosphere are in continuous random motion and consequently collisions between electrons and heavier particles occur. When such a collision happens, the wave is attenuated. The higher the frequency of the collisions, the greater is the attenuation.

Reflection at oblique incidence

If the effects of earth's magnetic field and collisions are ignored, then the refractive index μ of the ionosphere is given by [16]

$$\mu^2 = 1 - (f_N/f)^2 \qquad (2.1)$$

where f is the wave frequency and f_N is the plasma frequency which is proportional to the square root of electron concentration. $f_N = 2\,\pi\omega_N$, where ω_N is given by the relation

$$\omega_N = \sqrt{\frac{n_e e^2}{m\varepsilon_0}}$$

where n_e is the number density of electrons, e is the electric charge, m is the effective mass of electron and ε_0 is the permittivity of free space. Thus from the equation, it can be seen that as the density of the electrons in the ionosphere increases, the frequency which is reflected increases. This is consistent with the sketch in Figure 1.3 as the density of ionosphere increases with height.

Below the ionosphere, the refractive index is unity. A ray ascending into the ionosphere encounters a region where the refractive index gradually falls as the electron concentration increases with height as shown in Figure 2.2. The ray gets refracted as it progresses though regions of varying refractive index. By Snell's law, when the ray travels from one region to

another of lower refractive index, it bends more towards the region of higher refractive index. The higher the electron density, the more the bending of the ray. If the ionized layer is sufficiently dense, refraction will continue until the angle of refraction reaches 90°. The ray will have then reached its apogee (highest point) and will be reflected back to earth. In practice, the variation of the electron concentration is continuous and hence the path of the ray will be a continuous curve.

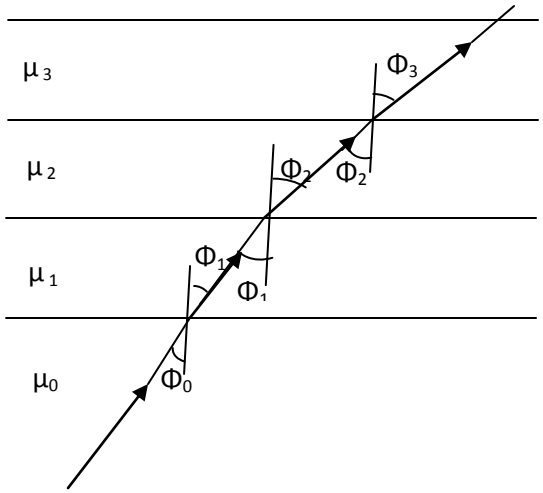

Figure 2.2: Refraction in a layered ionosphere, where each layer is assumed to have constant electron density and hence constant refractive index. As we go higher, the electron density increases and hence refractive indices gradually fall i.e. $\mu_0 > \mu_1 > \mu_2 > \cdots$ [1] The ray gets refracted. At each layer, the ray bends towards the lower layer as it is of higher refractive index, until at apogee where angle of refraction reaches 90°.

For simplicity, consider the ionosphere to be divided into a number of thin strips of constant electron density, with each strip having greater electron density than the one beneath it. The successive refraction at the boundaries between the layers will cause bending of the ray as shown in Figure 2.2.

Applying Snell's law at the boundary of each strip gives

$$\mu_o \sin\phi_0 = \mu_1 \sin\phi_1 = \cdots = \mu_n \sin\phi_n \qquad (2.2)$$

Thus a ray entering the ionosphere at an angle of incidence ϕ_o will be reflected at a height where the ionization is such that $\mu = \sin\varphi_0$ (We get this by substituting μ_o=1 (for region below ionosphere) and ϕ_n = 90° (for the condition at refraction) in equation 2.2)

At vertical incidence, φ_0= 0°. Substituting for φ_0 in $\mu = \sin\varphi_0$, we get $\mu = 0$. This is the condition for reflection for a ray at vertical incidence. From Equation 2.1, this occurs where f=f_N.

For oblique incidence, $\varphi_0 > 0°$. The condition for reflection is given by

$$\sin^2\phi = 1 - (f_N/f)^2 = 1 - (f_v/f)^2$$

where f_v, represents the vertically incident frequency reflected at the level where the plasma frequency is f_N. Hence $f = f_v \sec\phi_0$

Thus a frequency f incident on the ionosphere at an angle ϕ_0 will be reflected from the same electron density as the equivalent vertical incidence frequency $f_v = f\cos\phi_0$; hence a given ionospheric layer will always reflect higher frequencies at oblique incidence than at vertical incidence.

Now we have seen that the propagation of the ray depends on the refractive index of the medium which in turn depends on the electron density. The next section describes Appleton Hartree equation used to find the refractive index of the medium from the ionospheric parameters.

2.3 Magnetoionic Theory

The theory of wave propagation in an ionized medium in the presence of a magnetic field was developed by Lorentz to explain passage of light through crystals [15]. However, when applied to radio wave propagation in the ionosphere, this theory failed to explain some observed features. The modified form developed by Appleton and Hartree is now known as magnetoionic theory. The Appleton Hartree formula is used to find the refractive index of the ionosphere.

Appleton Hartree equations

The Appleton Hartree theory applies for a medium which is electrically neutral with no resultant space charge and equal numbers of electrons and positive ions. A uniform magnetic field is assumed and the effect of positive ions on the wave is neglected.

The complex refractive index, μ, at angular frequency ω is given as [15, 17]

$$\mu = 1 - \frac{X}{1 - iZ - \frac{Y_T^2}{2\,(1 - X - iZ)} \pm \left(\frac{Y_T^4}{4(1 - X - iZ)^2} + Y_L^2 \right)^{1/2}} \qquad (2.3)$$

where

$X = \frac{Ne^2}{\varepsilon_0 m \omega^2}$

$Y_L = \frac{eB_L}{m\omega} = Y \cos\Theta$

$Y_T = \frac{eB_T}{m\omega} = Y \sin\Theta$

Θ is the angle between wave normal and $-B_0$

$Z = {}^{\upsilon}/_{\omega}$

$i = \sqrt{-1}$

N is the electron concentration, e and m are the electronic charge and mass and ε_0 is the permittivity of free space. υ is the electron collision frequency. The subscripts T and L refer to the transverse and longitudinal components respectively to the Earth's magnetic field B with respect to direction of wave normal.

The presence of '±' sign in the equation gives two separate solutions for the refractive index. The '+' sign represents the refractive index for the ordinary wave and the '-' sign represents the refractive index of the extraordinary wave.

The corresponding wave polarizations R are

$$R = \frac{i}{2Y_L}\left[\frac{Y_T^2}{1-X-iZ} \mp \left(\frac{Y_T^4}{(1-X-iZ)^2} + 4\,Y_L^2\right)^{1/2}\right] \quad (2.4)$$

From the Equation 2.3, we can infer that

- Below the ionosphere, the refractive index is unity. For a given wave frequency, refractive index decreases with increasing electron concentration and for a given electron concentration, refractive index decreases with increasing wave frequency. If N is sufficiently large, then ignoring the magnetic field and collisions, μ will become zero and X = 1 at the height of refraction at vertical incidence (this is in agreement with what we saw in Section 2.2); otherwise the wave traverses the whole ionosphere and escapes. Hence for frequency f at reflection, N satisfies

$$f^2 = \frac{Ne^2}{4\,\pi^2\,\varepsilon_0 m}$$

- In the presence of a magnetic field, the ordinary wave is reflected as if the field were absent , but the extraordinary wave at HF is reflected from a lower height where

$$X = 1 - Y \text{ with } \quad Y^2 = Y_L^2 + Y_T^2$$

From Equation 2.4, in general, the wave polarization is elliptical with the ordinary and extra ordinary waves having equal axial ratios but opposite senses of vector rotation. In the case of no collisions, i.e. Z = 0, the two waves will have orthogonal wave major axes. With longitudinal propagation i.e. $(Y_T^4) >> 4(1-X)^2 Y_L^2$, the two magnetoionic waves are circularly polarized. With transverse propagation, i.e. $(Y_T^4) << 4(1-X)^2 Y_L^2$ the ordinary wave is linearly polarized with its electric vector parallel to the imposed magnetic field.

In the presence of collisions, the major axes of the polarization ellipses of the ordinary and the extraordinary waves are no longer orthogonal. In this case, the refractive index is a complex number.

Once the value of refractive index is known, the path of the ray through the ionosphere can be predicted using Haselgrove's equations, which is discussed in the coming section.

2.4. Propagation in an Anisotropic medium

A medium is said to be isotropic if the phase velocity of a wave propagating within it is independent of direction. This is not the case with a magnetoionic medium where the refractive index depends on direction of propagation with respect to the field. The ionosphere is non-homogeneous due to spatial variations in electron density. Collisions can be neglected so that the

refractive index can be taken as real. Due to anisotropy, the normal direction to the wave front, the wave normal (which is the phase propagation direction) will be different from the ray direction (which is the energy propagation direction) in general [18].

Figure 2.3 shows propagation in an anisotropic, homogeneous medium. (When the medium is slowly varying in space, ray theory can still be applied.) Application of the Fermat principle shows that the ray direction, the wave normal and the magnetic field direction are coplanar and that the angle between the ray-direction and wave-normal is

$$\tan\alpha = \frac{1}{\mu}\,.\frac{d\mu}{d\Theta}$$

where θ is the angle between the wave normal and the magnetic field direction.

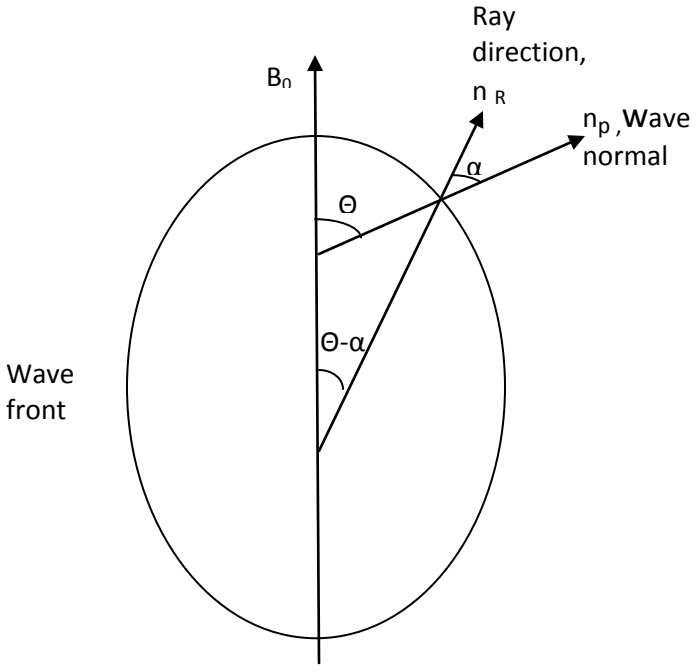

Figure 2.3: Cross-section of a wave front in an anisotropic, homogeneous medium with a plane containing the magnetic field direction [19]

We saw that the group path and phase path of a ray are different in an anisotropic medium. The ray tracing code outputs the group path which we use for further computations. A brief discussion of the common terms including group path and phase path used in the context of ray tracing is given below.

2.4.1 Phase and group path

As shown in Figure 2.3, for a wave cos (kz-ωt), the phase propagates in the direction indicated by n_p with phase velocity, $v = {}^{c}/_{\mu}$, while the energy (or a wave packet) travels in the directions of the ray n_R with group velocity, $u = {}^{c}/_{\mu' \cos \alpha}$

where μ' is the group refractive index of the rays defined by

$$\mu' = \frac{c}{\mu} = c\,\frac{dk}{d\omega} = c\,\frac{d}{d\omega}\left(\frac{2\pi}{\lambda}\right) = \mu + f\,\frac{d\mu}{df}$$

The phase velocity v, for propagation with no collisions and no magnetic field is

$$v = \frac{c}{\mu} = c\left[1 - \frac{Ne^2}{m\omega^2\varepsilon_0}\right]^{-1/2}$$

This indicates that the phase velocity in the medium is greater than the velocity of light and the wavelength in the medium is greater than in free space. [18, 19]

If the phase velocity of a wave in the medium varies as a function of the wave frequency, it is said to be dispersive. Two waves with slightly different frequencies will travel with slightly different velocities. The interference pattern between two such waves determines where and with what velocity the energy of the composite wave will travel.

For a wave, the group velocity is given by

$$u = \frac{\delta\omega}{\delta k}$$

For a non-dispersive medium in which ω/k is constant, u = v i.e. group velocity and phase velocity are the same

The distance the wave would have travelled in the time t, if it had travelled with free space velocity is called phase path.

The phase path in an anisotropic medium is

$$P = \int_l \mu \, dl = \int_r \mu \cos\alpha \; dr$$

where dl and dr are taken along n_P and n_R respectively.

Analogously the distance that the energy (of a wave packet) would have covered, if it had travelled with the free space velocity is called group path.

The corresponding group path is

$$P' = \int_r \mu' \cos\alpha \; dr$$

Till now, we have seen the basics of ionospheric propagation explained in terms of Snell's law, Appleton Hartree equations for finding the refractive index at a particular point in the ionosphere and a few terms used in ray tracing. In the next section, The Haselgrove's equations used for finding the path of a ray through the ionosphere are described.

2.4.2 Haselgrove's equations

Haselgrove (1955) introduced ray canonical equations in spherical form as shown below [19]:

$$\frac{\dot{r}}{c} = \frac{1}{\mu^2}\left[v_r - \mu\frac{\partial\mu}{\partial v_r}\right] \quad (2.5)$$

$$\frac{\dot{\theta}}{c} = \frac{1}{\mu^2 r}\left[v_\theta - \mu\frac{\partial\mu}{\partial v_\theta}\right] \quad (2.6)$$

$$\frac{\dot{\varphi}}{c} = \frac{1}{\mu^2 r\sin\theta}\left[v_\varphi - \mu\frac{\partial\mu}{\partial v_\varphi}\right] \quad (2.7)$$

$$\frac{\dot{v_r}}{c} = \frac{1}{\mu}\frac{\partial\mu}{\partial r} + v_\theta\frac{\dot{\theta}}{c} + \sin\theta\, v_\varphi\frac{\dot{\varphi}}{c} \quad (2.8)$$

$$\frac{\dot{v_\theta}}{c} = \frac{1}{r}\left[\frac{1}{\mu}\frac{\partial\mu}{\partial\theta} - v_\theta\frac{\dot{r}}{c} + r\cos\theta\, v_\varphi\frac{\dot{\varphi}}{c}\right] \quad (2.9)$$

$$\frac{\dot{v_\varphi}}{c} = \frac{1}{r\sin\theta}\left[\frac{1}{\mu}\frac{\partial\mu}{\partial\varphi} - \sin\theta\, v_\varphi\frac{\dot{r}}{c} - r\cos\theta\, v_\varphi\frac{\dot{\theta}}{c}\right] \quad (2.10)$$

where r, θ, φ are coordinates of a point in spherical system of coordinates with origin in the earth's center and c is the velocity of light in vacuum.

v_r, v_θ, v_φ are components of the wave normal direction in the r, θ, φ directions, normalized so that $v_r^2 + v_\theta^2 + v_\varphi^2 = Real\{\mu^2\}$

The above six equations, 2.5 to 2.10 can be used to find the ray path by a step by step integration process, when the value of refractive index is known. Numerical method can be used to solve the above set of equations. Solution to these differential equations gives three position variables and the three components of the direction variable of the wave normal, at any point of propagation. Here, the independent variable is 't', the time of travel of a wave front along a ray. Thus solving

the Haselgroves equations for a ray at each step along the ray path gives us the next point in its propagation path.

The group path , P' is given by the equation,

$$\frac{dP\prime}{dt} = \left(1 + \frac{f}{\mu}\frac{\partial \mu}{\partial f}\right) \qquad (2.11)$$

In the case we are considering collision, the medium is no longer lossless. Once the path is known, the attenuation suffered by the wave in travelling through the medium can be found from χ, the co-efficient of the imaginary part of the refractive index.

Let D denote the total absorption and K the absorption coefficient. In this case,

$$\frac{dD}{dt} = -(K/\mu)D \qquad (2.12)$$

The six canonical equations 2.5 to 2.10 along with the equations 2.11 and 2.12 can be integrated to get the coordinates, direction vectors, phase path and total absorption of the ray at any point along its propagation path. Instead of t, the phase path length, P, can also be used as the independent variable for integration (Haselgrove, 1955; Grossi and Langworthy, 1966) recalling that P = ct.

2.5 Jones and Stephenson's code

In 1975, R. Michael Jones and Judith J. Stephenson developed a FORTRAN program to trace rays through an anisotropic medium whose refractive index varies continuously in three dimensions. The code is a practical implementation of the equations we have seen in the previous sections of this chapter.

Given the transmitter location and the transmission details like frequency, elevation angle etc, the program integrates ray path through the ionosphere described by theoretical models. For computing refractive index, the program includes Appleton-Hartree formula, which is based on constant collision frequency. Once refractive index is known, Haselgrove's equations can be used to predict the path of the ray [20].

The program is organized into subroutines. The most important subroutine is TRACE, which is the core of the program doing the integration of Haselgrove's equations along the ray path. TRACE calls subroutine RINDEX to get the value of the refractive index. RINDEX in turn calls ELECTX, MAGY and COLZ to get parameters X, Y and Z respectively described in the refractive index formula in Equation 2.3. A simple block diagram for this is shown in Figure 2.4.

The program has several theoretical models for electron density, perturbations / irregularities in the electron density, the earth's magnetic field and electron collision frequency. The user can simulate the ionosphere using any of these models. Magnetic Field and Electron Collision frequency are not necessary if we are just considering the propagation of ordinary wave without absorption.

For refractive index (RINDEX subroutine), some of the choices available are

AHNFNC : Appleton Hartree No Field No Collision (no call made to MAGY or COLZ)

AHWFNC : Appleton Hartree With Field No Collision (no call made to COLZ)

AHWFWC: Appleton Hartree With Field With Collision

Some of the ELECTX models available are Chapman layer, Double Chapman With tilts and ripples and the most commonly used choice for MAGY is Dipole field.

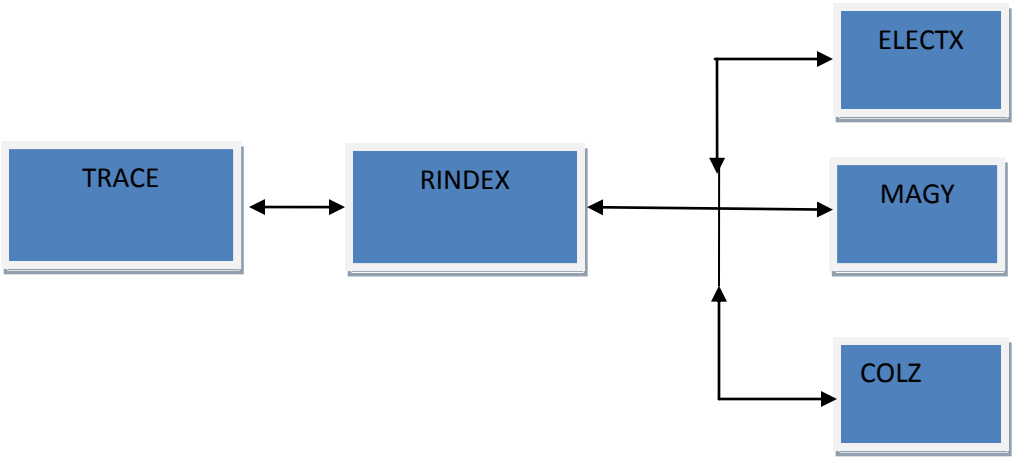

Figure 2.4: Block diagram showing the most important subroutines in the Jones Stephenson Code

Accuracy: The numerical integration subroutine has a built in mechanism to check errors and adjust the integration step length accordingly. There is provision to give accuracy as a user input parameter.

2.6 Propagation effects at HF

Figure 2.5 shows ray plots for the Blackstone radar. The ray tracing code was run with IRI-2007 as the electron density model. The simulation was run for 02 November 2009 at 18 UT. Rays of elevation angles from 5° to 35° in steps of 5° at a constant transmit frequency of 11 MHz were considered. Figure 2.5a shows the electron density profile at the Blackstone radar transmitter location. Group path is the parameter we measure using radar. So it was decided to plot the group path of a ray as a function of altitude. Figure 2.5b is the plot of group path vs. altitude which is different from Figure 2.1 which is a plot of ground range vs. altitude. The ray tracing code writes out group path of each ray at each step in the integration of the Haselgrove's

equations. A script was written to read the value of group path and altitude of each ray and to plot the same. The plot retains the same shape as that of ground range vs. altitude.

(a)

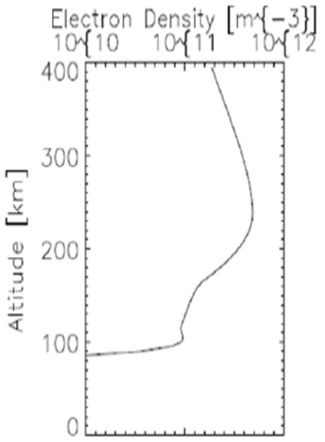

It can be seen that a bunch of rays between the higher and the lower elevation angles travel through the ionosphere with a near-horizontal path close to apogee. These rays are called Pederson rays [15]. The band of elevation angles providing Pederson rays is usually only a few degrees. In Figure 2.5, elevation angles from 10.5° to 15° are the Pederson rays. These rays reach to the greatest ranges.

(b)

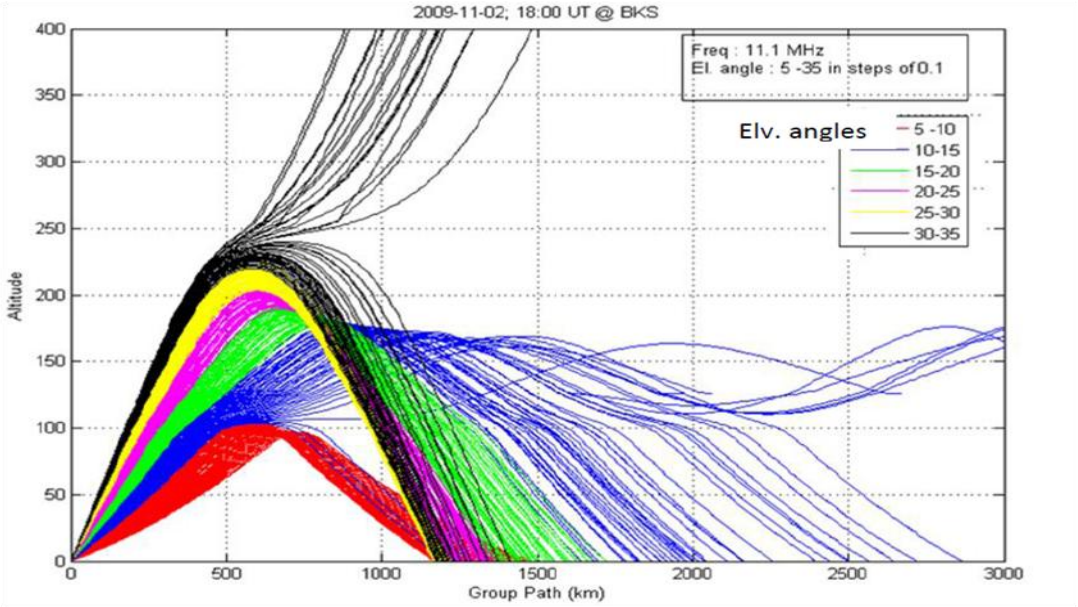

Figure 2.5: Ray plots for Blackstone radar shown to explain HF propagation effects – simulated for 02 Nov 2009 at 18:00 UT (a) Ne vs. height at transmitter location using IRI 2007 model, explained further Section 3.2. (b) Group path vs. Altitude; elevation angles are color coded with same color being used for an elevation angle band of 5°.

Skip distance is the range to the first return from the ground. From Figure 2.5b, we can see that skip distance is around 1200 km in this case. There are a large number of rays hitting this region. This is referred to as the skip distance focusing. From the figure, we can also observe that lower elevation angle rays get refracted from lower heights as compared to higher elevation angles. The higher the elevation angle, the greater is the height travelled through the ionosphere.

Signals may also be scattered by ionospheric irregularities in the D, E and F regions. The scattering may result in onward propagation (forward scatter), deviation out of the great circle (side scatter) or return along the same path (backscatter). Only a part of the signal may be scattered and the rest of the signal can propagate forward through the ionosphere.

In Figure 2.5, we can see a bunch of rays hitting the ground which is what we see as the ground scatter at the radar. The ground scatter strength is proportional to the number of rays hitting the ground. Thus from the Figure 2.5, we can see that the ground scatter power measured will show a peak at a range of ~1200 km, where there is maximum number of rays hitting the ground. Beyond 1200 km, the number density of rays generally decreases and so does the measured ground scatter signal strength, although there are variations.

Backscatter signal is measured at the radar. Backscatter is essentially the signal scattered back to the radar. Backscatter is categorized into ionospheric scatter and ground scatter depending upon whether the scattered signal reaches the radar directly from the ionosphere or it is further scattered from the ground before it reaches the radar.

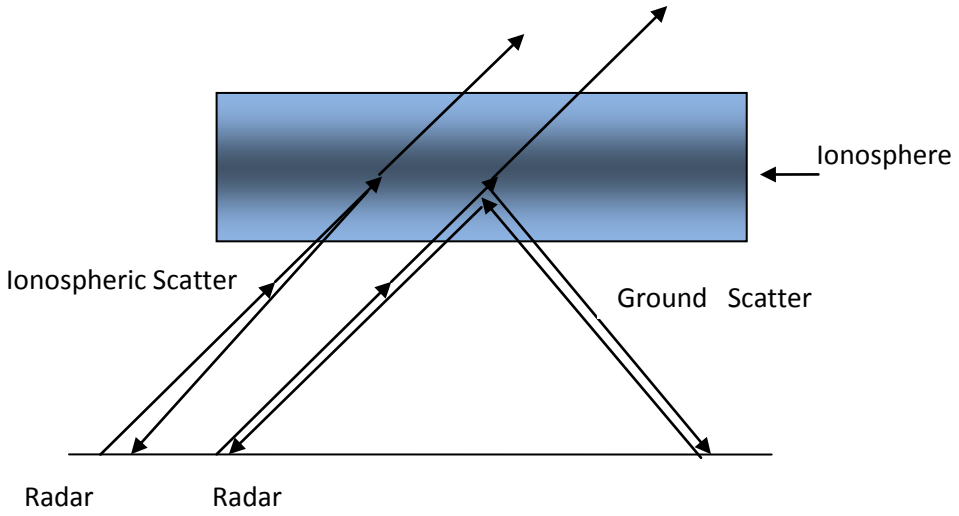

Figure2.6: Ionospheric scatter vs. Ground scatter

Figure 2.6 is a simple sketch illustrating ionospheric scatter and ground backscatter.

In the Figure 2.6., it can be seen that in the case of ground scatter, the wave reflected to the ground is again scattered back from the ground to the radar through the ionosphere where as in the case of ionospheric scatter, the wave is scattered at an ionospheric irregularity and reflected directly to the radar.

The ground backscatter varies with the variations in the ionosphere. Thus there are seasonal and diurnal variations in ground scatter. It can also change with the solar cycle. The ground backscatter is of value as a method of remote sensing the ionosphere. The ground scatter is measured by the SuperDARN radar and is what we are trying to reproduce using simulation. We can compare the simulation with the observation and assess our understanding of the ionosphere. The model parameters of the ionosphere can be fine tuned to match simulation with observation and thereby improve our understanding of the ionosphere.

Even though the main purpose of this thesis is to simulate the ground scatter pattern observed at the Blackstone radar, ray tracing can be used for another interesting application of the SuperDARN research. The main purpose of the SuperDARN radars is to study the field aligned irregularities in the F region. Orthogonality of the radar wave with the magnetic field is needed to see the field aligned irregularities. The ray tracing code gives the value of propagation vector and position coordinates at different points along the path of a ray. We can take the dot product of the propagation vector at any point along the path and the local magnetic field at that particular point, to check the orthogonality of the wave to the local magnetic field. This analysis can be used to find the frequency at which the wave is orthogonal to the magnetic field at a particular location of interest.

Chapter 3

Ray Tracing applied to the Blackstone Radar

3.1 Radar Backscatter

Backscattered HF signal from the ionosphere contains useful information regarding the state of the ionospheric medium over the propagation path of the signal. Methods of reproducing the characteristics of the backscattered signal provide an important means of remotely sensing the ionosphere. When using steerable high frequency radar, the backscatter signal can be used to infer changes in the ionosphere incurring over millions of square kilometers [21].

The observed ground backscatter depends on the radar system and the ionospheric conditions. The changes in the backscatter response are due to the changes in the ionosphere. Simulation of the backscatter power can be used for the frequency management of OTH radars.

The Blackstone radar (described in Section 1.4.2) database was selected to perform a simulation study. We aimed to reproduce the observation of the ground scatter seen with the radar, identify anomalies and explore their causes. Single hop propagation alone is considered (For further details on single hop and multihop propagation, refer to Figure 1.4). For modeling the ionosphere, Appleton Hartree with no collisions is used. IRI -2007 is used to represent electron density (the details of which are described in Section 3.2) and dipole field is used to represent magnetic field throughout the simulations.

3.2 Ray Tracing code and the IRI model

The Jones and Stephenson's code (refer to Section 2.5) was written in 1975 when the computer memory was a very expensive resource. Hence the code was designed to use minimum memory and with minimum computational complexity. Later, several versions of the ray tracing code were developed; but all were based on the basic Jones and Stephenson's code.

A modern version of the tray tracing code was obtained from Leicester University. The code had Haselgrove's equations for integrating the ray path and various theoretical models to model the ionosphere. A plot of ray tracing produced by the code is shown in Figure 3.1.

Some of the models already available in the code were:

Refractive Index	: Appleton Hartree
Electron Density	: Double Chapman layer with tilts
Magnetic Field	: Dipole, Constant, Cubic
Electron Density Perturbation	: Torus, Shock, Blob
Electron Collision	: Constant, Exponential

More details on the structure of this ray tracing code and how to run the same can be found in Appendix B.

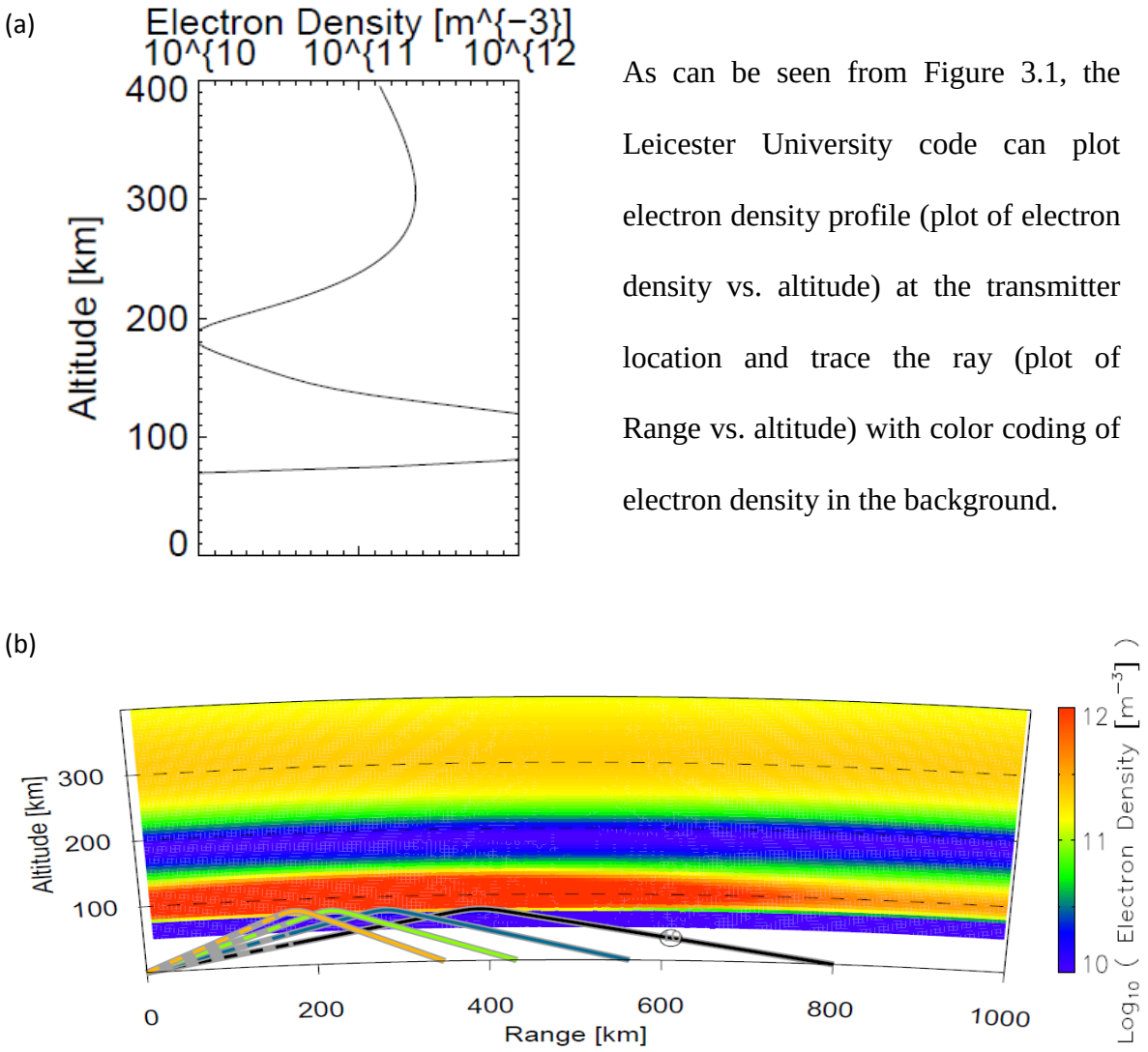

As can be seen from Figure 3.1, the Leicester University code can plot electron density profile (plot of electron density vs. altitude) at the transmitter location and trace the ray (plot of Range vs. altitude) with color coding of electron density in the background.

Figure 3.1: Plot from the existing ray tracing code (from Leicester University) ; (a) Electron density vs. altitude at transmitter location (b) Ground range vs. altitude for rays with electron density color coding in the background; simulated for elevation angles from 5° to 20° in steps of 5° at constant radar operating frequency of 10.4 MHz ; refractive index formula is Appleton Hartree with field and no collisions with Dipole magnetic field , electron density model is Double chapman layer with a blob at 100 km altitude.

Modification to the code

The International Reference Ionosphere (IRI) is a globally accepted model for the ionospheric electron density and the best empirical model available to date. The IRI-2007 model was

incorporated into the Jones and Stephenson's code for modeling the electron density. A brief description of the IRI is given below.

The International Reference Ionosphere (IRI) is an international project sponsored by the Committee on Space Research (COSPAR) and the International Union of Radio Science (URSI). These organizations formed a Working Group in the late sixties to produce an empirical standard model of the ionosphere, based on all available data sources. Several steadily improved editions of the model have been released. For given location, time and date, IRI describes the electron density, electron temperature, ion temperature, and ion composition in the altitude range from about 50 km to about 2000 km; and also the electron content. It provides monthly averages in the non-auroral ionosphere for magnetically quiet conditions. The major data sources are the worldwide network of ionosondes, the powerful incoherent scatter radars (Jicamarca, Arecibo, Millstone Hill, Malvern, St. Santin), the ISIS and Alouette topside sounders, and in situ instruments on several satellites and rockets. IRI is updated yearly during special IRI Workshops (e.g., during COSPAR general assembly) [22].

Several studies have been conducted to evaluate IRI by comparing it with other empirical models. These studies have shown that IRI is suitable for modeling the mid-,low and equatorial latitudes, and not so well suited for high latitudes where extremely dynamic processes take place and relatively little contributed to the model [23].

Figure 3.2 shows the comparison of IRI-2001 model with local empirical models at two typical mid-latitude locations – St. Santin (44.6° N, 2.2° E) and Millstone Hill (42.6° N, 71.5° W). The empirical models (values indicated by red line in the figure) were developed from long term data bases of multiple Incoherent Scatter Radars (ISRs). Comparisons were done between these ISR

models and IRI (values shown by blue dots in the figure) for median solar activity and quiet magnetic activity conditions.

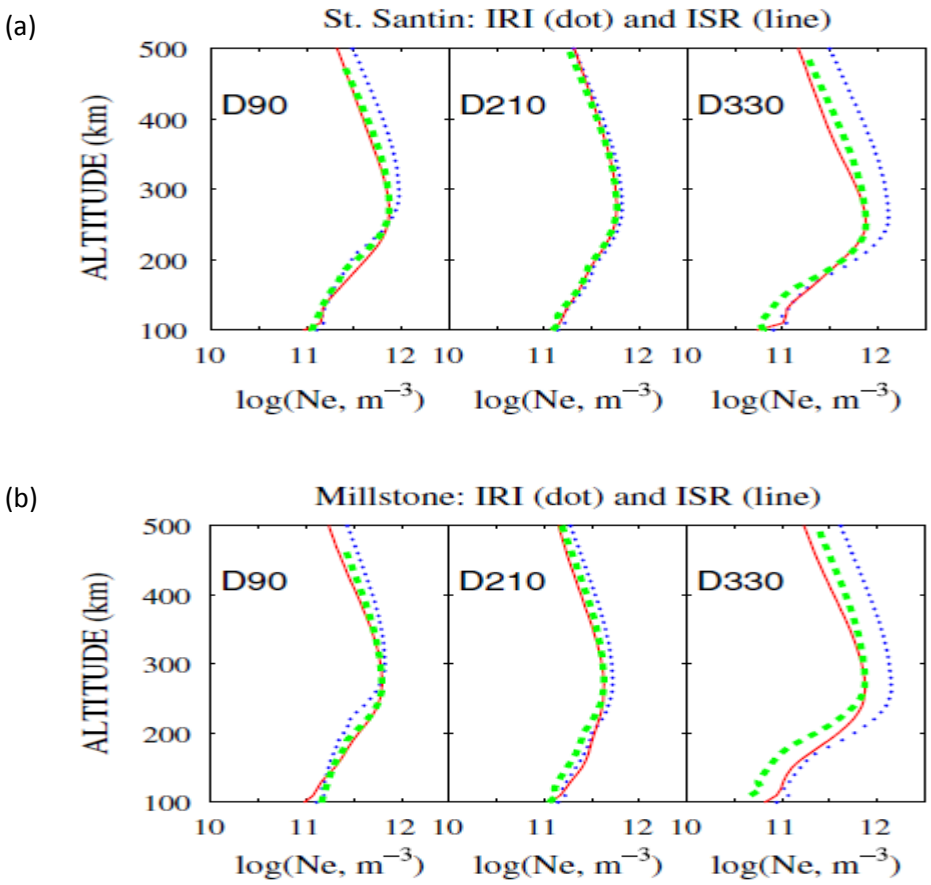

Figure 3.2: Comparison of Ne height variations between ISR (line) and IRI (blue dots) models for 2 mid-latitude locations at 12:00 LT in spring (Day number 90), summer (Day Number 210) and winter (Day Number 330). Shown also are IRI profiles scaled to the ISR model for profile shape comparisons (thick dashed green) (a) St. Santin (44.6° N, 2.2° E) (b) Millstone (42.6° N, 71.5° W) [23]

From Figure 3.2a, it can be seen that excellent agreement is achieved in summer time or around noon time in terms of the N_e magnitude amd the profile shape. In winter, the ISR N_e is lower than the IRI N_e. From Figure 3.2b, at Millstone Hill, N_e values from both models are close in summer and spring, but the ISR N_e is lower in winter.The topside (which is at altitudes above the peak

electron density value) profile shapes from both models are similar with an exception in winter. In the bottomside, ISR N_e tends to be higher than the IRI value. Thus from the comparison at two typical mid-latitude radars, it can be noted that overall there exists a very good agreement between the ISR model and the IRI model. They agree the best in summer and the worst in winter. When there exists a difference, the ISR N_e tends to be higher in the bottomside. It will be shown later in Section 4.3, that when simulations were done for the Blacstone radar location, the predictions for winter were in very good agreement with the observation ; this may be due to an improvement in IRI-2007 when compared to IRI-2001. The underestimation of IRI in bottomside electron density still persisted.

The Blackstone radar (37.1° latitude and 282° longitude) during the day is subauroral like Millstone (42.6° latitude and 288.5° longitude). It can be seen from Figure 3.2b that a reasonable agreement exists between IRI data and ISR data at Millstone Hill radar. Due to this agreement with measurement observed at Millstone and the fact that the IRI electron density model has taken data from a number of mid latitude radars like Millstone Hill, Malvern, St. Santin etc, the IRI model can be applied to model the electron density at the Blacstone radar lcoation. Also , TIGER radar (-43.4 latitude and 147.2 ° longitude), a part of the SuperDARN network in the southern hemisphere uses IRI model for their ray tracing simulations.

IRI provides electron density as a function of latitude, longitude, altitude, date and hour of the day. Figure 3.3 shows variations in electron density produced by IRI code. The latitude and longitude were taken to be that of Blackstone radar. The plots are produced by web tool provided by NASA hosted at http://omniweb.gsfc.nasa.gov/vitmo/iri_witmo.html.

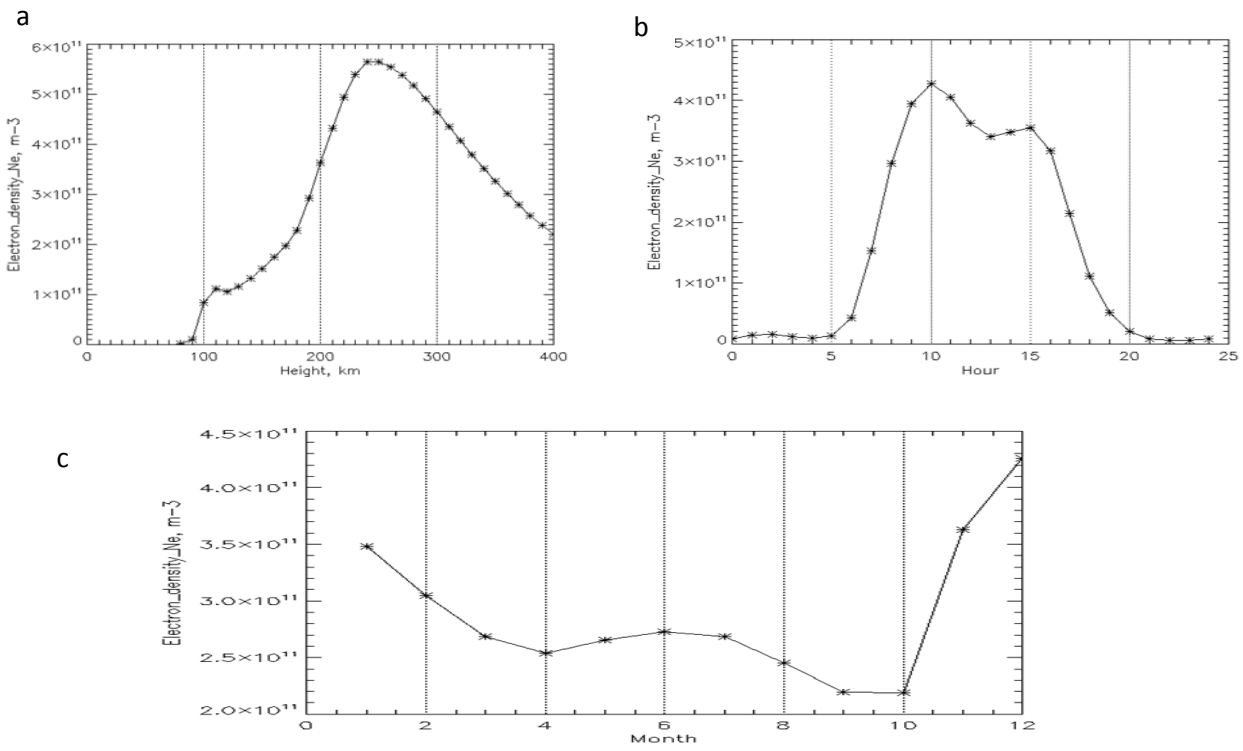

Figure 3.3: Electron density variations at the Blackstone radar location (37.1° and 282° longitude) (a) Ne vs. height on 2 Nov '09 at 12:00 LT (b) Ne vs. hour at 200 km height on 2 Nov '09 (c) Ne vs. month of the year at 200 km height at 12:00 LT [http://omniweb.gsfc.nasa.gov/vitmo/iri_witmo.html]

In each case where electron density is plotted as a function of a parameter, the other parameters were kept constant. In Figure 3.3a, it can be seen that the N_e value peaks at an altitude between 200 and 300 km. From Figure 3.3b, it can be noted that the electron density undergoes diurnal variations. The buildup of the ionosphere in the morning and it's depletion in the evening can be seen from the plot. This is the reason why we see ground scatter at Blackstone radar only during day time. At night, there is no strong ionosphere to refract the rays and hence there is no ground scatter power measured at night in typical days. Figure 3.3c shows the profile of electron density as a function of month of the year. It is counter-intuitive to see higher electron density in the winter months (October to February) than during the rest of the year. This phenomenon is referred to as the winter anomaly and is further explained in Section 4.2.

Now we have seen how IRI serves to be a suitable model for the electron density at Blackstone radar location. In the next section, details of incorporating the latest model of IRI available, the IRI -2007 model to the existing ray tracing code are discussed.

3.3 Integrating the IRI -2007 model into the Ray Tracing code

The available ray tracing code and the IRI–2007 code are written in FORTRAN. In Figure 2.4, we saw how the Jones and Stephenson's code calls electron density model subroutine to get the parameter 'X' in the Appleton- Hartree equation. It was decide to add a call to the IRI code as a part of the 'ELECTX' subroutine. When the user defines 'IRI' as the electron density model, the ray tracing code calls IRI code with input parameters altitude, latitude and longitude at each step of integration in the ray path to get the corresponding electron density at that point.

Integrating the IRI-2007 model into the ray tracing code was not easy. The ray tracing code is written in FORTRAN and has extensive use of common blocks instead of function calls. Common blocks are a way of sharing variables between subroutines. When variables are declared in common blocks, any subroutine calling this common block can access those variables. Changes to these common block variables were made in a number of different places making the code very hard to understand. Hence the code was first converted to C using the 'f2c' converter and later given to the tool 'Doxygen'. Doxygen generates the function call graph and function caller graph for the code showing subroutine calls which was of great help in understanding the code. An example of these two graphs is given in Appendix C.

When IRI-2007 code was first integrated into the ray tracing code, there were many issues due to variable type mismatch. FORTRAN code crashed several time after entering into infinite loop

without giving relevant error messages. When the number of points in the ray path were large (as in the case of Pederson rays described in Section 2.6), the code used to crash. It took hours of debugging to realize that the array overflow was the reason behind this. When simulations were run for the year 2006, the code worked well, but it again crashed for a simulation attempted for the year 2009. This was because of the changing solar activity and the corresponding increase in the electron density values. The array sizes declared in ray tracing code were not large enough to store these higher values of electron densities. Array sizes were modified to overcome this issue.

The stringent printing formats in FORTRAN including the restriction on number of characters per line also created lot of confusion while coding.

After elaborate debugging and running of the code, a few sanity checks were done to ensure the correctness of the code. The electron density obtained from the IRI web page and the values output by the ray tracing code were compared and the comparison plot is shown in Figure 3.4. Both use electron density values from the same database. As expected, the plots are identical.

Figure 3.4 compares electron density for November 2009 at 18:00 UT at the Blackstone radar location. The electron density peaks at 250 km which is the F region and there is no E region as is expected in winter.

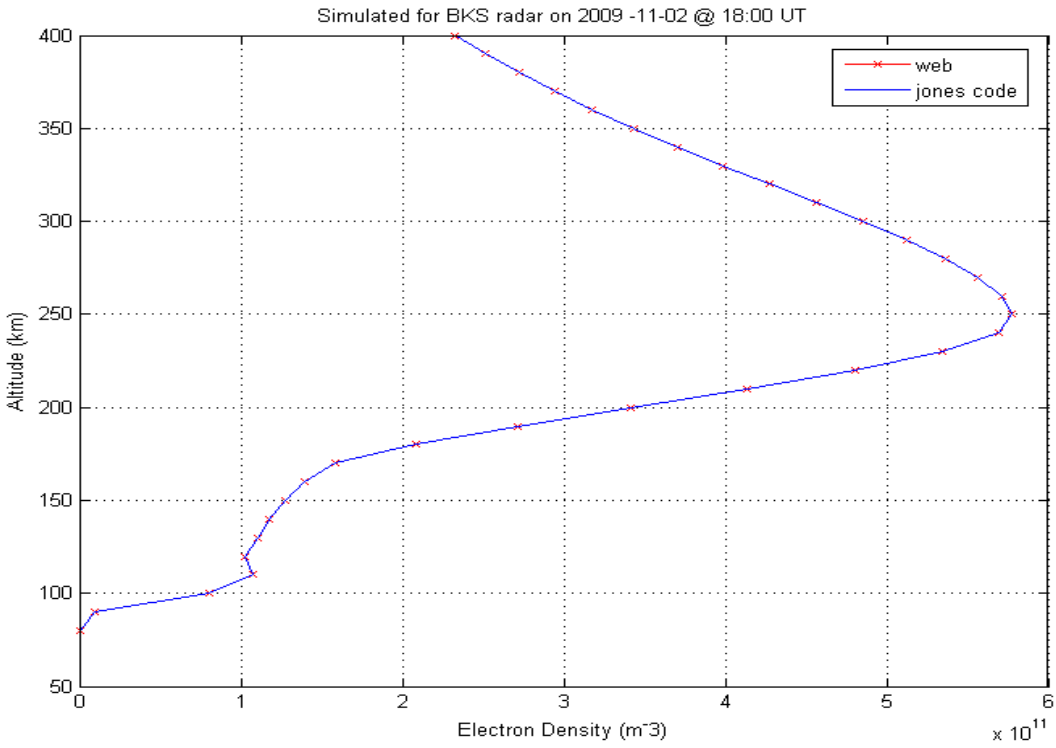

Figure 3.4: Comparison of electron density profile, obtained from Ray Tracing (Jones & Stephenson's code) and the web tool for IRI provided by NASA, done as a part of sanity check

The diurnal variations and seasonal variations in the ray paths were checked. Figure 3.5 shows the same. For modeling the ionosphere, Appleton Hartree with no collisions is used. IRI-2007 is used to represent the electron density model and dipole field is used to represent the magnetic field throughout the simulations.

Simulations were done for the location of the Blackstone radar for both the winter and summer solstice. Year was chosen randomly. 11 MHZ is the typical frequency for Blackstone radar operation. Figure 3.5a shows simulation done for winter solstice (21 Dec 2006) at 12 LT and Figure 3.5b shows simulations done for the same day at 23 LT.

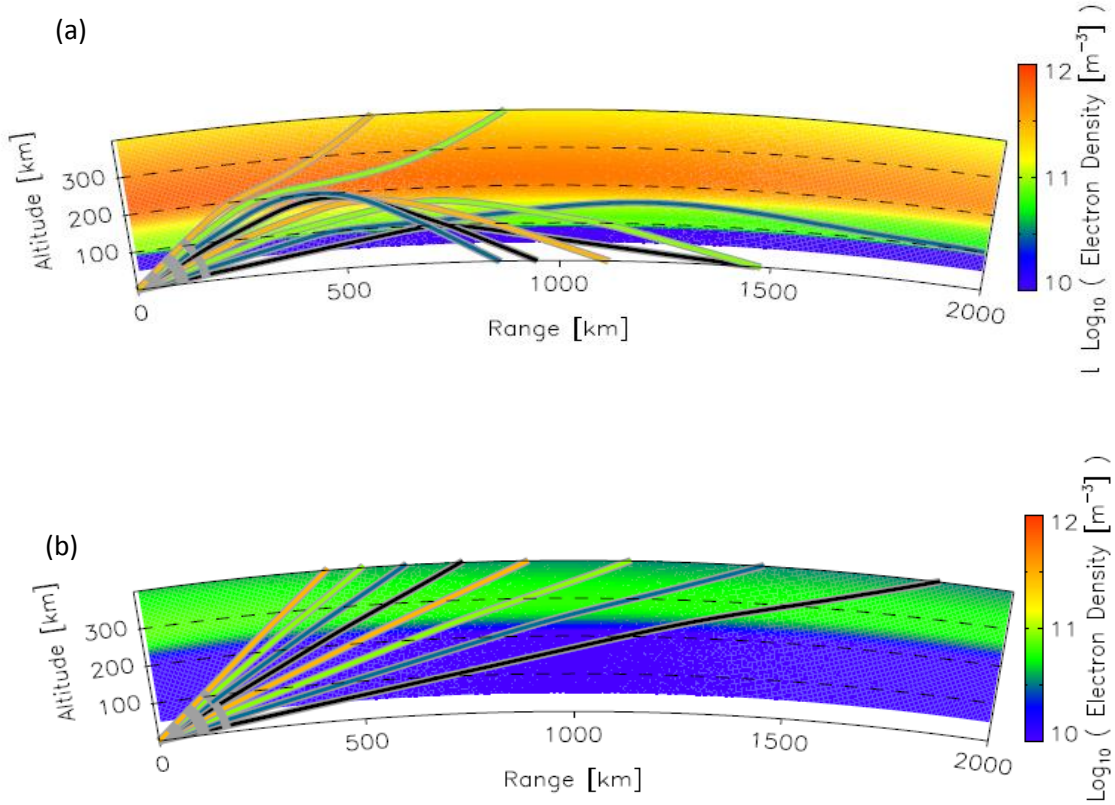

Figure 3.5: Simulation done for rays of elevation angle from 5° to 40° in steps of 5°; rays of different elevation angles are indicated by different colors ; background electron density is also color coded.(a)Winter day – Simulated for 2006-12-21 ; 12 LT at 11 MHz (b) Winter night - Simulated for 2006-12-21; 23 LT at 11 MHz

The diurnal variations in the ionosphere electron density can be seen clearly from Figures 3.5a and b. In Figure 3.5a, as we move along the altitude we can see that the electron density peaks between 200 km and 300 km. This corresponds to the F region. There is no strong E region formation in winter. From Figure 3.5a, we can see that the higher elevation angle rays get refracted from a greater height. The skip distance focusing can be seen in Figure 3.5a around 1000 km. Skip distance focusing will be more clear in the ray tracing plot when we use finer steps in elevation angle. The rays at skip distance focusing are refracted from the F region as there is no strong E region to refract the rays. The rays hitting the ground at a distance are

scattered back to the radar and are responsible for the observed ground backscatter power at the radar. The more the number of rays hitting a region, the higher is the power measured at that point. All rays escape at night as there is no strong ionosphere to reflect them back to the ground (Refer Figure 3.5b).

Figure 3.5c and d shows simulations done for summer solstice (21 June) in 2006.

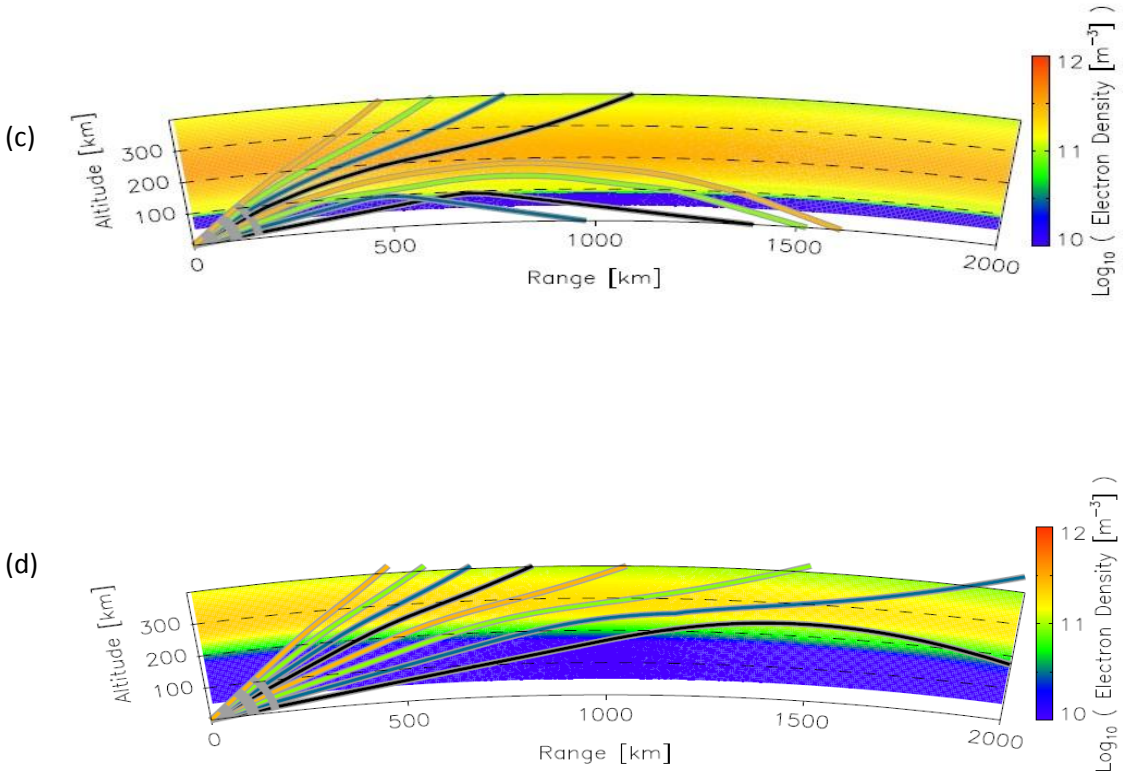

Figure 3.5: Simulation done for rays of elevation angle from 5° to 40° in steps of 5°; rays of different elevation angles are indicated by different colors ; background electron density is also color coded.(c)Summer day - Simulated for 2006-06-21; 12 LT at 11 MHz (d) Summer Night - Simulated for 2006-06-21; 23 LT at 11 MHz

From Figure 3.5c, it can be noted that there is a strong E region and F region during day time of summer. The lower elevation angles are refracted by the E region and they hit the ground at a

ground range less than 1000 km. We can see the higher elevation angle rays getting refracted from the F region. They strike the ground at greater ranges, ~1500 km in Figure 3.5c. The night time ionosphere is shown in Figure 3.5d and it is too weak to refract any rays to the ground. Thus from Figure 3.5, it can be inferred that the ground backscatter occur mainly during the day time in both summer and winter as the night time ionosphere is too weak to refract rays back to the Earth in both these seasons.

The observed power is primarily in a band of group paths (or ground ranges), which means there are no rays hitting the ground till a certain distance from the radar. The scatter power observed peaks at the skip distance and then gradually diminishes as we move along the group path (In Figure 3.5a, this skip distance is approximately 800 km). The set of near group paths where there is more intense ground scatter is referred to as the ground scatter band.

In Figure 3.5, it can be observed that the day time electron density in F region is higher in winter than in summer. This phenomenon is referred to as winter anomaly as is explained further in Section 4.2. Hence during winter, there will be more backscattered power measured due to two reasons: A weaker E region in winter allows more rays to go to the F region and the stronger F region refracts more rays back to the ground.

Now that we have seen how the ray tracing plot can be an indication of the measured ground scatter signal, we will take a look at the actual radar time plot of ground scatter observed at Blackstone.

Figure 3.6 shows the time series plot of ground scatter data from Blackstone. The plot shows time in UT. Local time, LT = UT -5 for the Blackstone radar location

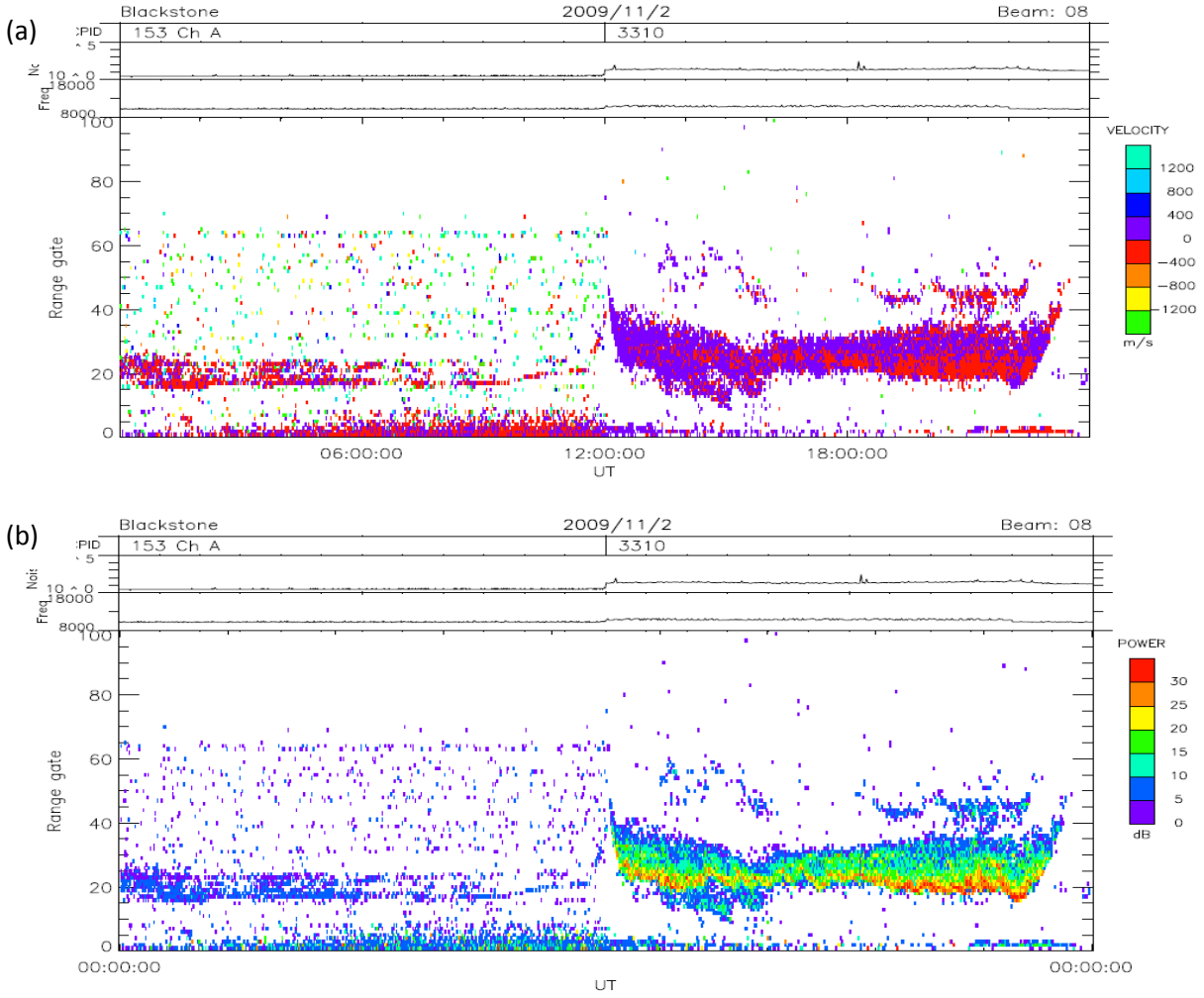

Figure 3.6: Time series plot of radar power measured at Blackstone on 2 Nov '09 (data from 00 UT to 00 UT of next day) shown as a function of range gate (same as group path). (a) velocity plot. Zero Doppler velocity implies ground backscatter (b) corresponding power plot. In this plot, the ground scatter band is from range gate 22-35. Skip distance focusing can be seen near range gate 22

In Figure 1.6, the Doppler velocity plot from 16 beams of SuperDARN radar was introduced. There was not much variation across the beams in the ground scatter signal received. Hence in our simulations, we will be using data from a single beam. Here in Figure 3.6, the data from Beam 8 which has an azimuth angle of 335° is used. Figure 3.6 shows radar backscatter power as

a function of range gate and time. The concept of range gate is explained in the next section, 'Group path and range gate'.

In Figure 3.6a, Doppler velocity measured at the radar is shown. Red or violet color indicates near-zero velocity which corresponds to the ground scatter. Figure 3.6b gives the power in dB of the ground scatter measured. From the figure, it can be noted that the ground backscatter appears predominantly during the day time. During day time, there is no scatter power measured till range gate 22. The scatter power peaks at range gate 22. This corresponds to the skip distance focusing shown in Figure 3.5. Also, there is a band of near range gates over which more intense backscattered power is measured. This ground scatter band is gate 22 to 35 in Figure 3.6.

Group path and range gate:

The sketch in Figure 3.7 shows the difference between ground range and group path.

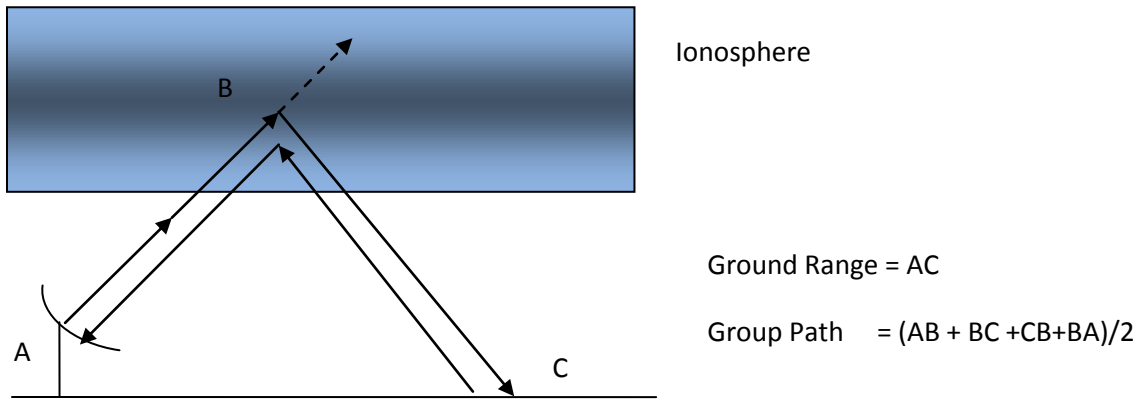

Figure 3.7: Group path and ground range - Neglecting the height of the radar antenna, point A can be taken as the source of the ray. Ray gets reflected from ionosphere at B and hits ground at C. From C, it is scattered and reaches A through B.

In Figure 3.7 ground range is the distance measured over ground from A to C where as slant range (group path) is the total distance traversed by the ray from A to C through B, i.e. the distance corresponding to the time taken for propagation divided by 2.

Ray tracing code writes out the values of group path (also known as slant range or group range), ground range and altitude at each step of ray path integration. Range gate can be considered as receivers placed along the group path of the radar beam. First range gate starts at 180 km from the radar and each range gate is of length 45 km. Hence signals from group path interval 180 to 225 km (=180+45) are measured in range gate 1, 225 to 270 km in range gate 2 and so on.

Group path = 180 + (45 * range gate number)

It was decided to run the simulations for specific days for the Blackstone radar. The idea was to simulate and compare with radar data, the pattern of ground backscatter observed, the diurnal and seasonal evolutions it undergoes and try to explain any anomalies observed.

From the radar power plots, it was observed that the measured power remains almost the same through an hour. Hence it was decided to run ray tracing for each hour of a particular day. The year 2009 was selected to study the ground scatter pattern.

The following assumptions were made while choosing days for simulation:

- Magnetically quiescent days were chosen for simulation (Magnetic Kp index ≤ 2) as IRI cannot capture the dynamics of geomagnetic disturbances.

- Elevation angles from 5°-35° were chosen. (When simulated, it was observed that only elevation angles below 35° hit the ground. Also when elevation step of 0.1 was chosen,

resulting power histogram plot was observed to have the best match with the observation)

- Rays at all elevation angles were assumed to be of equal power. Using the antenna analysis done in the SuperDARN lab [24], it was noted that there is no major power variation among rays in the range of our simulation.

- Electron density was assumed to be constant throughout an hour. This assumption can be justified by the fact that there is no major change in radar data observed through an hour.

- Constant radar cross-section for ground scattering.

Some of these assumptions could be relaxed in a more refined analysis.

A brief discussion of deriving backscatter power plots from the ray tracing simulation is given in the following section. The radar data for 02 November 2009 and the corresponding simulation are selected for our discussion.

3.4 Estimation of the ground scatter power from ray tracing

The ray tracing code was run for Blackstone radar for 02 Nov 2009; 18:00 UT and a frequency of 11 MHz.

From the values written out by the ray tracing code, the plot of group path versus altitude was plotted and is shown here in Figure 3.8. This figure is the same as explained in Figure 2.5.

(a)

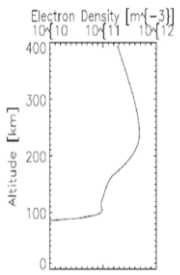

(b)

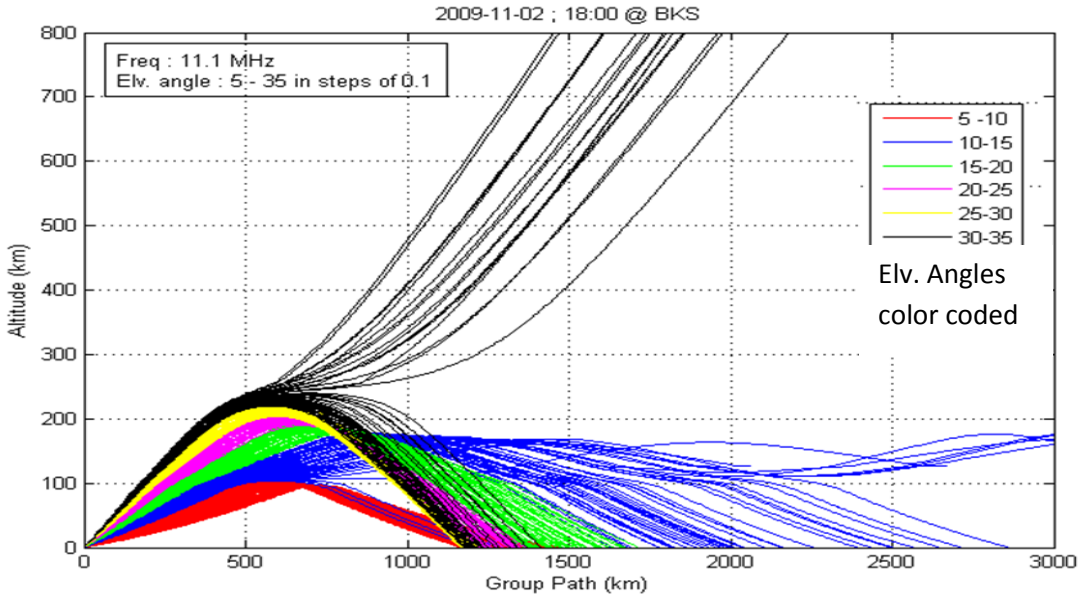

Figure 3.8: Ray tracing plots for 02 Nov 2009 at 18:00 UT (a)Ne vs. height at the Blackstone radar location using IRI 2007 model (b) Group path vs. Altitude ; Simulations done for rays with elevation angle from 5° to 35° in steps of 0.1° and are color coded, rays falling in an elevation band within 5° are colored the same i.e. red represents rays from 5° to 10°, blue from 10° to 15° and so on

Figure 3.8 clearly shows the skip distance focusing. The first bunch of rays (elevation angles from 5-10°) hit the ground only after 1000 km. From the plot of altitude vs. group path, a histogram of ray density was produced and is shown in Figure 3.9. The x- axis is changed from group path to range gate as this is the common terminology used in radar data analysis.

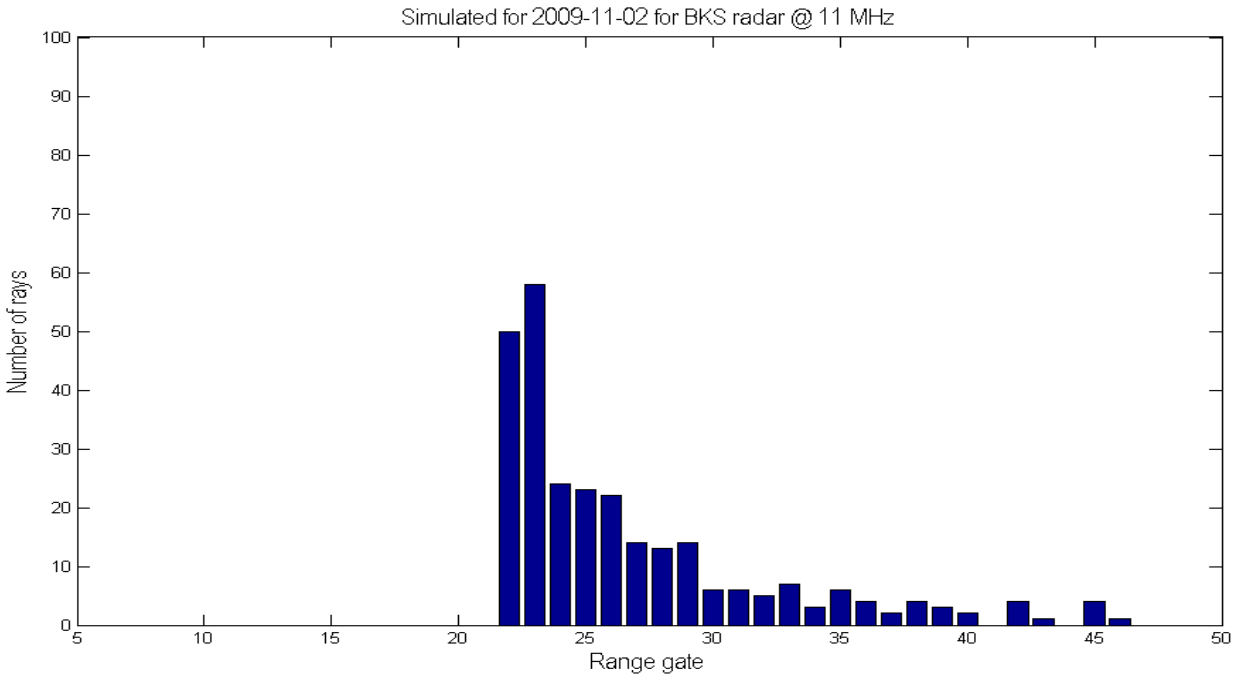

Figure 3.9: Ray Density Histogram obtained for group path data shown in Figure 3.8. The focusing of rays at group path of 1170 km as seen in Figure 3.8b is the reason for the first spike in histogram at range gate 22

In Figure 3.9 we can see that there is no ray hitting the ground before range gate 22. Range gate 22 corresponds to a group path of 180 + 22 * 45 = 1170 km. This can be seen in Figure 3.8b as the region where the first bunch of rays hitting the ground concentrate. So the first spike in ray density histogram comes at range gate 22 and in 23. This is the skip distance focusing. As we move further along the range gates, the number of rays decreases gradually and then vanishes which is identical to the case shown in Figure 3.8b, where the concentration of rays hitting the ground decreases beyond group path of ~ 1500 km. In Figure 3.9, range gate 22 to 40 can be taken as the ground scatter band.

The more the number of rays focusing in a range gate, the higher the power measured in that particular range gate. From the ray density histogram, a power histogram can be generated as

shown in Figure 3.10. The power plots from the radar are in dB scale. Hence power in a particular range gate is taken to be the logarithm of N, where N is the ray density in that gate.

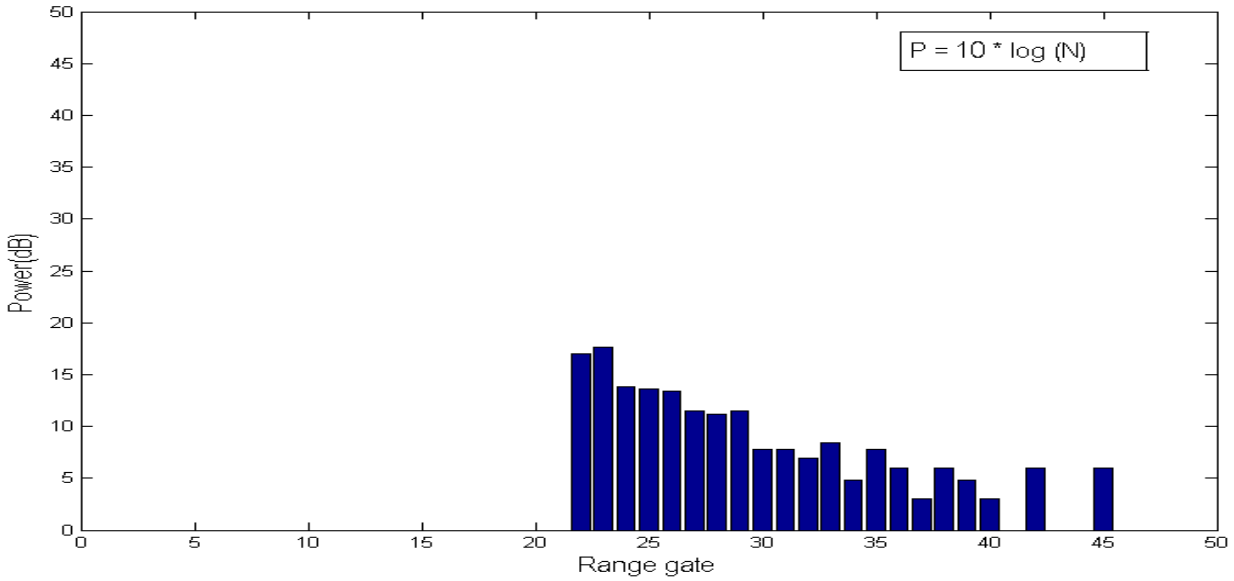

Figure 3.10: Histogram expressed in terms of power. The more the number of the rays hitting at a range gate, the more the measured power at that particular range gate. Since radar power measurements are in dB scale, logarithm of N is chosen to represent power; N being the number of rays striking at the range gate

The power plot in Figure 3.10 was changed into a Range Time Intensity (RTI) plot format shown in Figure 3.11 as this is the standard form of plot available for radar data. The radar time series plot shows the echo (scatter) power measured in dB at each range gate as a function of time. The power values are color coded.

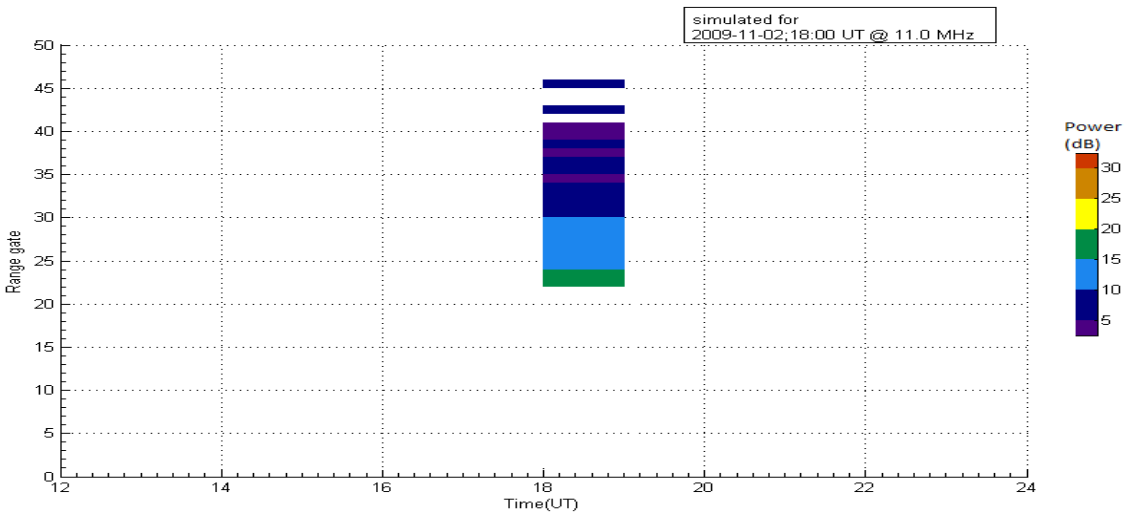

Figure 3.11: Power plot for 02 Nov 2009; 18: 00 UT. The power values are color coded and plotted against the time for which simulation was run. This is the standard format for radar power data

From Figure 3.11, it can be seen that there is no power till range gate 22 at 18 UT. The peak value of ground scatter power is at range gate 22 and 23 (indicated by the green color). Beyond range gate 22 the scatter power gradually decreases and vanishes completely beyond range gate 45. This is identical to Figure 3.10. Simulations were run for whole day (from 12:00 – 23:00 UT) and were plotted as shown in Figure 3.12.

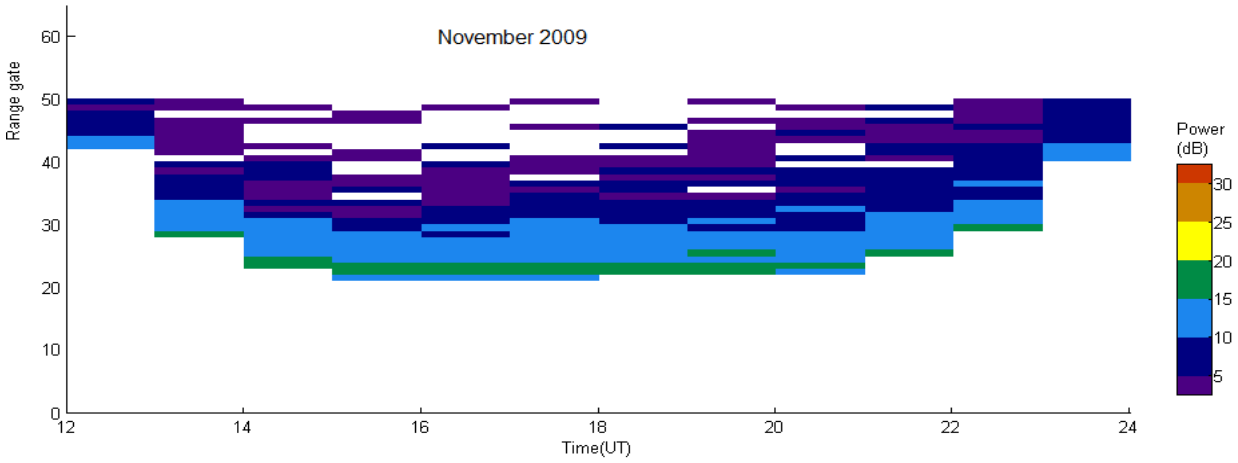

Figure 3.12: Simulated for 02 Nov 2009 from 12:00 – 23:00 UT. This corresponds to day time hours in Blackstone, when we see ground scatter

From Figure 3.12, it can be noted that at 12:00 UT which is 7:00 LT, the ionosphere builds up slowly with sunrise and there is some power in the range gates 40 to 50. This is because when the ionosphere is weak, rays traverse greater heights before getting reflected. From 12:00 to 14:00 UT, we can see the slow build up of the ionosphere where the first range in which power is measured is getting closer to the radar. Also the measured power increases. From 14:00 UT to 21:00 UT (which corresponds to 9:00 LT to 16:00 LT), the skip band and the power measured remains nearly constant. From 21:00 UT to 23:00 UT, the ionosphere depletes and a corresponding decrease in power and shift in skip band range gates occur.

Radar Data Processing: The radar data available is in the form shown in Figure 3.13.

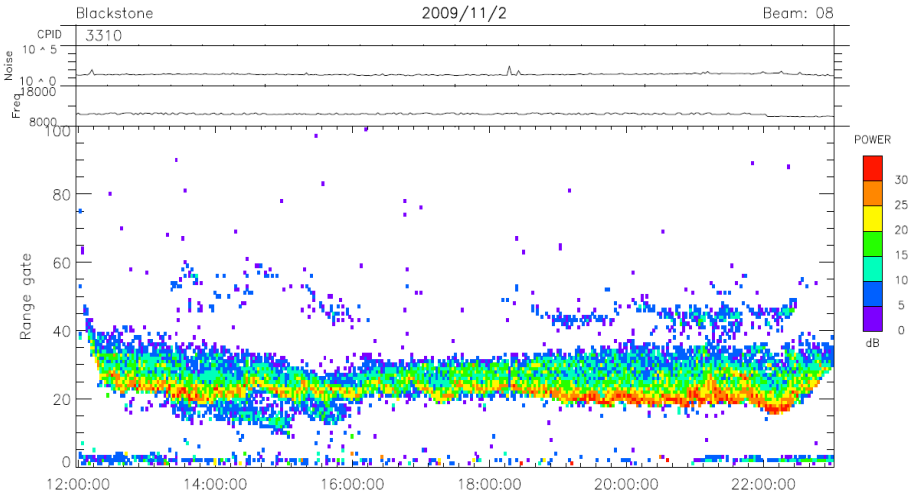

Figure 3.13: Time series plot from radar measurements; same as shown in Figure 3.6b, but time axis is from 12 to 24 UT when ground scatter is observed

Since simulations were run for a particular hour, it was decided to plot the median value of power for a particular hour. This is for the ease of comparison with simulation. The median value of measured power, at a particular range gate, for a particular hour was computed. This

median power is plotted against each range gate as a color-coded time series graph shown in Figure 3.14. Now the plot of Figure 3.14 can be compare directly with Figure 3.12.

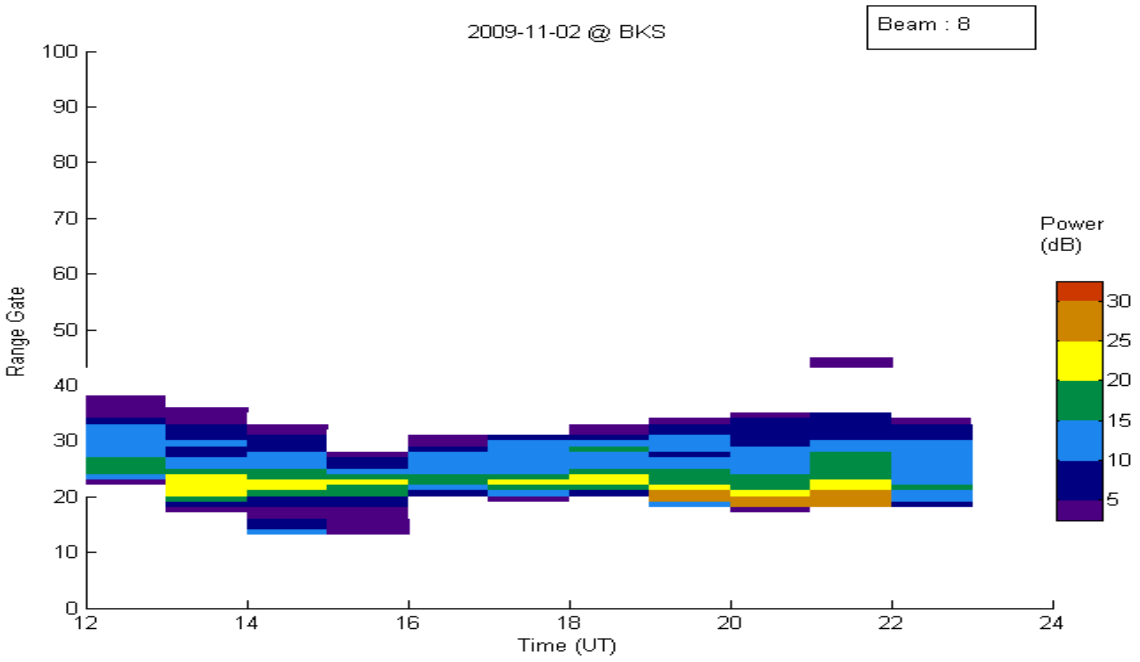

Figure 3.14: Time series plot of median power per hour (derived from Fig 3.13)

It can be noted that the Figure 3.14 retains the main features of Figure 3.13. The skip distance focusing is at range gate 22 and there is some enhancement in power at range gate 22 from 19 to 22 UT.

Note that no effort has been made to normalize the power in the simulation plot according to the observed backscatter power; but the peak power levels are fairly close with the default. For the purpose of this analysis, it is sufficient that zero-order agreement is obtained in terms of distribution of the ground scatter band in range, time and basic power variation (skip distance focusing). The scripts used for plotting histograms, Range Time Intensity (RTI) plots are given in Appendix D.

In the figure below, the radar data plot in Figure 3.14 and simulation plot in Figure 3.12 are shown side by side for ease of comparison.

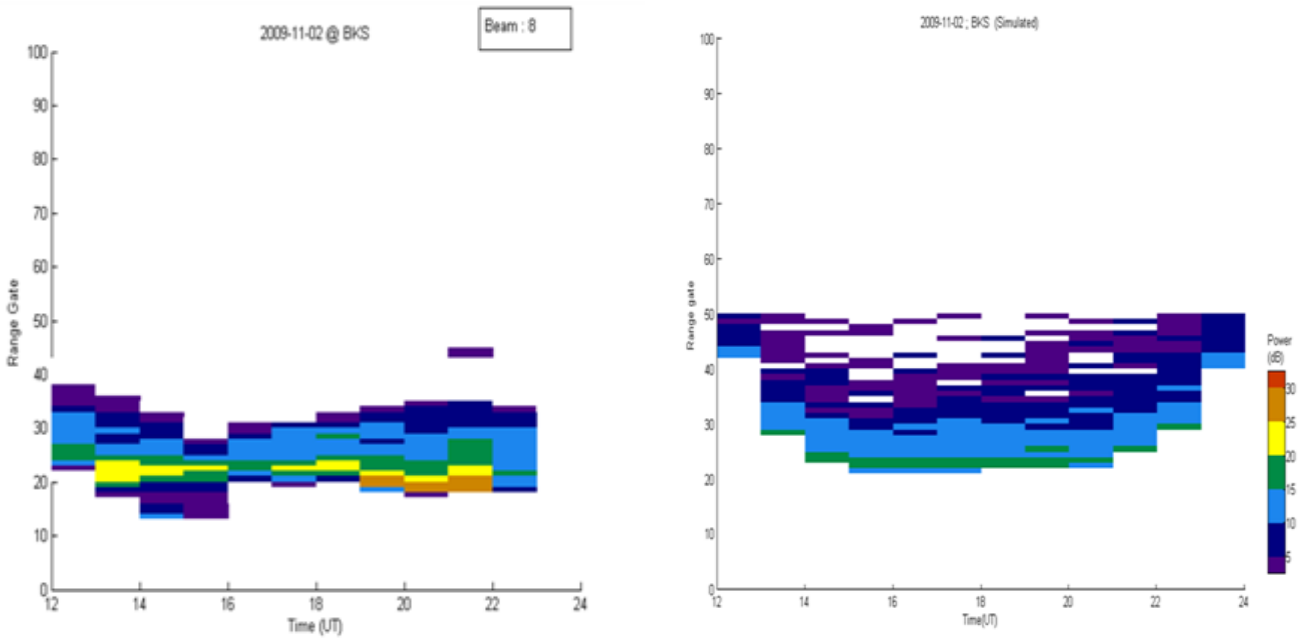

Figure 3.14 (radar data plot) and Figure 3.12 (simulation plot) shown side by side (as a and b respectively) for ease of comparison

We can see that, both in the simulation and the actual observation, the peak power occurs around range 22. In the case of radar data, the skip band extends only to range gate 40 where as in simulation, it is up to range gate 50. Applying a 5 dB threshold to the simulation result, the skip zone is approximately from range gate 22 to 35 in both cases.

In the simulation, the maximum power range gate is 22 and power remains almost the same throughout the day from 14:00 to 22:00 UT. In radar data, the maximum power range gate is 22 from 13:00 to 23:00 UT, but there is an enhancement in power at gate 22 from 19:00 to 22:00 UT. Also there is some power in range gates before the maximum power range gate in the case

of radar data, whereas in simulation, the skip distance focusing is more distinct. Simulation shows slow build up and depletion of ionosphere from 12:00 to 15:00 UT and 21:00 to 24:00 UT respectively, where as in radar data, the build up and depletion is quite sharp.

Although IRI could not predict these subtle ionospheric dynamics, there is a very good match between simulation and data as far as skip zone is concerned. Because of this promising result observed in the simulation, it was decided to go ahead and simulate for typical days in each month of 2009. These results are shown in Chapter 4.

Chapter 4

Simulation and Analysis of the Ground Scatter Power, Year 2009

Accurate modeling of the pattern of evolution of ground scatter through the seasons helps us to understand the changes the ionosphere goes through. This chapter details the pattern of ground scatter evolution through the year 2009 at the Blackstone radar. The seasonal variations and the anomalous features observed in the ground scatter power are discussed. Simulations were run in an attempt to reproduce these features and hence assess our understanding of the ionosphere in and around the Blackstone radar location.

Days in each month of the year 2009 (except February and November) were selected so that they represent an average picture of the ground scatter observed during that particular month. There was not enough radar data to find typical days in February and November. Geomagnetically quiet days were considered. The radar plots of the ground scatter as a function of range gate and time for these days are shown in Figure 4.1 to Figure 4.3. The plots are representative of the typical days of each particular month. The plots extend from 12 to 24 UT (8 to 20 LT) as this is the typical time interval during which the ground scatter is observed at Blackstone, i.e., ground scatter is typically observed only during the hours of daylight. The radar operated at an average frequency of 11 MHz on all these days. The data from a central beam of the radar, beam 8, is used for this analysis.

4.1 Seasonal Variation of the Ground Scatter observed at Blackstone

Figure 4.1 is the plot of radar data for selected days from January to May. From Figure 4.1a, we can see that the ground scatter in January starts at 14 UT and persists till 22 UT and is concentrated in the range gate interval 20 to 40. It can be seen that the range gate where the maximum power is observed oscillates in range as we progress through the day. This is due to the presence of gravity waves, which serve to focus and defocus the backscatter returns. The pattern of ground scatter is similar in March (Figure 4.1b), except that the day is longer and hence the duration of the ground backscatter observed is also longer. There is an enhancement of power in the range gates close to 20, from 22 to 24 UT, and an equatorward displacement of the skip distance. This early evening effect is likely due to enhanced F region densities or changes in layer height.

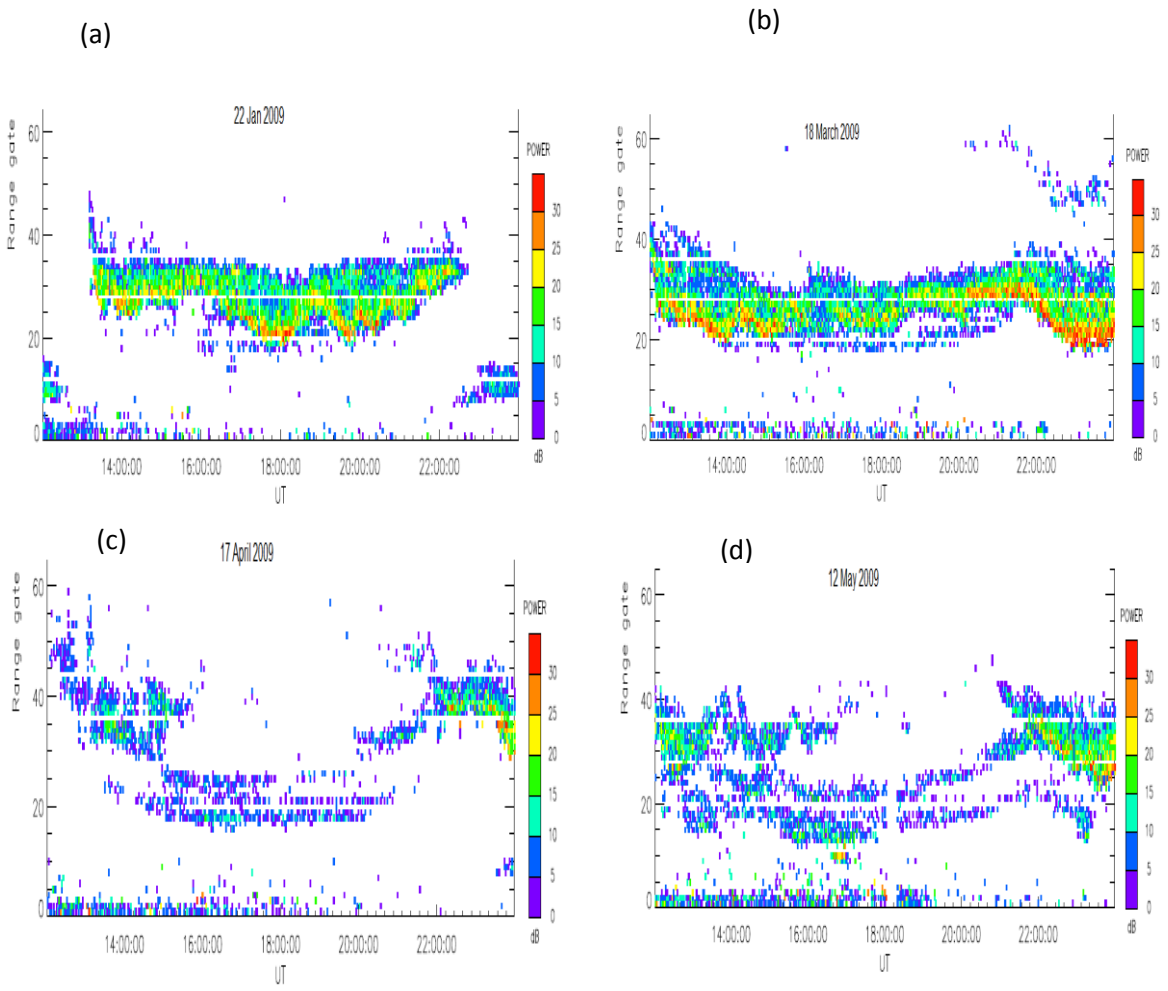

Figure 4.1: Radar range – time plot showing the ground backscatter power as a function of time and range gate (a) Jan (b) Mar (c) April (d) May. The plots show data from Beam 8 with the radar running at an average frequency of 11 MHz. Sunset hours in UT are 22:24 (Jan), 23:21 (Mar), 23:48 (Apr), 00:10 (May) [www.sunrisesunset.com /usa/Virginia.asp]

In April, the backscatter power is concentrated in range gates 30 to 40 during the morning time from 12 to 15 UT and during dusk from 21 to 24 UT. From 15 to 21 UT, the band of maximum power measured is from range gate 18 to 27.Here, backscatter occurs primarily from two narrow bands. (Signals scattered from the E region hit the ground at shorter group range than those scattered from the F region. This was discussed in Section 3.3.) Thus the power from E region is measured at nearer range gates than that from the F region. The further band, from gates 20 to

25, is seen to be contiguous with the F region scatter near dawn and dusk, and, the nearer band which is from gates 18 to 20, is due to scatter from the E region. When the E region is absent during early morning and late evening, the backscattered signal comes from a broader range interval corresponding to the F region. In May, the features of the backscatter power are quite similar to those observed in April. An evening enhancement (from 22 to 24 UT) in the F region ground backscatter power is observed in April and May. The evening enhancement observed in March continues in April and May.

Figure 4.2 shows radar plots from June to August. In Figure 4.2a, it can be seen that in June, significant ground scatter is limited to range gates less than 20 almost throughout the day except from 21 to 23 UT where there is a little power enhancement in range gates 30 to 40. At night time there is strong back scatter observed in range gates 5 to 15 which could be from a night time auroral E region. In July, there are 2 bands of backscatter power from 12 to ~18 UT measured in range gates 5 to 10 and 12 to 20 corresponding to backscatter from E and F regions of the ionosphere, respectively. After 18 UT, it can be noted that there is no lower band of power and the upper band moves to farther range gates as the day progresses. This indicates vanishing of the E region and a slowly depleting F region. In August, there is consistent power measurement in the gates 15 to 20 from 12 to 23 UT and some power enhancement in range gates 25 to 40 from 12 to 14 UT and later from 22 to 24 UT. Thus we can see the presence of a very dynamic E region in the months of June to August, which blankets the rays from reaching the F region.

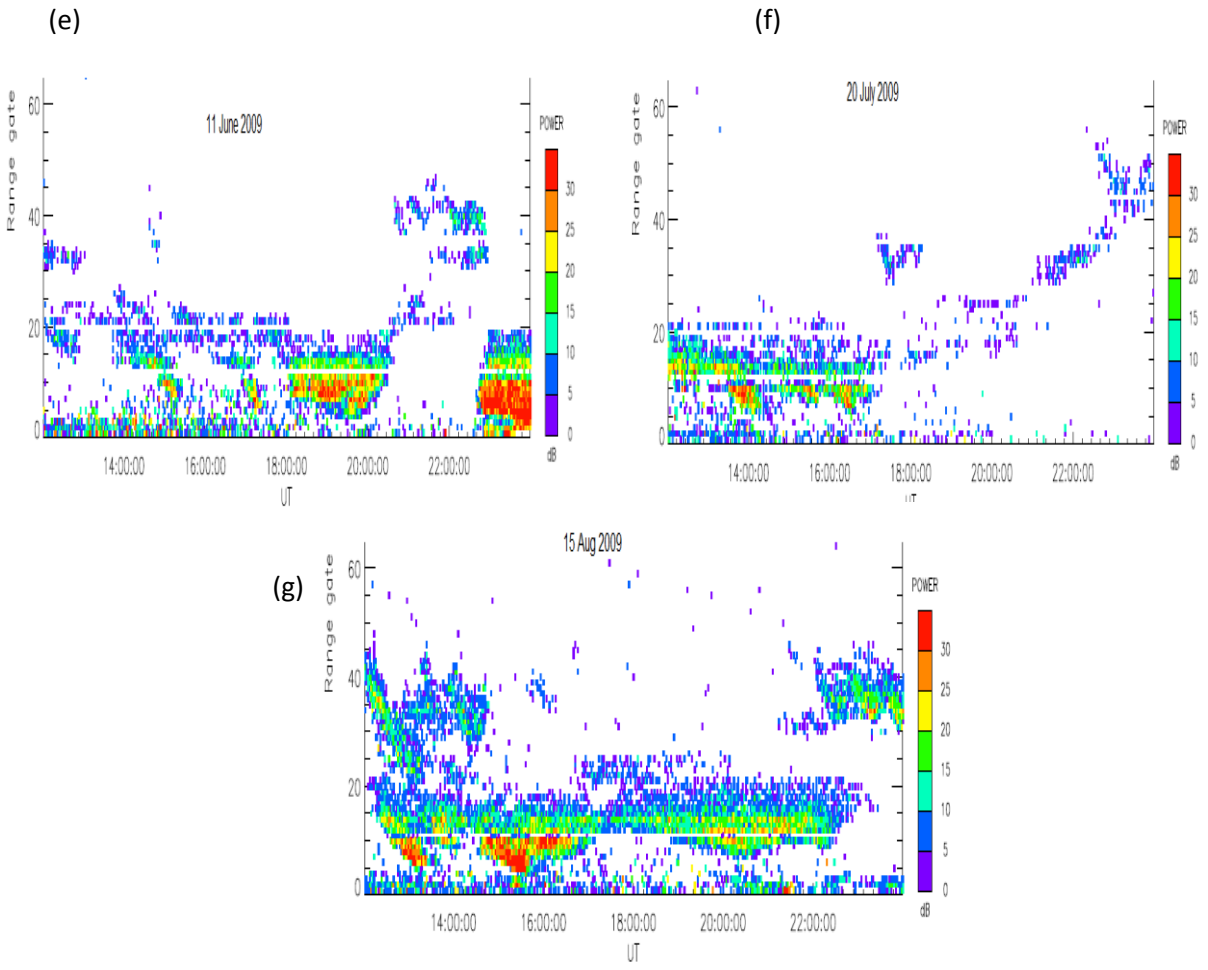

Figure 4.2: Radar range-time plot showing the ground backscatter power as a function of time and range gate (e) June (f) July (g) August. The plots show data from Beam 8 and radar was running at an average frequency of 11 MHz.

From Figure 4.3, which shows radar plots from September through November, we can see that the band of high power occurrence is from gates 20 to 40 and is consistent throughout the day in the months of September to November (i.e. from 12 UT to 24 UT in September and October and from 13 UT to 23 UT in November indicating late sunrise hours in winter). Evening time enhancements in backscatter are noted in the months of September and October. Also note the preponderance of gravity wave power enhancements in November.

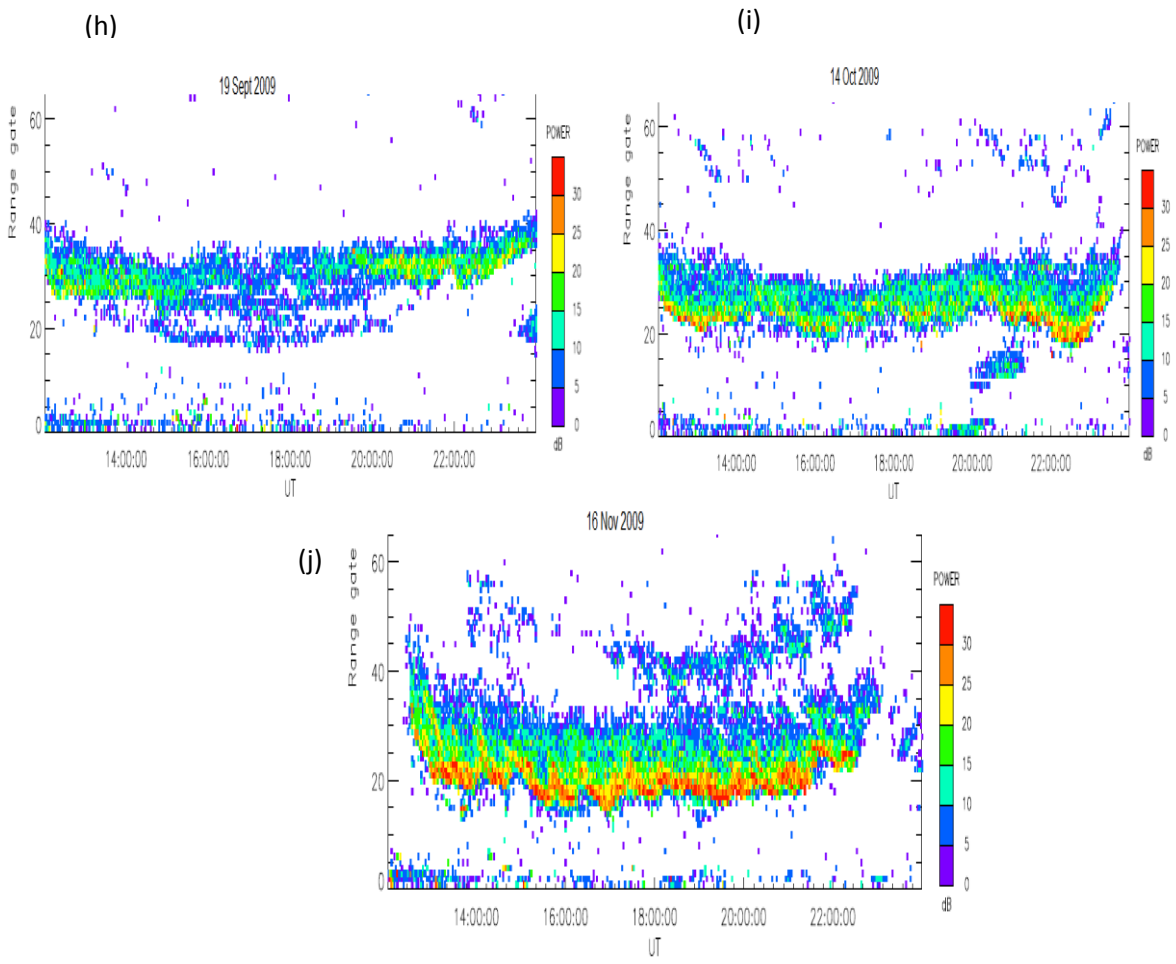

Figure 4.3: Radar range-time plot showing the ground backscatter power as a function of time and range gate (h) Sept (i) Oct (j) Nov. The plots show data from Beam 8 and radar was running at an average frequency of 11 MHz.

Based on the Figures 4.1 to 4.3 presented above, it can be concluded that the primary features observed in the backscatter power pattern for the year 2009 were:

- There is a seasonal trend in ground scatter pattern. The winter months i.e. from November to March were similar. A strong band of backscatter power from the F region was observed and this was much stronger than the power observed during the rest of the year.

- Spring months of April and May had separate contributions from both the E and F regions whereas in summer months from June to August, the backscatter was predominantly from the E region, when it was present during the day time. From April through June, the E layer became stronger and afterwards, it became weaker. The ground scatter from the E region observed in the months of June to August were in range gates below 10 as opposed to E region scatter power measured at gates 15 to 25 in April and May. This indicates a sporadic E layer formation [25] from June to August.
- In the autumn months of September and October, ground scatter is mainly from the F region and some evidence of an evening time enhancement in backscatter power.
- An evening enhancement of ground scatter power is observed in months of March through May and in October. This enhancement is normally accompanied by a sudden reduction in range to the ground scatter band. We do not know whether this enhancement occurs in summer months of June through August as the sporadic E region is blocking our view of the F region.
- It can be noted that the ground scatter power is mainly concentrated in the range gates from 20 to 40, except in the months of June, July and August. The ground scatter power from the F region is mostly concentrated in range gates 25 to 40 when there is an E region and from 20 to 40 from August through October, when there is no strong E region.

The enhancement in F region ground scatter power during the winter and the strengthening of the F region scatter power in early evening from March through May and again in October seems quite contradictory to what might be expected. During evening time, we expect ground scatter to become weaker and move out to farther ranges before it totally disappears. To our knowledge

this evening enhancement is the first observation of such an effect from the ground observations. These particular features are explored more in Section 4.2.

4.2 Anomalous Behavior in the Blackstone Ground Scatter Power

In this section, the winter anomaly and the possible reasons for the evening ground scatter enhancement in the F region backscatter power observed during summer are explained.

4.2.1 Winter Anomaly

The electron density enhancement in the F region during winter time at the mid-latitude is known as the winter anomaly. At any particular mid-latitude location and local time, the main peak electron density is greater in winter than in summer, despite the reduced solar insolation [26]. Studies by Torr and Torr (1973) concluded that the strong F2 layer winter anomaly exists at high northern mid-latitudes, primarily in the European/North America region. The winter anomaly falls off in area and amplitude with decreasing solar activity.

The reason for the winter anomaly is attributed to the higher atomic-to-molecular neutral number density ratios in winter than in summer. This is because of the seasonal variations in N_2 vibrational temperatures and an increase in the production rate of O+. The vibrationally excited N_2 causes more ion loss in summer than in winter.

A plot of electron density vs. altitude at the Blackstone radar location is given in Figure 4.4. The plot includes data from the IRI-2007 model. Days 21 Dec and 21 June of 2006 are selected to represent winter and summer respectively. The plot shows electron density profiles at 12:00 LT.

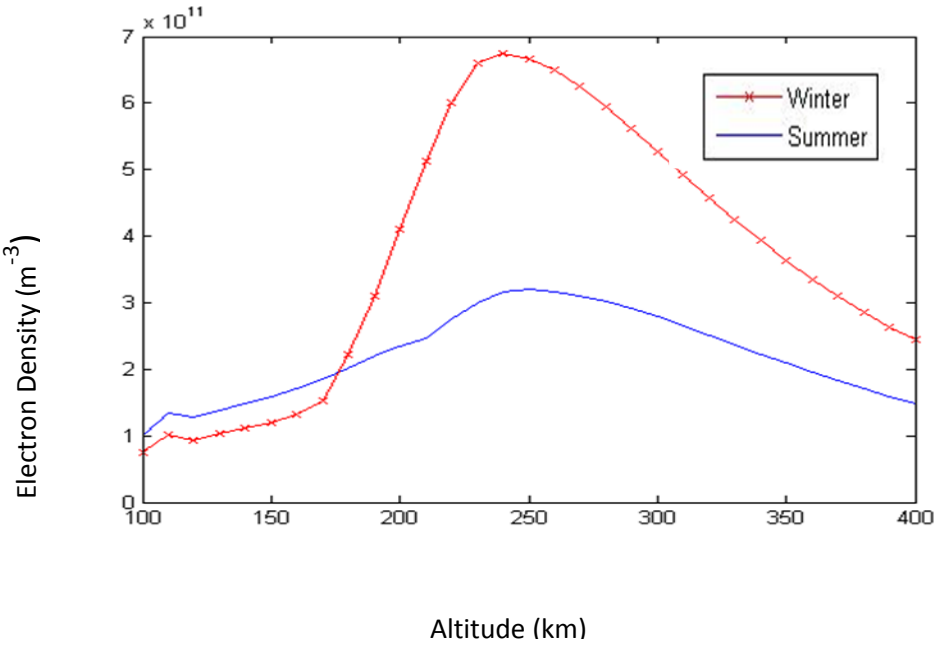

Figure 4.4: Electron density profile at Blackstone radar location; 21 Dec 2006 and 21 June 2006 represent winter and summer day respectively. Plot uses IRI 2007 model values at 12:00 LT in both days.

From Figure 4.4, it can be seen that the electron density at altitude higher than 200 km is much higher in winter than in summer. This stronger F region along with the absence of an E region leads to higher refraction from the F region in summer than in winter (November to March) as seen in radar plot Figure 4.3c and Figures 4.1a & b.

The other anomalous feature noted in Figure 4.1, namely the strengthening of the F layer ground scatter in the evening from March through June and in October is discussed next.

4.2.2 Mid Latitude Summer Night Time Anomaly (MSNA)

From March through June, an enhancement in ground scatter was seen in the evening hours. When checked for further hours beyond 24 UT, it was observed that this ground scatter persisted through later hours. The plot of the night time ground scatter for the months of March through

June are shown in Figure 4.5. The plots are from 00 UT to 6 UT, i.e. from 19 to 1 LT at Blackstone.

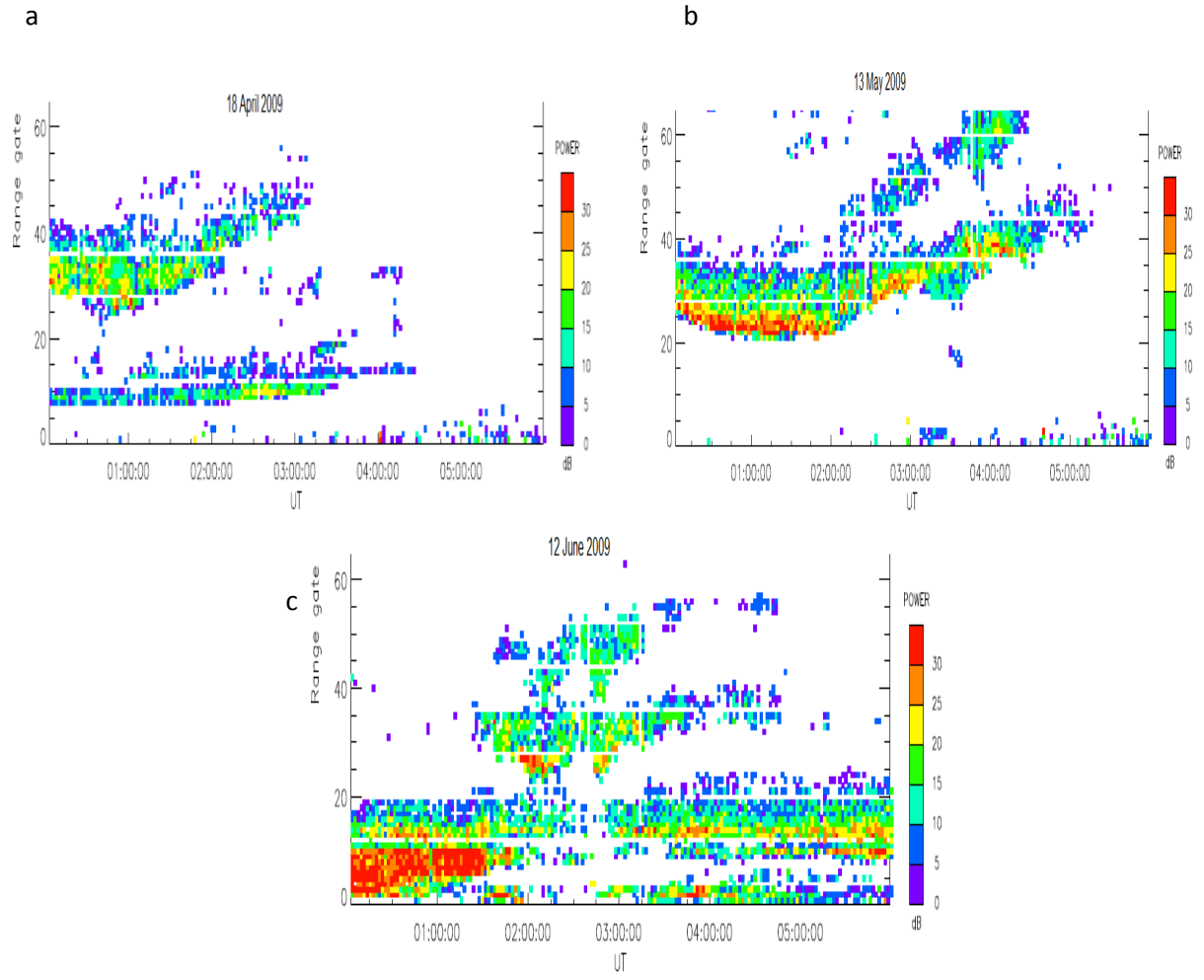

Figure 4.5: Night time radar ground scatter plots from 00 to 06 UT (a) Mar (b)Apr (c)May (d)June

In all cases, the preceding several hours had seen a reduction in day time ground scatter and a retreat to farther ranges as expected for late afternoon, followed by a sudden increase in ground scatter power and an equatorward displacement in the ground scatter band that continued till late evening as shown in Figure 4.5.

This feature of enhanced ground scatter is the strongest in May as can be seen in Figure 4.5b. The exact reason for this is not known. Global observations from FORMOSAT-3/COSMIC

mission, which is a constellation of six meteorology satellites, indicate a Mid-latitude Summer Night time Anomaly (MSNA) [27]. The anomaly is characterized by the greater night-time (1800 LT to ~0200 LT) ionospheric electron density than during the day time. This corresponds to night time hours of 23 UT to 07 UT at the Blackstone radar location. The MSNA was observed clearly in the Northern Hemisphere from 30° to ~ 60° N and spans from -60° E longitude to the east direction to ~180° E and further from 180° to -120° longitude by FORMOSAT 3/ COSMIC. Further inspection of the longitudinal variation in the MSNA presented [27] indicates that in the Blackstone sector, the anomaly peaks in the early evening, consistent with our observations.

It is probable that the evening ground scatter enhancement in Figure 4.5 is associated with this MSNA; however more radar observations and studies are needed, to confirm whether this same phenomenon is what we are observing at Blackstone and other mid latitude SuperDARN radars. Measurements with instruments capable of observing electron density, e.g., incoherent scatter radar will be helpful.

Thus from the above discussion, it can be concluded that a seasonal variation was observed in the ground scatter at Blackstone. There is also evidence of the winter anomaly and an evening anomaly in ground scatter. The following section describes our effort in reproducing the main features of the pattern of ground scatter including diurnal and seasonal variations. The method for deriving ground scatter plots from ray tracing code and comparing it with the median power plots from radar data was already explained in detail in Section 3.3.

4.3 Simulation of the Ground Scatter Power using Ray Tracing

The ray tracing code was run for each of the days shown in Figures 4.1 to 4.3 in an attempt to reproduce the features observed in the Blackstone radar ground scatter pattern. Median power at a particular hour at a range gate was derived from the radar data. Power plots showing median power as a function of time and range gate were plotted. The simulated result did not have much variation during a particular season. Hence in this discussion, typical simulation results representative of each of the four seasons is compared with the corresponding observed backscatter plot.

4.3.1 Winter Results

The comparison for winter is shown in Figure 4.6. Figure 4.6a shows the median power per hour as a function of time and range gate obtained from the radar data from November 2009 and Figure 4.6b shows the corresponding simulated plot. It can be noted that the range gate of maximum power observation is 22 in both the cases. Applying a 5 dB threshold to the simulation result, the skip zone is approximately from range gate 22 to 35 in both the cases.

The ionosphere build up is faster in the observation as shown by the sudden spike in power in range gate 22 at 13 UT and it stays elevated until 22 UT after which the power reduces rapidly (Figure 4.6a). In the case of the simulation, the maximum power range gate is 25 at 13 UT and it slowly moves towards inner gates as the time progresses and reaches gate 22 at 15 UT and stays there until 21 UT, indicating a slower build up of the IRI–2007 model ionosphere than observed in the radar data. After 21 UT, the ionosphere and hence backscatter power seems to vanish slowly.

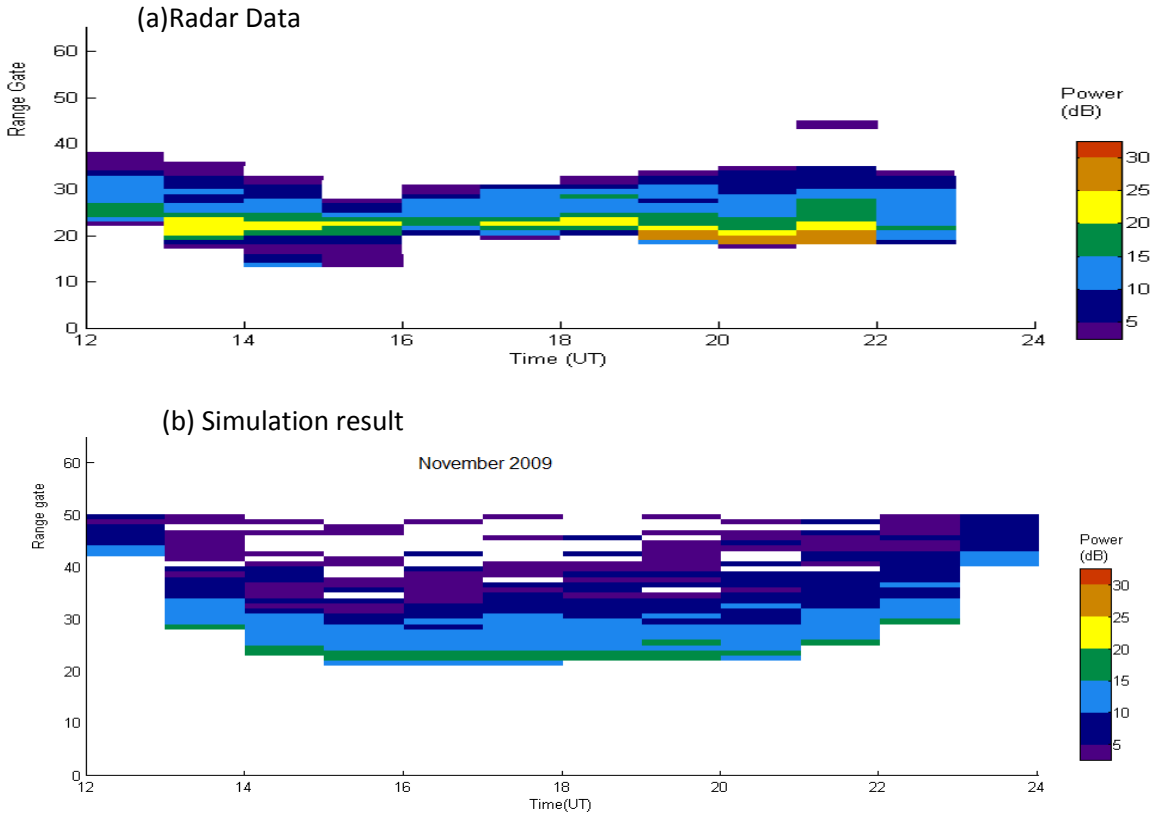

Figure 4.6: Month of November is selected to represent winter (Nov to Mar) backscatter (a) radar data obtained after taking median of power per hour for all range gates from plot Fig. 4.3.c (b) simulation result - simulations were run for 24 hours from 0 to 24 UT and color coded power values are plotted as a function of time and range gate

Overall a good agreement exists between the simulation and the observation in terms of ranges of occurrence and power variations.

4.3.2 Spring Results

Moving onto spring, the comparison plot for April is presented in Figure 4.7.

In the data in Figure 4.7a, we start seeing power at 12 UT at range gate 30 and it stays there until 15 UT after which the range gate of maximum power moves to inner gates and stays at gate 18 from 16 UT to 20 UT. This shows the buildup of the E region. A second interval of ground

scatter at further ranges corresponds to the F region scatter. When the E region is present, it refracts most of the rays and hence fewer rays reach the F region and the F region ground scatter is weakened. After 21 UT, the E region must have vanished and the scattered power is from the F region. Power remains in the band of gates 18 to 40 throughout the day.

In the simulation result, shown in Figure 4.7b, there are also distinct contributions from the E and the F region. The ground scatter band seems to remain in gates 18 to 40 throughout the day which is in very good agreement with the radar observation. The maximum power range gate is 18 from 14 UT to 20 UT which is due to the E region scatter power. Beyond 20 UT, the maximum power concentration is at range gate ~38 which matches with maximum power gate corresponding to the F region scatter seen in the radar plot.

(a) Radar Data

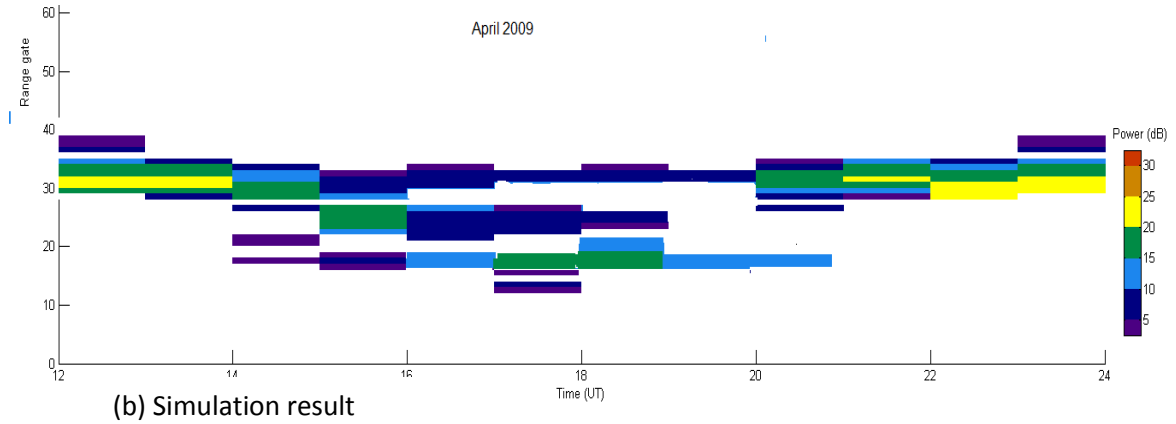

(b) Simulation result

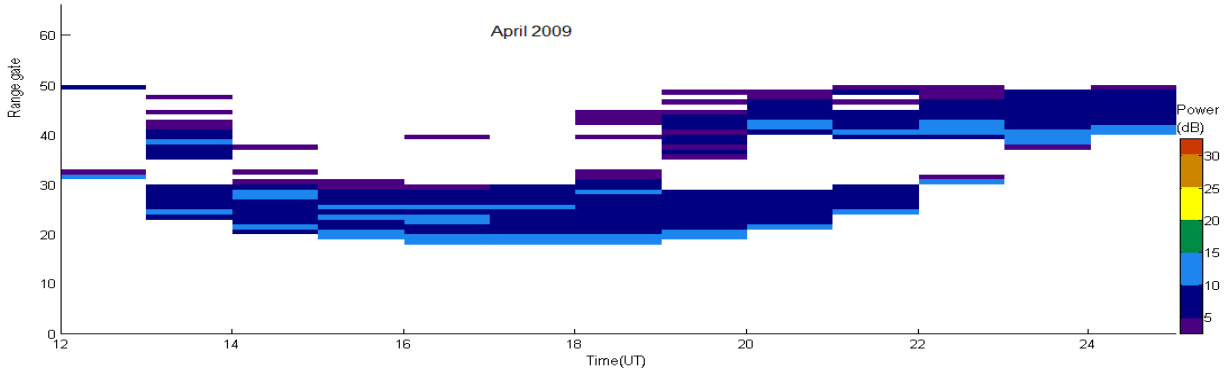

Figure 4.7: Month of April (April - May) is selected to represent spring backscatter. (a) Radar data obtained after taking median of power per hour for all range gates from plot Figure 4.1d (b) simulation result - simulations were run for 24 hours from 0 to 24 UT and color coded power values are plotted as a function of time and range gate

A plot from the ray tracing code to aid in this interpretation is shown in Figure 4.8, which shows the ground range vs. altitude for three different hours in a single day in April. As we progress though the day, we can see the formation of the E region which leads to distinct contributions in ground scatter from the E and the F region, and, at early morning and late evening hours, when the E region is not present, scatter power from the F region only.

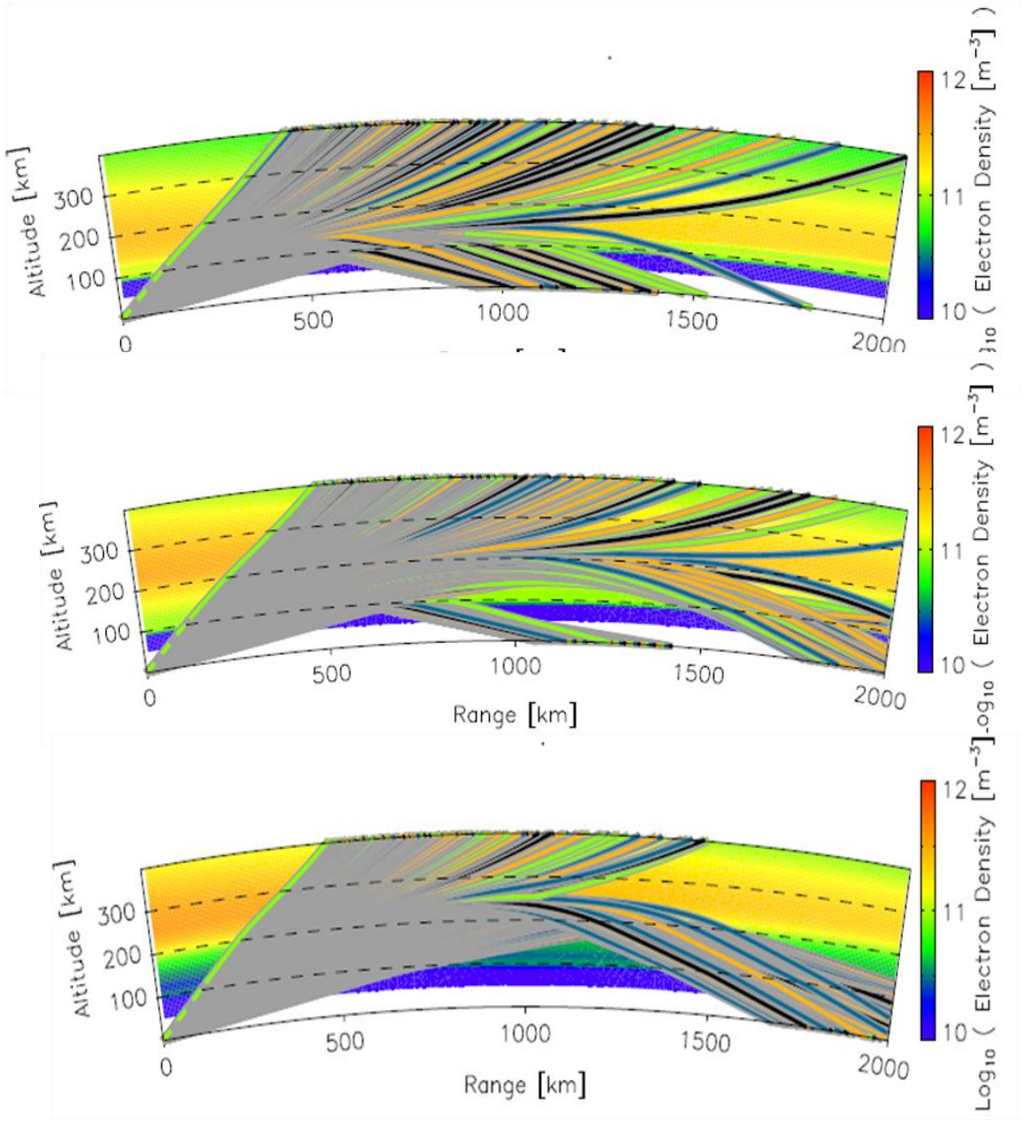

Figure 4.8: Ray Tracing plot for April 2009 (a) at 16 UT, when the E region is the strongest (b) at 20 UT when the E region becomes weaker and a strong F region exists (c) at 23 UT when the E region has totally vanished only the F region exists.

Figure 4.8 shows ray tracing at 16 UT, 20 UT and 23 UT. In Figure 4.8a, we can see that at 16 UT the ionosphere is very strong at an altitude between 100 and 200 km, which corresponds to the E region. At 20 UT, shown in Figure 4.5b, the altitude of highest electron density moves to the band of 200 to 300 km. A large number of rays, especially the lower elevation angles, are refracted from the E region. Higher elevation rays manage to penetrate through the E region and some are refracted from the F region. Thus we can see two distinct bands of ground scatter

power: one from the E region, which is at nearer ranges to the transmitter and another from the F region, which is at farther ranges from the transmitter. At 23 UT, the E region vanishes and the ground scatter observed is from the F region alone.

The F region backscatter in April is very strong from 22 to 24 UT (Figure 4.7) when compared to the rest of the day. There is no vanishing of the F region at 23 UT as in the winter result. Simulations were run for further hours to check if there are indications of the MSNA in the IRI model. But when simulated for the rest of the night, there was a very sudden vanishing of power, i.e. no evening ground scatter enhancement. Hence the IRI-2007 model could not predict this effect as observed from March through May.

Thus the IRI seemed to reasonably predict the distinct contributions from the E and the F region in spring, but failed to reproduce the evening enhancements in backscatter.

4.3.3 Summer Results

The ground scatter pattern for summer months of June to August was the most complicated as it had a sporadic E layer formation. The simulation could not reproduce the observation. The simulated ground scatter plot is shown in Figure 4.9.

From the Figure 4.2, we can see that the ground scatter data in June, July and August is not as clustered as in the other months. The software used for analyzing the radar data checks validity of data points by the number of data points in its neighborhood. Thus in these months, the software could not identify valid data points as the points were scattered around and hence there was not sufficient radar data to plot the median value of measured power per hour. However, the plot shown in Figure 4.2b is repeated for comparison.

(a)

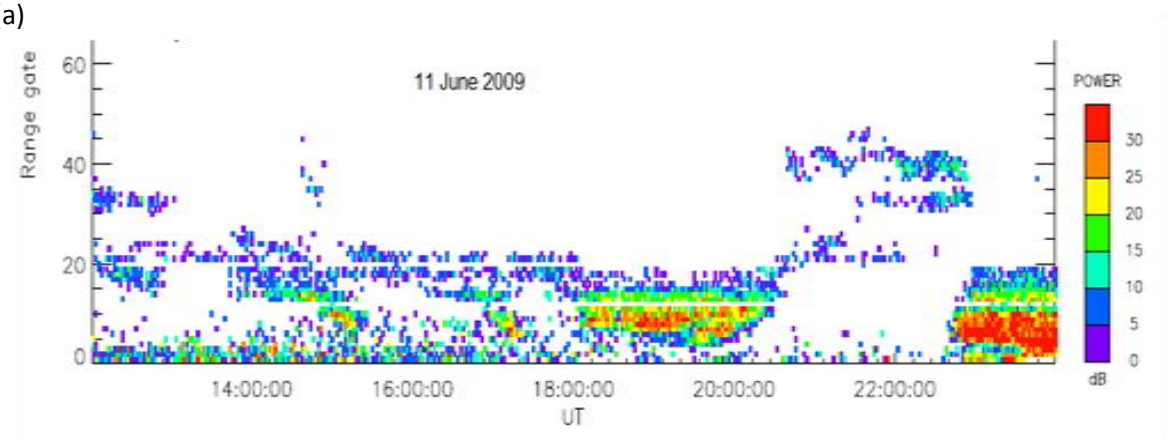

(b)

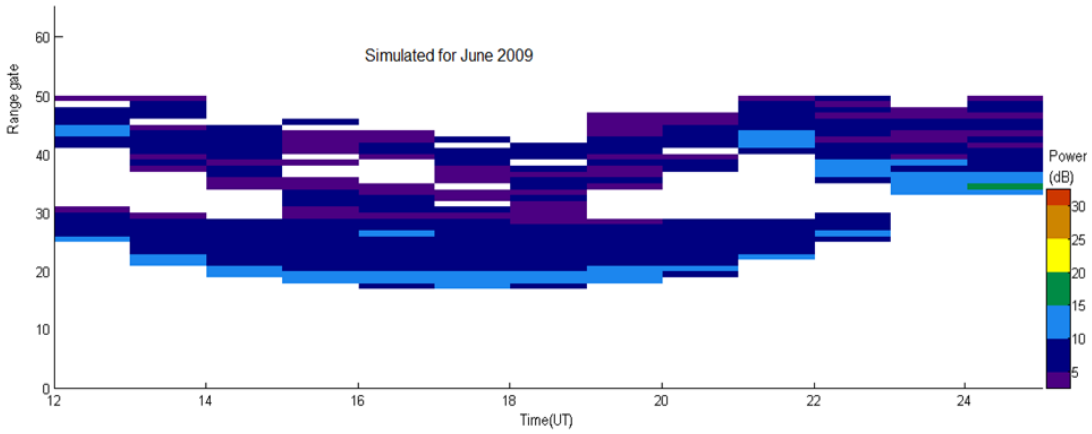

Figure 4.9: Simulation result for June to represent summer (June - Aug) ; skip band is from range gate 20 to 40 which is not at all representative of the summer radar data shown in Figure 4.2 where power is measured below range gate 20

From Figure 4.2, it can be seen that the power in the months of June through August were concentrated in range gates below 20 where as in the simulation plot shown in Figure 4.9, the power concentration is in the skip band 20 to 40. Thus the IRI model could not predict the sporadic E layer formation and hence further detailed comparison is not attempted.

4.3.4 Autumn Results

In Figure 4.10a, it can be seen that the radar data is strong at range gate ~ 35 from 12 to 14 UT and later from 20 to 22 UT. This power is from the F region backscatter. From 14 to 20 UT, the ground scatter is not very strong. This may be due to a weak E region formation. The E region is not strong enough to have a blanketing effect like in spring or summer where any of the rays penetrating the E region were not refracted to the ground by the F region.

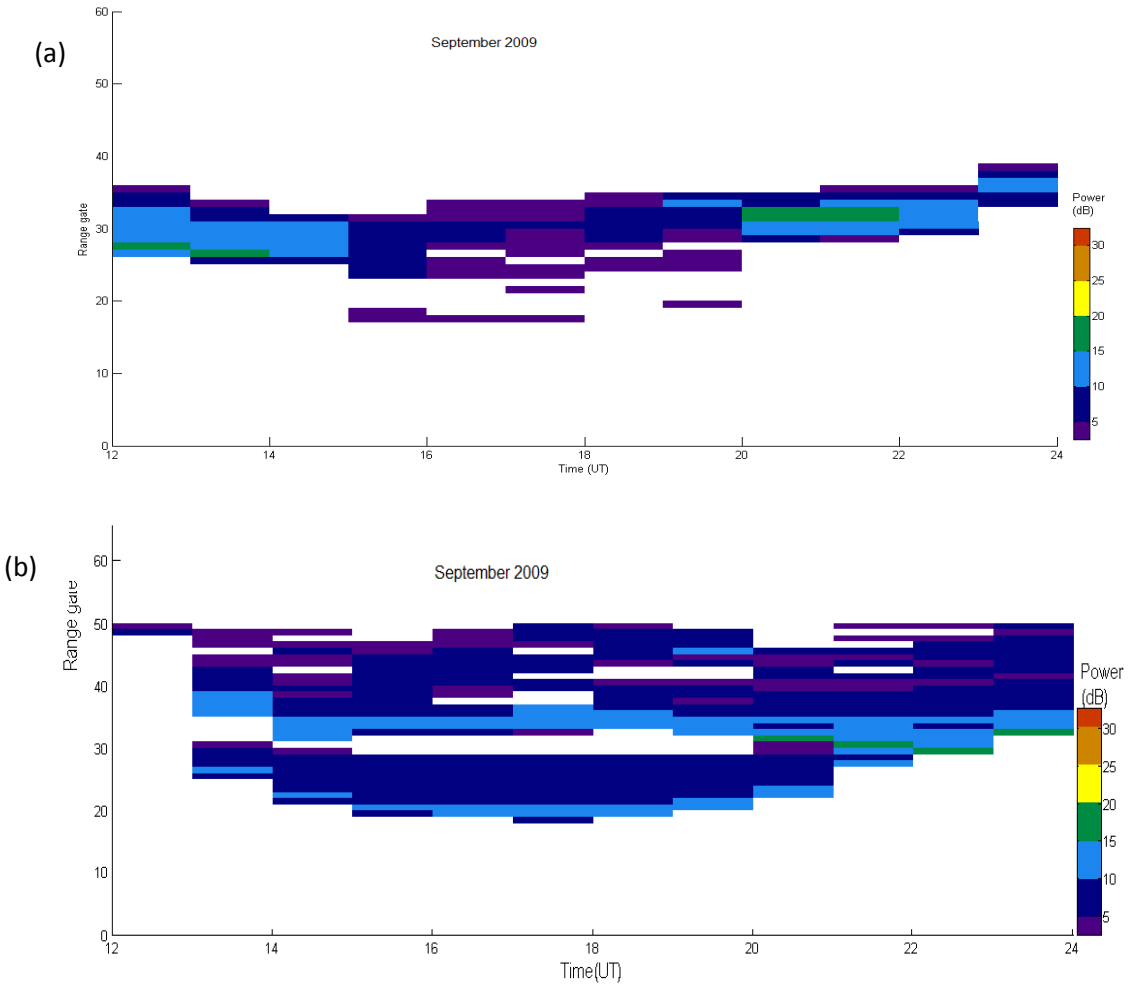

Figure 4.10: Month of September is selected to represent autumn (September - October) backscatter. (a) Radar data obtained after taking median of power per hour for all range gates from plot Figure 4.3a (b) Simulation result - simulations were run for 24 hours from 0 to 24 UT and color coded power values are plotted as a function of time and range gate

The simulation also shows 2 distinct patches of the backscatter power, one from the E and one from the F region. Thus there is reasonable agreement between the simulation and observation in autumn, except for the intensity of the E region ground scatter. This can be compared to the incoherent scatter radar measurements shown in Figure 3.2, where IRI tends to underestimate the bottom side electron density.

Also, we can see that in autumn, the power observed is in lower range gates as compared to the simulation results. This could be because of the charged particle precipitation in autumn due to increased geomagnetic activity [25].

To summarize, the main points noted while comparing radar data of ground scatter with the simulation results are:

- The simulated ground scatter power is concentrated mainly in the range gate band of 20 to 40 throughout the year. This is in very good agreement with the radar data except in the months of June through August, where the IRI model is not capable of predicting sporadic E layer formation.
- The predictions were most accurate for observation during the months of winter from November to March. The IRI could predict the absence of the E region and the winter anomaly pertaining to the F region. During winter, there was a very good agreement in the band of range gates observed. Also the backscatter was the strongest in simulation for winter when compared to other seasons which is in good agreement with the winter anomaly observed at Blackstone.
- In spring (April and May) and autumn simulation results, there is distinct backscatter from both the E region and the F region, which is in agreement with the radar data.

- The most complicated backscatter pattern was observed in the months of summer from June to August, where the predominant feature seems to be a sporadic E layer formation. The IRI model could not predict this sporadic E layer formation.
- The IRI model could not predict the evening ground scatter enhancements seen from March through May and in October. The observation of this evening enhancement is a new and surprising result.

Chapter 5

Conclusions and Future Work

The central aim of this thesis was to perform a simulation study of the pattern of ground scatter observed with the Blackstone SuperDARN radar. The ground scatter is an important tool in remote sensing the ionosphere. We aimed to reproduce the ground scatter, identify the anomalies and explore their causes. Since Blackstone radar is mid-latitude radar, the ionosphere is not as dynamic in this region as at the auroral zones. Thus simulation using ray tracing code with the IRI model was expected to reproduce the seasonal pattern observed in the ground scatter at Blackstone. Fine tuning of the ionospheric parameters should lead to better matching between simulation and observation and thus a better understanding of the ionosphere.

In Chapter 4, we saw the seasonal and diurnal variations in the ground backscatter observed at Blackstone in the year 2009 and also the simulation results using ray tracing code with the IRI-2007 model. The analysis of the observed backscatter power pattern helps in understanding the seasonal variations in different layers of the ionosphere and the performance of the radar. Also, this is the first time the IRI model is being used to simulate the ionosphere at the Blackstone radar location. Hence this exercise can also be viewed as a tool to evaluate the efficiency of the IRI model in predicting ionospheric conditions at Blackstone.

From the comparisons made between observed and simulated ground scatter power, we can say that overall, the IRI-2007 model is reasonably adequate for predicting the diurnal and seasonal variations of the average ground scatter power, but fails to predict the sporadic E region observed

during the summer or the anomalous evening ground scatter enhancement. Through systematic observation of the ground scatter power happening over a period of time, we can predict the location of the Es layer. An Es layer can be introduced into the IRI layer as a blob of electron density [28].

The antenna pattern was not considered for the simulation presented here. The antenna does not transmit equally at all elevation angles. The antenna pattern can be incorporated into the simulation code for better accuracy of prediction.

As of now, there is no information about the elevation angles in the radar measurements. This is because the interferometer array at Blackstone is not tested and validated completely for elevation angle information. The correlation between the signals at main array and interferometer array is what gives information regarding angle of arrival. The ray tracing code provides the elevation angle of the rays reaching the ground. So we can get an estimate of the elevation angles reaching the ground at a particular range gate from the ray tracing simulations.

If the elevation angle of the rays reaching the ground in a particular range gate can be obtained from the radar data, it can be used for further testing of the simulation. That is, the simulation can be queried to determine whether the same rays are producing the ground scatter at a particular range gate as in the radar observations.

While analyzing the Blackstone ground scatter pattern for 2009, a surprising effect, which is the evening time enhancement of ground scatter, was observed for the first time. This is an indication of an evening time electron density enhancement in the F region accompanying sunset, which the IRI-2007 model could not predict. The exact physics behind this phenomenon is not known. An analogous effect widely distributed at middle latitudes has only recently been reported on the basis of multiple satellite observations by Lin et al., 2010[27]. This phenomenon

can be further studied by tuning the parameters in the ionospheric model to get matching between simulation results and observations. This exercise will provide more insight into the physical conditions prevailing in the ionosphere that give rise to a dramatic evening enhancement in the F region electron density.

Appendix A

Table -1

Radio frequency bands:

Band	***Frequency range***	***Wavelength range***
Extremely Low Frequency (ELF)	< 3 kHz	>100 km
Very Low Frequency (VLF)	3-30 kHz	10-100 km
Low Frequency (LF)	30-300 kHz	1-10
Medium Frequency (MF)	300 kHz -3 MHz	100 m – 1 km
High Frequency (HF)	3-30 MHz	10-100 m
Very High Frequency (VHF)	30-300 MHz	1-10 m
Ultra High Frequency (UHF)	300-3 GHz	10 cm – 1 m
Super High Frequency (SHF)	3-30 GHz	1-10 cm
Extremely High Frequency (EHF)	30-300 GHz	1 mm – 1 cm

Table 2

List of SuperDARN radars:

Northern hemisphere SuperDARN radars:

Radar	**Latitude**	**Longitude**
Goose Bay	53.32	-60.46
Kapuskasing	49.39	-82.32
Saskatoon	52.16	-106.53
Prince George	53.98	-122.59
Kodiak	57.62	-152.19
Stokkseyri	63.86	-22.02
Pykkvibaer	63.77	-20.54
Hankasalmi	62.32	26.61
King Salmon	58.68	-156.65
Wallops	37.93	-75.47
Rankin Inlet	62.82	-93.11
Inuvik	68.42	-133.5
Blackstone	37.1	-77.95
Hokkaido	43.33	143.61

Southern Hemisphere SuperDARN radars:

Halley	-75.52	-26.63
SANAE	-71.68	-2.85
Syowa South	-69.0	39.58
Syowa East	-69.0	39.58
Tiger	-43.4	147.2
Kerguelen	-49.22	70.14
Unwin	-46.51	168.38

Appendix B

The Ray Tracing Code

The core of the ray tracing program is the Jones Stephenson's FORTRAN code which computes the ray path through the model ionosphere defined by the user. The ray tracing code from Leicester University also has IDL wrappers for plotting the ray path. A brief note on the structure of the ray tracing code is given below.

The ray tracing program consists of 3 main parts – an IDL wrapper for calling the Jones Stephenson's code (hence referred to as Jones code in this Appendix), the Jones code (in FORTRAN) and IDL wrappers for plotting.

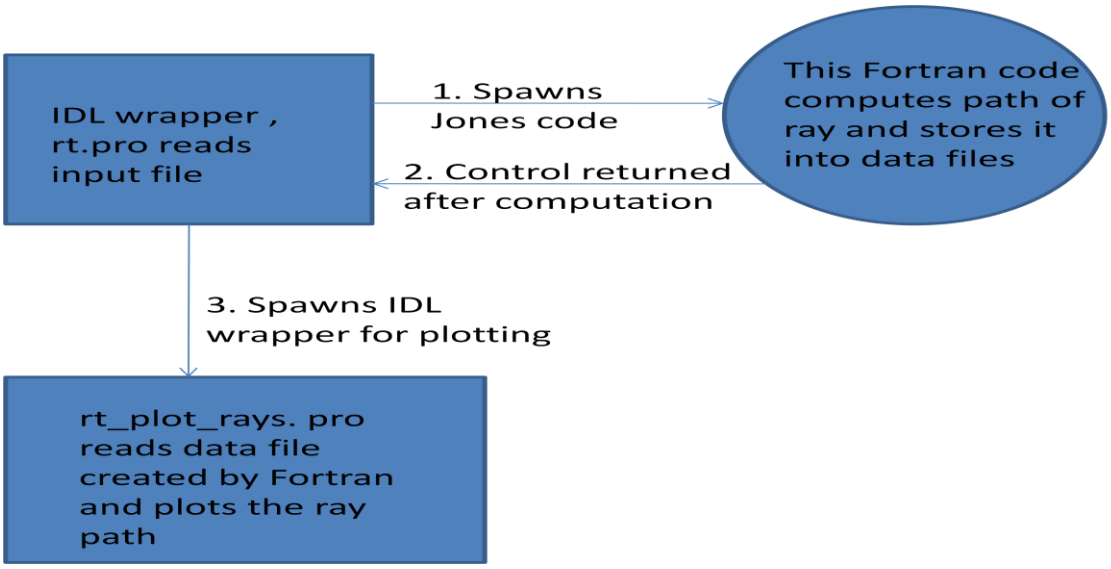

Figure B.1: Flowchart for Ray Tracing code

The ray tracing program has a FORTRAN part and 5 IDL procedures.

1. **rt.pro**: This IDL wrapper reads the input file, which has user defined parameters for simulation of the model ionosphere, and spawns the Jones and Stephenson's code. The

first 20 parameters in the input file are shown below. These values can be edited by the user. The values in the input file are read into an array in the ray tracing code. The numbers from 1 to 20 in the input file indicate the array indices.

```
*** Basic input file layout with explanations ***
 4              Method of calculating refractive index
 4              Electron density model ;  4 is double chapman
 10             Electron density perturbation model ; 10 is blob
 2              Magnetic field model ; 2 is dipolar
 4              Collision frequency model
No:   Value              Parameter Description
 1    1.     0000  Transmission mode (1=ordinary, -1=extraordinary)
 3    0.001  0000  Tx height above ground (km)
 4    37.1   1000  Tx latitude (deg)  (cutlass iceland, geomagn)
 5   -77.95  1000  Tx longitude (deg)
 7    11.000 0000  First frequency (MHz)
 8    11.000 0000  Last frequency (MHz)
 9    00.000 0000  Frequency step (MHz)
 11   335.000 1000  First azimuth (east of north) (deg)
 12   335.000 1000  Last azimuth (deg)
 13    1.000 1000  Azimuth step (deg)
 15    15.000 1000  First elevation (up of horizontal) (deg)
 16    35.000 1000  Last elevation (deg)
 17    5.000 1000  Elevation step (deg)
 20    0.000 0000  Receiver height above ground (km)
```

2. **jonesBlobTim.f**: This is the Jones code for ray tracing. The computed parameters are written into data files. The data files we use are ranges.dat which is the elevation angle of rays hitting the ground, their corresponding group range and ground path, edens.dat which is the electron density values at every point in ray integration and rays.dat which has the locus of the rays.
3. **rt_plot_rays.pro**: After execution of the Jones code, control is returned to rt.pro which spawns the IDL wrapper, rt_plot_rays.pro for plotting the ray path. This IDL wrapper in turn calls three IDL procedures – rt_read_rays.pro and rt_read_header.pro to read the values of locus of one ray and the corresponding header details respectively and rt_read_edens.pro to get the electron density values from the data files written by the Jones code.

Executing the ray tracing code

The machine needs a FORTRAN compiler and IDL environment to execute this ray tracing code.

To execute the ray tracing code, go to the directory where the FORTRAN code and the 5 IDL wrapper procedures (mentioned above) are available. Start IDL or DAVIT (DAVIT is a data analysis package of SuperDARN group at Virginia Tech) and type the following commands in the IDL prompt.

IDL >.comp rt (to compile the module)

IDL > rt,/do_rt,inp=’20060925.inp’ (This will start execution of the code ; 20060925.inp is the name of the input file)

Once the code is executed, we can see that the data files and a raytrace.pdf are generated in the current directory. The file raytrace.pdf has the plot of ray path as a function of ground range and altitude, and the electron density profile at the transmitter location.

The value of group range of rays that hit the ground can be read from ranges.dat along with corresponding ground range and their initial elevation angles.

Appendix C

Doxygen for ray tracing code documentation

Doxygen is a documentation system for C, C++, Python, IDL etc. Doxygen can generate an online documentation browser (in HTML) from a set of documented source files. It can also be used to extract the code structure from undocumented source files.

jonesBlobTim.f was first converted to C using the f2c convertor which is an open source tool for converting source code in Fortran to C language. This conversion was needed as the FORTRAN code available was not compatible with doxygen.

A part of the HTML file generated using doxygen is shown in the Figure C.1 below. Figure C.1 represents a caller graph which shows what all subroutines call the subroutine 'readw'.

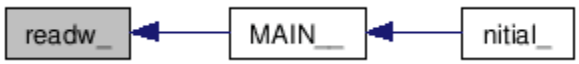

Figure C.1: Caller graph of subroutine 'readw'

In the figure, each of the blocks represents a function (or subroutine). Such a graphical representation of function call helps in understanding the flow of the program. The call graph for subroutine (function) 'readw' is shown in Figure C.2. From Figure C.2, we can see what all subroutines are called by the subroutine 'readw'. On clicking each of these subroutines, we can get into the details of that particular subroutine. For example, the call graph seen when clicking on 'rindex' in Figure C.2 is shown in Figure C.3.

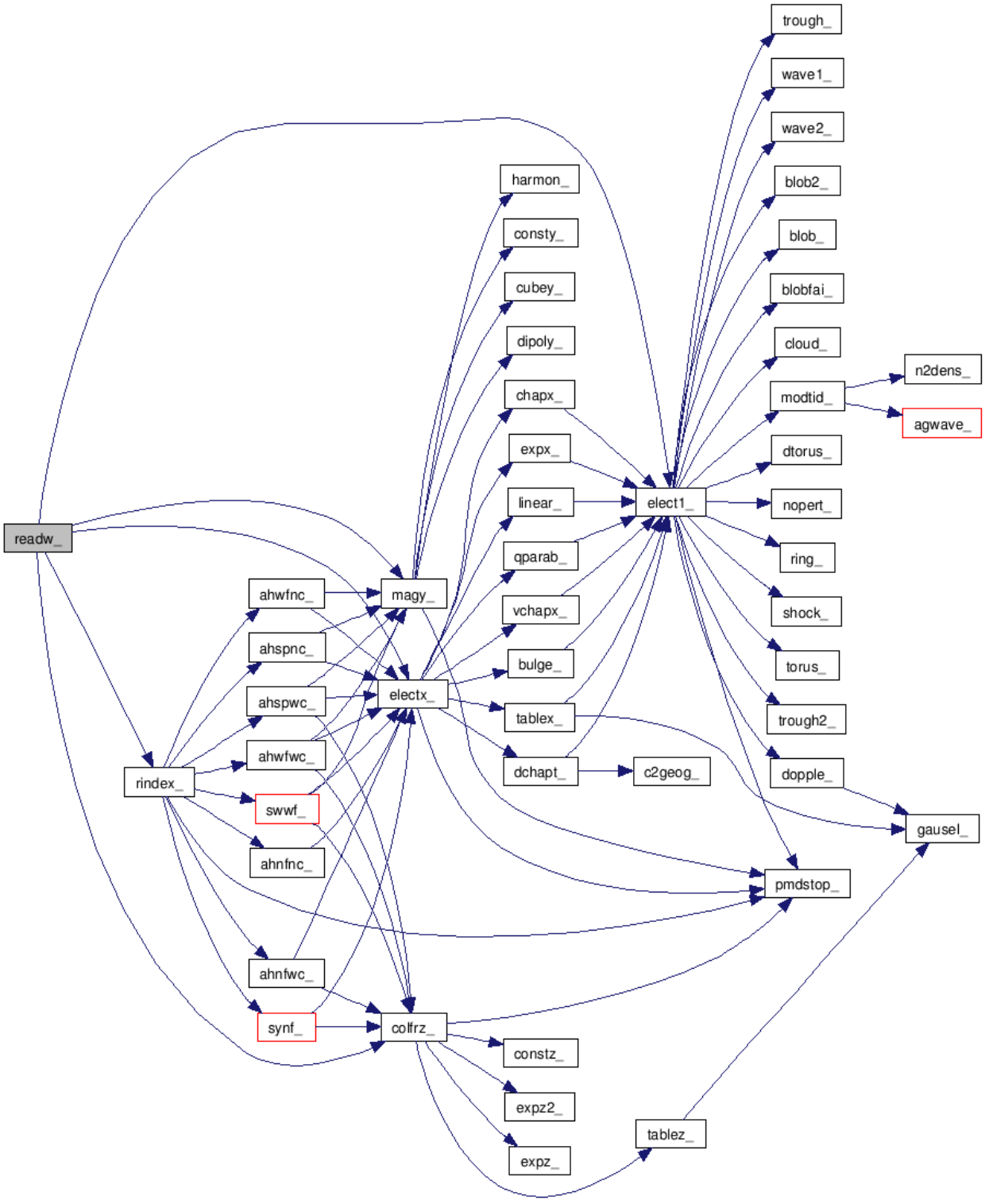

Figure C.2: Call graph for function ‘readw’

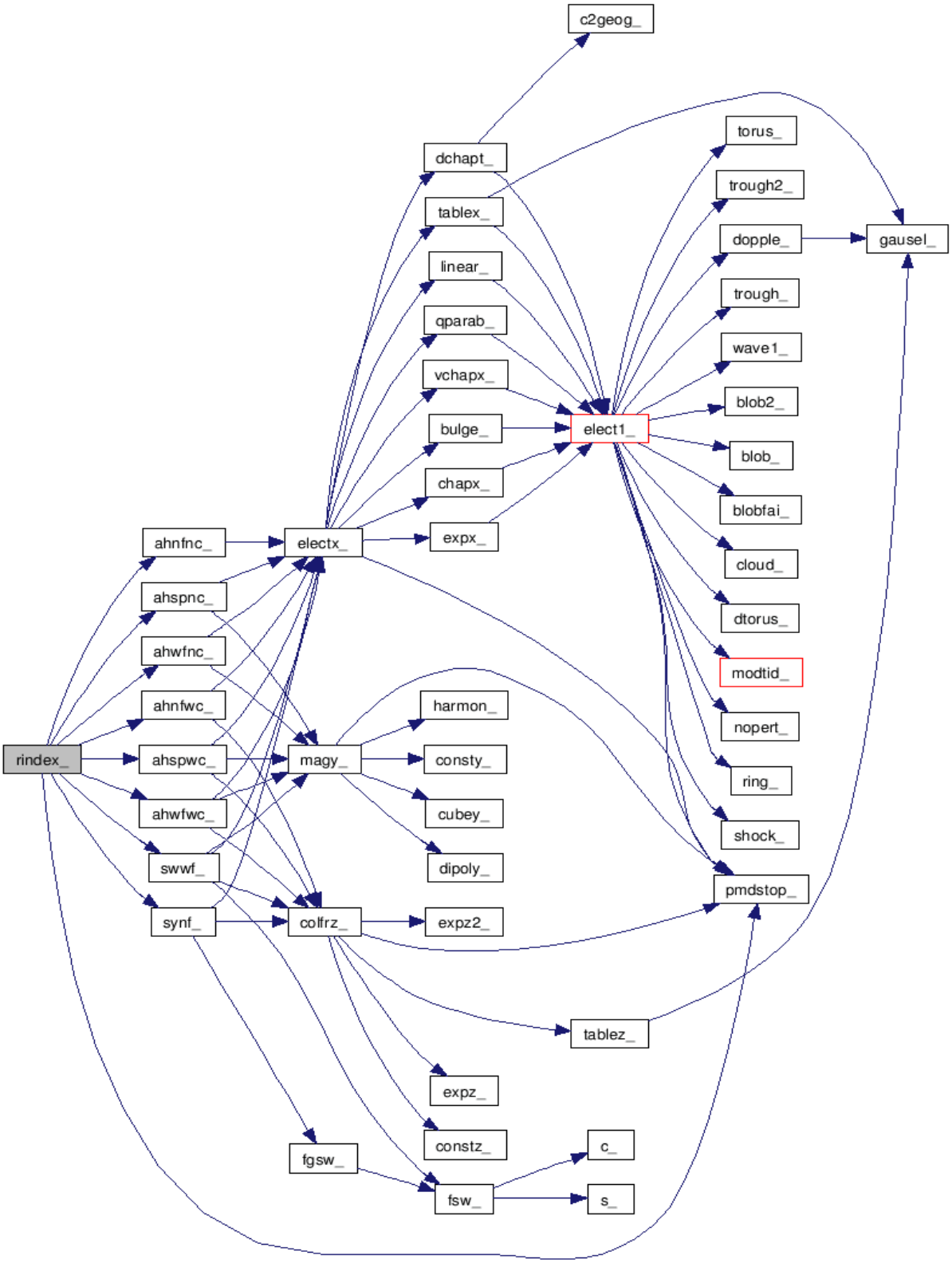

Figure C.3: Call graph for function ‘rindex’

Appendix D

RTI plots from the ray tracing code

Electron density was modeled using the empirical model IRI-2007 throughout this thesis. The FORTRAN source code for the latest version of IRI can be downloaded from NSSDC's FTP site ftp://nssdcftp.gsfc.nasa.gov/models/

An occasional check should be done to make sure that the IRI code available in our machine is the latest version for later uses. A readme.txt is available in the ftp site which explains the functionalities of each of the FORTRAN subroutines. It also explains how to use the IRI model as a standalone program to lookup the electron density values.

The IRI code was downloaded into the SuperDARN machine and integrated into the raytracing code. The user can give '9' as electron density parameter in the input file (Refer to Appendix B) to use the IRI-2007 model (which is the latest version of IRI available till date). The changes made to the code to incorporate IRI are documented in the code (jonesBlobTim.f) itself. The user can search for keyword 'IRI-2007' to identify these changes at a glance.

The code can be run from the folder where the ray tracing procedures and IRI folders are available. Start DAVIT or IDL and enter the following commands (as mentioned before in Appendix B):

```
IDL >.comp rt

IDL > rt,/do_rt,inp='20060925.inp',rdate='2006,0621,23'
```

This will start execution of the code; ‘rdate’ is the date and hour for which the simulation is run; format is ‘year,month_date,hour’(note that the underscore is used here only for clarity). Time shown here is LT (Local time). To use Universal Time, add 25 to the hour for which simulation is to be done. For example for running the simulation for 06-21-2006 at 14UT, rdate=’2006,0621,39’ and for simulation for 14 LT of the same day, rdate=’ ’2006,0621,14’

Running the raytracing code for more than one hour

Power plots were to be generated for a minimum of 12 hours for a single day. Hence a script was written to run the code in loops. The shell script used for this is shown below.

```
#!/bin/bash

linked_files=`find . -maxdepth 1 -type f`

script_time=`date +%F-%H%M%S`


function start_sim() {
        hour=$1
        mkdir ray_${script_time}_${hour}
        cd ray_${script_time}_${hour}
        for f in $linked_files; do
                ln -s ../$f
        done


        echo "rt,/do_rt,inp='20060925.inp',rdate='2009,0920,$hour'" > davit_in
        davit < davit_in
        cd ..
}
```

```
start_hour=0

stop_hour=2


for((hr=$start_hour;hr <= $stop_hour;hr++)); do
        echo start $hr
        start_sim $((hr+25))
done


wait
```

In this script, the user can specify the date and the start and stop hours (shown highlighted in the script). Time in UT can be entered and the script adds 25 to the hour before calling the IRI subroutines. For example the script above will simulate for 09-20-2009 for hours 0 to 2 UT. The script is named 'run_davit_par.sh' and can be executed by typing './run_davit_par.sh' from the directory where the script is located. The script will generate one folder corresponding to each hour and the file will be named with date and hour during which the user run the simulation and the hour for which simulation was run. For example a folder titled 'ray_2010-05-27-115924_25' indicates that the simulation was done on 05-27-2010 at 11:59:24 and was done for hour 25 UT. Inside this folder, all the data files generated by the ray tracing program for that particular hour of the day can be seen.

Once we have the data files after simulation, the file ranges.dat can be read to generate the power plot by reading values of group path of rays hitting the ground. The matlab script used to read this group range; plot ray density and power histogram and the color coded plot of power as a function of range gate and time is shown below.

```
% clear all

% close all

% clc



% figure - plot ray denstity vs group path



grp_path = []  % The group path values of rays when they strike the ground

               % is to be entered in this matrix

range_gate=[180:45:2385]; % starting values of range gate

range_gate_no=(range_gate-180)./45+1;



n=histc(grp_path,range_gate);



% To plot ray density histogram, uncomment this block of code

    % bar(range_gate_no,n)

    % xlabel('Range gate');
```

```
    % ylabel('Number of rays');
    % axis([5 50 0 100]);
    % title ('Ray Density vs. Group Path')


% figure % plot power vs grp path
power=10.*log10(n); % to get power from ray density
power(~isfinite (power)) = 0 ;


% To plot power histogram, uncomment this block of code
    % bar(range_gate_no,power)
    % xlabel('Range gate');
    % ylabel('POwer(dB)');
    % axis([0 50 0 50]);
    % title ('Power vs. Group Path')


%Color coded plot or power
t=23;  % Time for which the simulation is run
```

```
% figure

hold on

colmat = [  75 0 130;       %indigor

            0 0 128;        %navy

            28 134 238;     %dodgerblue

            0 139 69;       %spring green 3

            255 255 0;      %yellow

            205 133 0;      %orange 3

            205 55 0;];



%convert to matlab rgb

colmat = colmat/255;



power_q=floor(power/5);

x_vertex=[];

y_vertex=[];
```

```
for i=min(range_gate_no):max(range_gate_no)
        x_vertex= [t; t+1; t+1; t];
        y_vertex= [i; i; i+1; i+1];
    if(power(i)~=0) % To remove plotting zero values in power
          h= fill(x_vertex,y_vertex,colmat(power_q(i) + 1,:));
        else
           h=fill(x_vertex,y_vertex,'w');
        end
        set(h,'edgecolor','none');
end
colormap(colmat);
caxis([0 35]);
colorbar
axis([12 24 0 100]);
xlabel('Time(UT)');
ylabel('Range gate');
```

Plotting radar data

The Matlab script used for reading the ascii file which has the details of range gate, corresponding power measured, frequency and plotting the RTI (range time intensity plot) after computing median value of power measured at a particular range gate in a particular hour is given below.

```
close all;

clc



data=load('2009_1115_beam8.txt');



% Find number of hours to be simulated

t_min=min(data(:,6));

t_max=max(data(:,6));



for t=(t_min:t_max)  % Plotting for each hour

    % Extract range gate and power values from data file corresponding to

    % 't'th hour

    power=zeros(length(find(data(:,6)==t)),2) % Initialise an array
```

```
power(:,1)=data(find(data(:,6)==t),2);

power(:,2)=data(find(data(:,6)==t),19);



% Find nearest and farthest range gate

rg_min=min(power(:,1));

rg_max=max(power(:,1));

n_gates=(rg_max-rg_min)+1;



power_median=zeros(1,(rg_max-rg_min)+1); % to store median power in each gate

temp=zeros(n_gates,30); % 30 samples per range gate are taken in an hour

count=1;



% To find median power in a range gate

for i=(rg_min:rg_max)

    power_rdng=power(find(power(:,1)==i),2); % a row vector returning power rdng of a particular gate

    temp(count,:)=[power_rdng' zeros(1,30-length(power_rdng))]; % padded with zeros to account for sweeps with no rdng
```

```
%     if(~isempty(temp))
        power_median(count)=median(temp(count,:));
         count=count+1;
%     end
end


% Plotting
r_gates = [rg_min:rg_max];
% time = [0:24];
t_min=18;
t_max=19;


x_vertex=[];
y_vertex=[];
cols = [];
tmp = 1;
```

```
%quantized

power_median_q = floor(power_median/5);

k = 1;



% rgb colors

%refer http://cloford.com/resources/colours/500col.htm


colmat = [  75 0 130;       %indigo

          0 0 128;        %navy

          28 134 238;     %dodgerblue

          0 139 69;       %spring green 3

          255 255 0;      %yellow

          205 133 0;      %orange 3

          205 55 0;];
```

```
    %convert to matlab rgb
    colmat = colmat/255;


%     figure;


    hold on;


    for i=(rg_min:rg_max)
        x_vertex= [t; t+1; t+1; t];
        y_vertex= [i; i; i+1; i+1];


        if(power_median(k)~=0) % To remove plotting zero values in power_median
            h=fill(x_vertex,y_vertex,colmat(power_median_q(k) + 1,:));
        else
             h=fill(x_vertex,y_vertex,'w');
        end
        set(h,'edgecolor','none');
```

```
        k = k + 1;
    end
end
colormap(colmat);
% set('edgecolor','white');
caxis([0 35]);
% set('edgecolor','white');
colorbar


axis([12 24 0 100]);
title('2009-11-15;  BKS Beam 8')
xlabel('Time (UT)')
ylabel('Range Gate')
```

List of References

1. Brian F. Windley, *The Early History of the Earth*, London, John Wiley and Sons, 1976
2. Davies Kenneth , *Ionospheric Radio Propagation,* New York, Dover Publications,1966
3. R.D. Hunsucker, J.K. Hargreaves, *The high-latitude ionosphere and its effects on radio propagation,* New York, Cambridge University Press, 2003
4. Michael C. Kelly, *The Earth's Ionosphere Plasma Physics and Electrodynamics,* San Diego, Academic Press Inc. ,1992
5. IPS Radio and Space Services educational notes http://www.ips.gov.au
6. Donald William Danskin, *HF auroral backscatter from E and F regions*, PhD thesis, University of Saskatchewan, 2003
7. Rawer K, *The ionosphere; its significance for geophysics and radio communications,* translated from German by Ludwig Katz, New York, F. Ungar Pub. Co., 1957
8. R.D. Hunsucker, *Radio techniques for probing the terrestrial ionosphere,* Berlin; New York, Springer-Verlag, 1991.
9. Nathaniel Frissel and Lyndell Hockersmith, S*eeing beyond: Over the Horizon Radar Systems and HF propagation,* White paper, 2008
10. K. Rawer, *Wave propagation in the ionosphere*, Dordrecht; Boston, Kluwer Academic, 1993.
11. Nathan Blaunstein, Eugeniu Plohotniuc, *Ionosphere and applied aspects of radio communication and radar*, Boca Raton, CRC Press, 2008.
12. J. A. Ratcliffe*, An introduction to the ionosphere and magnetosphere,* Cambridge [Eng.] University Press, 1972.
13. SuperDARN website hosted by John Hopkins University http://superdarn.jhuapl.edu/

14. Henry Rishbeth and Owen K. Garriott, *Introduction to ionospheric physics*, New York, Academic Press, 1969.
15. MPM Hall, LW Barclay, *Radio wave propagation*, London, Peregrinus, 1989.
16. Nicholas M. Maslin, *HF Communications: A systems Approach*, New York, Plenum Press, 1987
17. K.G. Budden, *The propagation of radio waves: the theory of radio waves of low power in the ionosphere and magnetosphere*, Cambridge [Cambridgeshire]; New York, Cambridge University Press, 1985.
18. John A Richards , *Radio wave propagation : An introduction for the non-specialist*, Berlin Springer,2008
19. N. Carrara et.al , "Guided Propagation of HF radio waves in the ionosphere", *Space Science Reviews 11* , pg.555-592, 1970
20. R. Michael Jones and Judith J. Stephenson, *A versatile three-dimensional ray tracing computer program for radio waves in the ionosphere*, OT Report 75-76. PB2488567, Colorado, National Geophysical Data Center, 1975
21. D. Monselesan et. al., "First step towards tiger frequency management: A ray tracing exploration using both IRI and IGRF models", *Advances in Space Research*, Volume 27, Issue 1, pp. 167-174,2001
22. D. Bilitza, "International Reference Ionosphere 2000", *Radio Science*, Volume 36, no. 2, pp. 261-275, 2001
23. Shun-Rong Zhang et.al. , "Multiple-site comparisons between models of incoherent scatter radar and IRI", *Advances in Space Research*, Volume 39, Issue 5, pp.910 -917,2007

24. Kevin Sterne, *Testing the Re-designed SuperDARN HF radar and modeling of a Twin Terminated Folded Dipole Array,* Master's thesis, Virginia Tech, 2010

25. R.J. Normal et.al., *Comparing HF radar backscatter from the southern ocean with ray-tracing results using the IRI model,* Published by IPS http://www.ips.gov.au/IPSHosted/NCRS/wars/website/proceedings/final/g/norman_f.pdf

26. A.V. Pavlov et.al, "Causes of the mid-latitude NmF2 winter anomaly at solar maximum", Journal *of Atmospheric and Solar Terrestrial Physics*, Volume 67, Issue 10, pp. 862-877, 2005

27. C.H. Lin et.al., "Mid-latitude summer nighttime anomaly of the ionospheric electron density observed by FORMOSAT -3 /COSMIC", *Journal of Geophysical Research*, Vol. 115, A03308, pp.11 , 2010

28. P. A. Bradley, "Ingesting a sporadic E model to the IRI" , *Advances in Space Research*, Volume 31, Issue 3, pp. 577-588, 2003